Passivity–Based Control and Stability Analysis for Hydro–Solar Power Systems

Universidad Tecnológica de Pereira

Walter Julián Gil–González

Passivity–Based Control and Stability Analysis for Hydro–Solar Power Systems

Walter Julián Gil–González

This dissertation is submitted for the degree of
Ph.D in Engineering

Pereira, December 2, 2019
UNIVERSIDAD TECNOLÓGICA DE PEREIRA
Doctorate in Engineering

Passivity–Based Control and Stability Analysis for Hydro–Solar Power Systems

Main advisor: **Alejandro Garcés–Ruíz**, Ph.D.
Universidad Tecnológica de Pereira
Co-advisor: **Andrés Escobar–Mejía**, Ph.D.
Universidad Tecnológica de Pereira
Co-advisor: **Olav B. Fosso**, Ph.D.
Norwegian University of Science and Technology

Committee

Ph.D. Alexander Molina Cabrera, Universidad Tecnológica de Pereira. Pereira, Colombia.
Ph.D. Maximiliano Bueno López, Universidad del Cauca sede Popayán, Colombia.
Ph.D. César Augusto Orozco Henao, Universidad del Norte. Barranquilla, Colombia.

Pereira, December 2, 2019
Doctorado en Ingeniería con énfasis en Ingeniería Eléctrica
Universidad Tecnológica de Pereira
Cl. 27 # 10-02, Pereira, Risaralda
TEL: (+57)(6)3137122
www.utp.edu.co

Abstract

Modern power systems are under transformation due to the inclusion of non–conventional renewable energy sources such as wind and photovoltaic generation. Even though these energy sources are good alternatives for the sustainable harnessing of energy, they affect operation and stability of the power system, due to their inherently stochastic nature and dependence on weather conditions. In addition, solar and wind farms have a reduced inertia capability that must be compensated by large synchronous generators in conventional hydro–thermal systems, or by energy storage devices. In this context, dynamical interaction between conventional and renewable sources must be studied in detail. By 2030 that the Government of Colombia projects that Colombian power system will integrate in its energy matrix at least 1.2 GW of solar photovoltaic generation. For this reason, it is necessary to design robust controllers that improve the stability in power systems with high penetration of photovoltaic and hydro–power generation. This dissertation studies new alternatives to improve the dynamic response power system during and after large disturbances using passivity–based control. This is because power system components are inherently passive and permit Hamiltonian formulations, thus exploiting the passivity properties of mechanical and electrical systems. The main contributions of this dissertation are: a decentralized passivity–based control of the hydro–turbine governing systems for multimachine power systems to stabilize the rotor speed and regulate the terminal voltage of each hydro–turbine governing systems in the system as well as a PI–passivity–based control for the photovoltaic solar plants and superconducting magnetic energy storage which is robust according to parametric uncertainties and unmodeled dynamics. Simulation results validate the proposed controllers.

List of abbreviations

This is a short list of the main abbreviations used in this dissertation.

ac	:	Alternating current.
AVR	:	Automatic voltage regulator.
dc	:	Direct current.
DPC	:	Direct power model.
IDA–PBC	:	Interconnection and damping assignment passivity–based control.
ITAE	:	Integral of the time–weighted absolute error.
HTGS	:	High–voltage direct current.
HTGS	:	Hydro–turbine governing systems.
PLL	:	Phase–locked loop.
PI–PBC	:	Proportional–integral passivity–based control.
pH	:	port–Hamiltonian.
POD	:	Power oscillation damper.
PSS	:	Power system stabilizer.
PV	:	Photovoltaic solar.
SHP	:	Small hydro–power.
SMES	:	Superconducting magnetic energy storage.
VSC	:	Voltage source converter.

Contents

Chapter 1

Introduction

This chapter presents the motivation of this dissertation focused on improving the dynamic response of the power system with high–level penetration photovoltaic solar plants during and after large disturbances. The related work as well as contributions, aims, publication derived from this dissertation are also presented.

1.1 Motivation

Modern electric power systems are a fundamental part of social and economic progress of a country, since the levels of production, agro–industrial development and the quality of life of citizens depend on the continuous supply of electricity (Barbero, 2013); For this reason, it is important to have a reliable, continuous and high–power quality energy supply. Additionally, the economic growth of any country is closely related to the development of its power infrastructure (Barbero, 2013). Therefore, transient stability analysis is an important topic in design and operation of electric power systems to maintain their secure operation during and after large disturbances (e.g., fault, loss of a generator, loss of lines or loads, sudden changes in the tie–line flow) (Machowski et al., 2008; Chaiyatham and Ngamroo, 2017). In addition, the integration of renewable energy sources and the growing demand have increased the complexity and uncertainty of the systems and pushed to operate close to their capacity limits, thus increasing the stress on the power system which can lead into a blackout as a consequence of a large disturbance (Anderson and Fouad, 2003). For this reason, there is an increasing interest in investigating methods for maintaining and improving the stability of electric power grids.

Modern systems may also include new technology such as high–voltage direct current (HVDC) and energy storage devices. The HVDC systems present many advantages such as improving power quality, fast control on the active and reactive power independently, connection to remote generation or feeding of load isolated and facilitating power grid connections, among others (Beerten et al., 2014; Zheng et al., 2015; Liao et al., 2017). These advantages have permitted a growing role in energy transmission systems throughout the world and have shown the potential for large–scale application in power transmission and distribution systems (Haruni et al., 2013; Yang et al., 2018a).

The HVDC systems are required in the context of renewable generation integration since renewable energy sources or hydro-power plants may be far from the demand centers. In the case of energy storage systems, they have begun to play an important role in improving the dynamic response of the power system (Zakeri and Syri, 2015; Kiaei and Lotfifard, 2017). In addition, they are technologies that allow a massive integration of renewable energy sources since they can compensate power oscillations which are generated by uncertainties of primary resources (Zakeri and Syri, 2015). The most common energy storage systems are supercapacitors, flywheels, batteries and superconducting coils (Ibrahim et al., 2008; Zakeri and Syri, 2015). Superconducting magnetic energy storage systems (SMES) have great attention from electric utilities due to their advantages in comparison to flywheels and batteries, such as fast response, high efficiency (around 95%) and,particularly the large amounts of power discharges during small periods of time (Zakeri and Syri, 2015) and unlimited number of charging and discharging cycles (Ibrahim et al., 2008; Zakeri and Syri, 2015). Fig. 1.1 illustrates an example of a modern electric power system which consists of conventional power plants based on synchronous generators (e.g., thermal and hydro power plants), non–conventional generation units (e.g., wind and solar power plants), distribution grids (or microgrids), and demands (e.g., residential, industrial and commercial).

The Government of Colombia predicts that by 2023, the Colombian power system will have important changes in its energy mix, with the integration of at least 3.0 GW of photovoltaic solar (PV) and wind plants, according to the Colombian government's Mining and Energy Planning Unit (CREG, 2017). Since it is expected that Colombia power system reach high-level PV penetration, in this dissertation, will focus on the study of PV systems.

This research is oriented to propose controllers to hydro–turbine governing systems (HTGSs), PV plants and superconducting magnetic energy storage SMES system that allow improving the dynamic response of the power system during and after large disturbances. In addition, to propose a methodology for computing the reference values of the PV plants and SMES system that permit enhancing power oscillation damper (POD) in a power system with a high–level of PV penetration. The proposed controllers are more elaborated control schemes with high performance in order to guarantee stability under a wide range of operating conditions of the power systems since the conventional control approach (i.e., cascade linear regulators, especially PID controls) may be insufficient in the new context of high–level of integration of renewable energy sources (Chen et al., 2013). Additionally, this dissertation wants to take advantage of the mathematical structure of the components of the power system to design nonlinear control schemes that guarantee stability in the sense of Lyapunov's theory. This mathematical structure has the property to be passive and present a Hamiltonian structure, which can be exploited by using passivity–based control (PBC). The PBC theory proposes a control law which keeps structure passive and guarantees stability conditions in closed–loop (Ortega et al., 2013; van der Schaft, 2017). In addition, the PBC is useful to demonstrate that a feedback interconnection of passive systems is passive and that certain strict passivity properties are inherited (Ortega et al., 2013). Therefore, using the properties of the interconnected passive systems is presented as a convenient form to analyze the power systems (Ortega et al., 2013; van der Schaft, 2017).

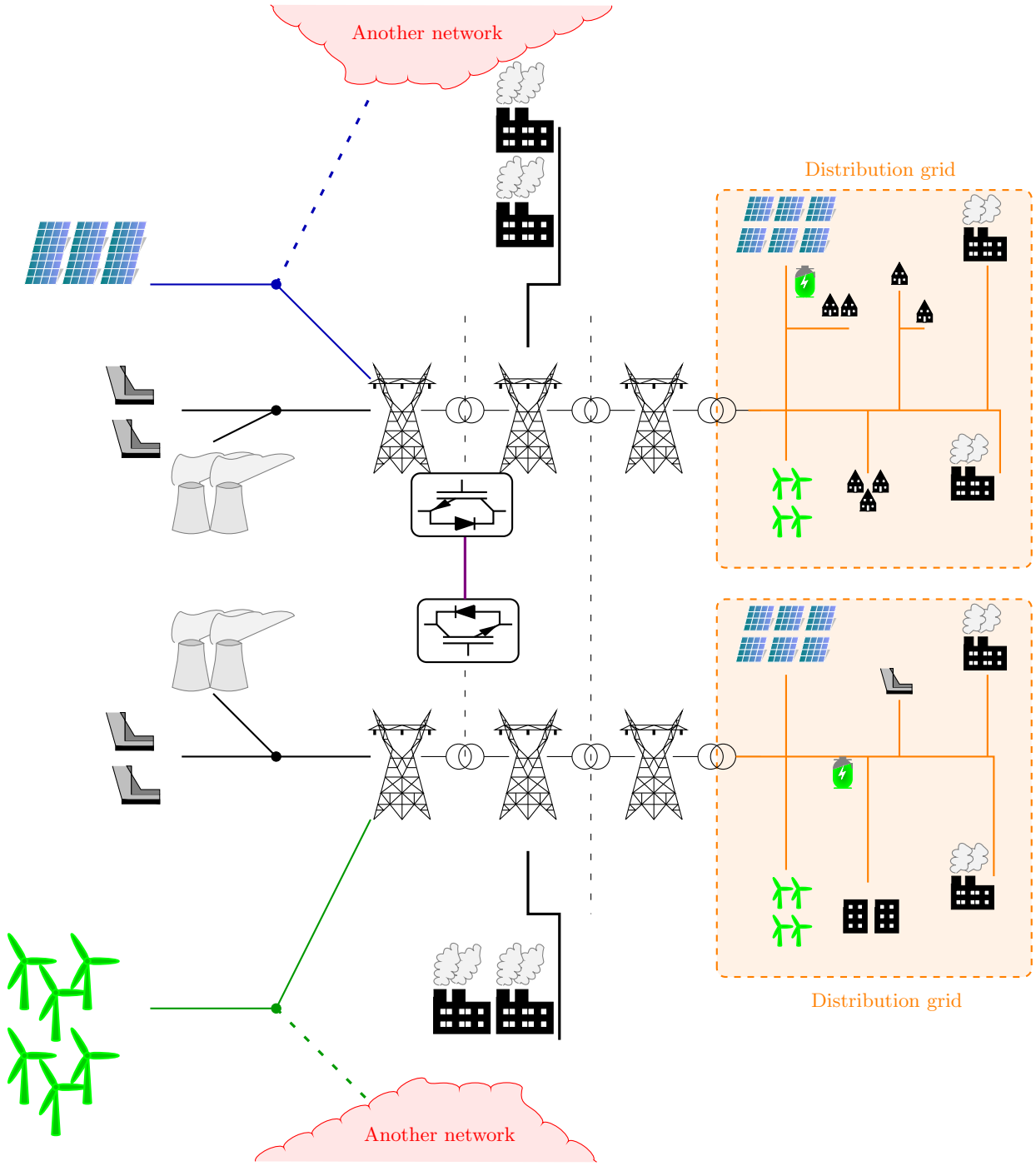

Figure 1.1: Example of a modern electric power system composed by conventional power plants based on synchronous generators (gray–colored), non-conventional generation units (green–blue–colored), distribution grids (orange–colored), and demands (black–colored).

1.2 Problem Statement

Power generation using renewable energy sources has been widely applied to ensure more reliable, sustainable and environmentally friendly power systems (Energy, 2016). In the near future, it is expected that several systems may reach penetration levels over 30% (Corbetta et al., 2015). However, as a consequence of the high variability of the primary energy resources and uncoordinated design of controllers in the power electronic devices, these generations may affect the power systems' behavior in steady state. This significantly changes power flow patterns and influences its dynamic performance (Li et al., 2013; Montoya et al., 2018). In addition, the large integration of renewable energy sources (e.g., PV and wind plants) diminishes inertia and synchronizing coupling in the power systems, which may be harmful to the transient stability of the systems (Chaiyatham and Ngamroo, 2017; Li et al., 2013; Remon et al., 2017).

On the other hand, the growth of demand, its fluctuations, and a continuous system expansion make it difficult that the power system maintains its synchronization. Hydroelectric power plants play an increasingly important role in the frequency regulation and power balancing in hydro–dominated systems (Pico et al., 2012; Guo et al., 2017). In addition, low–frequency oscillation phenomena in hydro–dominated systems have been noted in different countries (see (Pico et al., 2012) for the Colombian case), which has motivated the study of improved regulation performance for hydro–turbine governing systems (HTGSs) in order to guarantee stable operation of the power system. Nevertheless, the HTGS is a complex non–linear system with an intrinsic non–minimum phase characteristic, which has a strong coupling among mechanical, hydraulic and electrical dynamics, making it a complicated system to be analyzed (Xu and Qian, 2015). Additionally, some other factors such as the appearance and attenuation of the water hammer phenomenon and the large disturbances of the power system hamper the design of control from a non–linear perspective which simultaneously covers the entire dynamics of the hydraulic, mechanical and electrical parts (Gil-González et al., 2019; Chen et al., 2013; Zhang et al., 2018b). For this reason, the control of HTGS is usually designed from a small signal perspective while separating the dynamics of each subsystem. Since the controls of the hydro–generators are responsible for maintaining the terminal voltages and rotor speeds close to the reference value and injecting sufficient power to damp oscillations and by this contributing to the overall objective.

Today, most HTGSs are equipped with cascade controllers for the governor subsystem (IEEE working group report, 1992; Babunski and Tuneski, 2003; Jiang et al., 2006) and the automatic voltage regulator (AVR) as well as for the power system stabilizer (PSS) which is usually connected to the excitation subsystem (Lee, 2016; Huerta et al., 2018). These controllers can be complicated, having a combination of proportional, integral and derivative properties. The controls are designed and tuned for the worst–case condition and tested by perturbing the closed–loop system under several transient conditions (Huerta et al., 2018). Even though this technique has been used for many years, it does not guarantee global stability and would not be sufficient in modern power systems with the integration of renewable energy sources. Therefore, it is essential to investigate non–linear techniques with high performance that guarantee the power system stability after large disturbances.

The problems mentioned above caused by HTGS and PV plants need to be addressed in the Colombian power system since 66.8% of its total generating capacity is composed by hydro–based power plants. Furthermore, it is expected the increase in PV plants in the next years (CREG, 2017). Hence, it is necessary to analyze and propose control strategies that allow preserving the global stability of the network and enhancing its dynamic response. In this context, we can pose the following research question:

How to improve the dynamic response of hydro–dominated power systems with high–level PV penetration and maintaining the stability during and after large disturbances?

In order to answer this question it is necessary to apply a generalized control theory with the following features: *i*) Applicable to each component of power system such synchronous machines, hydro–turbines, the PV plant, and energy storage system. *ii*) Exploit the structure of the system. *iii*) Easily integrable with the model of the whole power system. *iv*) Guaranteed stability in different operating conditions as well as during and after large disturbance, and *v*) Scalable for the large power systems.

The PBC is an adequate control theory to meet all these features (Ortega et al., 2013; van der Schaft, 2017; Nageshrao et al., 2016). In addition, the PBC is useful to demonstrate that a feedback interconnection of passive systems is passive and that certain strict passivity properties are inherited (Ortega et al., 2013; van der Schaft, 2017; Nageshrao et al., 2016). Therefore, using the properties of the interconnected passive systems is considered a convenient form to analyze the power systems. Additionally, we employ a methodology for the PV plants and superconducting magnetic energy storage (SMES) system which add damping to the power system, and so help improve its dynamic response.

It is important to highlight that the problems mentioned of the HTGS and the PV plant in the approach have not been analyzed together yet. These analyses are always carried out independently as presented in section 1.3 where a detailed review of state–of–the–art is shown.

1.3 Related Work and Contributions

This section presents a summary of the literature focused on controllers for HTGS, PV plants, SMES systems, and VSC–HVDC systems applied to power system transients. In addition, related work to small–hydro power plants are shown. In each part, the state of the art is compared to the ideas proposed in this dissertation.

1.3.1 Summary of investigations related to controllers for HTGS

Recently, investigations focused on studying new control schemes for improving the dynamic response of HTGS have been conducted. Some of these investigations considered uncertain parameters or unknown dynamics such as those presented in (Guan and Pan, 2008) and (Cerman and Hušek, 2012). Other investigations were developed to reduce undesirable oscillations by employing hybrid fuzzy sliding mode controls (Liang et al., 2017) or sliding mode controls (Chen et al., 2014). In (Zhang et al., 2015), a non– linear predictive control method for a HTGS was presented which

used a performance index with a terminal penalty function that guarantees stability in the sense of Lyapunov for discrete systems. In (Zhang et al., 2016a), a complementary control strategy was proposed for a governing system to regulate the frequency in an island AC network at sending terminal of the high–voltage direct current system. The authors of (Zhang et al., 2017) established the dynamic model for a pump–turbine considering the non–linear piecewise function of relative parameters. In (Zhang et al., 2018c), the impacts of the PI gains in a pumped–storage hydroelectric power plant by introducing the random power load were studied. In (Zhang et al., 2018a), a novel approach was proposed to establish the transient modeling of the HTGS. In (Xu et al., 2016b), an adaptive fast–fuzzy fractional order PID control for the pumped–storage hydro unit employing improved gravitational search algorithm was proposed. Control schemes such as intelligent method control (Kishor and Singh, 2007), fuzzy control (Nagode and Škrjanc, 2014; Li et al., 2017a), fault tolerant control (Simani et al., 2016), synergetic control (Zhu et al., 2017; Zhou et al., 2018), and finite–time control (Ma et al., 2018) have also been proposed. Even though these techniques appear to be effective and robust in their applications, they have limitations such as the need for parameter tuning, adaptation to requirements of large–scale systems, change of control rules, online optimization processes or problems of stability. Additionally, some of these investigations did not consider the entire dynamics of HTGS (i.e., hydraulic, mechanical and electrical dynamics) and they were neither analyzed in a large–scale power system nor under large disturbances.

On the other hand, other authors developed controls based on the port–Hamiltonian (pH) representation of the subsystems guaranteeing stability of some parts for the HTGS in closed–loop (Zeng et al., 2010; Xu et al., 2012; Zeng et al., 2014; Xu et al., 2016a; Li et al., 2017b). These authors used an orthogonal decomposition method known as a generalized Hamiltonian theory to design control with a pH structure in closed–loop (Xu et al., 2016a; Li et al., 2017b). The authors of (Gil-González et al., 2019) showed that it is possible to achieve an open–loop pH structure of HTGS, generating a control law based on passivity theory that exploits its natural structure and, also guarantees its stability in closed–loop. Nevertheless, these controls have some limitations. Firstly, they used a third–order model of a synchronous machine, which only describe mechanical and excitation flux dynamics. Secondly, they did not consider multimachine systems and apply centralized schemes which could be challenging to implement in large–scale power systems where the HTGS are located in wide geographical areas; therefore, communication between them could be difficult. Table 1.1 summarizes these and other investigations related to controllers for HTGS.

In contrast to these previous works, this dissertation presents the following innovations:

- A decentralized PBC of the HTGS for multimachine power systems to stabilize the rotor speed and regulate the terminal voltage of each HTGS in the system is proposed.
- The entire dynamics of each HTGS are described by an eleventh–order model, which considers the non–linear dynamic of the mechanical and hydraulic system as well as the electrical system. The latter using the sixth–order model of the electric machine. It is important to notice that previous works only considered the mechanical part or the electrical part independently.
- The proposed controller avoids all problems of communication between the HTGSs and maintains the passive structure in closed–loop through interconnection and damping

Table 1.1: Summary of Investigations Related to Controllers for HTGS.

Test system	Control approach	References
Single–machine infinite–bus	Sliding mode control	(Guan and Pan, 2008; Chen et al., 2013)
	Passivity–based control	(Zeng et al., 2010; Gil-González et al., 2018; Gil-González et al., 2019)
	PID control	(IEEE working group report, 1992; Babunski and Tuneski, 2003) (Sanathanan, 1987; Ling and Tao, 2006a; Wang et al., 2011) (Khodabakhshian and Hooshmand, 2010; Zhang et al., 2018a,c)
	Hybrid fuzzy sliding mode controller	(Zargari et al., 2012; Cerman and Hušek, 2012; Liang et al., 2017)
	Fuzzy predictive control	(Chen et al., 2014)
	Predictive control	(Kishor and Singh, 2007; Zhang et al., 2015)
	Optimal robust control	(Jiang, 1995a; Zou et al., 2016; Zhang et al., 2017)
	Fractional–order PID control	(Xu et al., 2016c; Li et al., 2017a; Xu et al., 2016b)
	Fuzzy control	(Nagode and Škrjanc, 2014; Li et al., 2017a)
	Fault tolerant control	(Simani et al., 2016)
	Synergetic control	(Zhu et al., 2017; Zhou et al., 2018)
	Finite–time control	(Ma et al., 2018)
	Generalized Hamiltonian model	(Xu et al., 2012; Zeng et al., 2014)
	Adaptive control	(Liu et al., 2016)
	Grey prediction control	(Wang et al., 2016)
Multi–Machine system	PID control	(Zhang et al., 2016a; Leon et al., 2012a)
	Generalized Hamiltonian model	(Xu et al., 2016a; Li et al., 2017b)

assignment (IDA).

1.3.2 Summary of investigations related to controllers for PV plants

Several studies have focused on transient stability in power systems with high penetration levels of renewable: In (Rodriguez et al., 2002), it was analyzed how a large number of wind power generators influence the dynamic performance in the Spanish power system while the authors in (Delille et al., 2012) investigated the use of energy storage to mitigate the impact of inertia–less renewable energy sources on an isolated power system; In (Tamimi et al., 2013), the impact on system stability was investigated for different penetration levels in Canada; In (Wang and Du, 2016), the frequency stability problems of the European synchronous area were studied; In (Edrah et al., 2015), a wind power generator supported by a static synchronous compensator (STATCOM) was used in order to secure the reactive power support during grid faults to avoid degradation of stability.

The works mentioned above comply with network standards by employing conventional controllers. However, these controllers were not designed to interact harmoniously with the grid. Other works were focusing on controllers for renewable energy sources actively contributing to the power system stability. In (Shah et al., 2013; Surinkaew and Ngamroo, 2018; Chaiyatham and Ngamroo, 2017; Surinkaew and Ngamroo, 2019), and (Surinkaew and Ngamroo, 2017) were demonstrated how inter–area oscillation damping is feasible by using a wide–area measurement–based damping controller at a PV plant. In (Korai and Erlich, 2015), a methodology to enhance the frequency stability of a power system, with significant penetration of distributed energy resources, was studied. Other research works were based on emulating

synchronous generators by voltage source converters. Provision of synthetic inertia by applying the well–known concept of *virtual synchronous generators* was discussed in (Miller et al., 2011) and (Bevrani et al., 2014). This approach has usually been employed in systems with high penetration of renewable energy sources, in smart grids and/or microgrids (Shintai et al., 2014; Suul et al., 2016; Zhang et al., 2016b; Mo et al., 2017). However, studies of the impact this may have on the dynamic performance of the transmission system, have been scarcely undertaken. The references (Remon et al., 2017b) and (Remon et al., 2017) modeled the PV plants as a virtual synchronous generator for stability studies. Table 1.2 presents recent research of the transient stability in power system with large penetration levels of renewable. Note that none of the works proposed so far, employs Hamiltonian representations for the control design. In contrast to these previous works, the main contributions of this dissertation in relation to PV plants are:

- A methodology for improving power oscillation damper (POD) in power system with high–level PV penetration based on a washout–filter is proposed. The proposed methodology does not force the dynamic behavior of a voltage source converter (VSC) as a virtual synchronous generator. In addition, it takes into account the operating limits of the VSC, which considers first active power and then, the reactive power.
- A power direct model (DPC) for PV plants is developed, which avoids using phase–locked–loop (PLL) to integrate a VSC. Hence, it increases the reliability of the system without time delay while diminishing the investment costs in electronic devices.
- A study of three different penetration levels of PV plants is done to determine the impact of these on the power system transient.
- A PI–PBC for PV plants modeled as DPC is described, which combines the advantages of passivity-based stability control with the uncomplicated implementation of PI controls.

1.3.3 Summary of investigations related to controllers for SMES system

Different works have been focused on improving stability in the power systems. In (Sadeghi et al., 2016), a robust controller for a class of nonlinear chaotic power systems based on the non-quadratic Lyapunov function was proposed. In (Modirkhazeni et al., 2016), the oscillations of the frequency in isolated hybrid power system were enhanced, using a Takagi–Sugeno fuzzy system to determine the contribution coefficient of a wind turbine. The authors of (Khooban et al., 2016) proposed a simple indirect adaptive general type–II fuzzy sliding mode controller for power systems dealing with uncertain and external disturbances. The performance of static synchronous compensator (STATCOM) versus static var compensator (SVC) based on fuzzy controller for stability improvement of wind farm connected to multi-machine power system were compared in (Hemeida et al., 2018), and in (Leon et al., 2012b), a comparison of excitation control based on feedback linearization and interconnection and damping assignment controller was presented, with the objective of damping oscillations in power systems. In the case of the mitigation of subsynchronous oscillations in power systems several devices, such as SVC,

Table 1.2: Summary of Investigations Related to Study of the Transient Stability in Power System with Integration of Renewable Energy Sources.

Generation technology	Control approach	Research approach
Wind generators	PI	In (Rodriguez et al., 2002) was studied as the high penetration of wind power affects the power system dynamics in Spain. In (Edrah et al., 2015) was modeled a wind power as a STATCOM with the purpose of supplying the reactive power during grid faults without affecting the stability.
Photovoltaic generators	PI	In (Remon et al., 2017), (Remon et al., 2017), and (Remon et al., 2017a) are analyzed the effects and impacts have PV system in the transmission power system. These investigations model the PV systems as virtual synchronous generators.
	H_∞-based control	In (Shah et al., 2013) proposed a wide-area measurement-based damping controller for a PV system for the damping of inter–area oscillation.
	Fuzzy PID Controller	In (Chaiyatham and Ngamroo, 2017), a smart control of PV farm for improving the transient stability in the interconnected power system was proposed.
Wind and Photovoltaic generators	PI	In (Tamimi et al., 2013) was analyzed the stability in the power system in Canada for different penetration levels of DERs. In (Delille et al., 2012) researched to compensate low inertia of DERs on an isolated power system based on energy storage system. In (Korai and Erlich, 2015), a methodology for the frequency stability improvement of the power system to a high-level DERs penetration was analyzed.

STATCOM, PV–STATCOM, resistive type superconducting fault current limiter (SFCL) and SMES, among others have been proposed to be integrated to the grid. The works published in (Hammad and El-Sadek, 1984) and (Abi-Samra et al., 1985) employed an SVC connected to the synchronous generator terminal where subsynchronous resonance (SSR) is damped for all critical levels of series compensation. In (Patil et al., 1998) and (Padiyar and Prabhu, 2006), the use of a STATCOM was analyzed as an auxiliary controller based on rotor speed to alleviate SSR; In (Varma and Salehi, 2017) it was proposed a controller based on PV-STATCOM to alleviate SSR where it is considered two modes of operation for PV–STATCOM, one during daytime and other during nighttime. Also, other FACTS devices have been employed to mitigate SSR, e.g., unified power flow controller (UPFC) (Raju et al., 2017), static synchronous series compensator (SSSC) (Bongiorno et al., 2008; Thirumalaivasan et al., 2013; Rajaram et al., 2017) and thyristor controlled series compensator (Zhu et al., 1995). Table 1.3 shows the applications of the SMES system focused on improving classical problems of the power systems such as subsynchronous resonance and power system stability. Although there are multiple works of the SMES system focused on improving transient stability none of them consider the penetration of renewable energy sources. In contrast

Table 1.3: Summary of Investigations Related to Improve the Power System Stability Using SMES System.

Research problem	Configuration of the system	Control approach	References
Subsynchronous resonance	The first model of IEEE second benchmark model	PI	(Rahim et al., 1996)
		PID with pattern search	(Farahani, 2012)
		Neural network-NN	(Farahani and Ganjefar, 2013)
	The second model of IEEE second benchmark model	PID	(Wu and Lee, 1993; Wang and Tseng, 1999)
		Adaptive neural network	(Rabbani et al., 1999)
Transient stability	A six-machine system	PBC with adaptive L_2 disturbance	(Wang et al., 2006)
		Kinetic energy control	(Ngamroo and Vachirasricirikul, 2013)
	New England	Fuzzy controller	(Sadeghzadeh et al., 1999)
	Single-machine infinite-bus	Fuzzy controller, PI	(Sadeghzadeh et al., 1998; Rahim and Nowicki, 2005)
		Direct feedback linearization	(Tan and Wang, 2004)
		Feedback linearization and linear H_∞ control	(Liu et al., 2004)
		IDA-PBC and H_∞	(Wan and Zhao, 2013)
		Energy function based	(Shi et al., 2010, 2012)
		Immersion and invariance control	(Kanchanaharuthai et al., 2015)
		Fuzzy logic-controlled or PI	(Ali et al., 2007; Rabbani et al., 1998; Mitani et al., 1987, 1988)
		PI	(Ngamroo and Vachirasricirikul, 2012)
	IEEJ WEST ten-machine	Fuzzy logic-controlled	(Ali et al., 2008)
	A six-machine system	Tube-based MPC	(Kiaei and Lotfifard, 2017)
	Multi-machine infinite-bus system	Logic controller	(Taguchi et al., 2007)
	Three areas four machines power system	H_∞ controller	(Ngamroo, 2011)

to these previous works, the main contributions of this dissertation in relation to SMES system are:

- A methodology to compute the active and reactive power references for the improvement of power oscillations in a power system is presented. The proposed methodology is also based on a washout–filter.
- A DPC for SMES system is developed and its impact on the power system stability transient with penetration of PV plants is studied.

1.3.4 Summary of investigations related to HVDC systems

Several studies on modeling and control of VSC–HVDC systems have been based on conventional vector control developed with PI loops (Li et al., 2010; Giddani et al., 2013). However, the performance of these controllers depends heavily on their parameters, which are tuned by the one–point linearization of the original system. This entails that if the operating conditions of the system vary according to the point linearization, its performance may be degraded (Li et al., 2010; Meah and Ula, 2010). To address this problem, many investigations have been proposed, such as adaptive parallel multi–PI controller (Meah and Ula, 2010), model predictive control (Fuchs et al., 2014), feedback linearization control (Ruan et al., 2007), sliding mode control (Ramadan et al., 2012), feedback linearization based sliding mode control (Moharana and Dash, 2010), feed–forward control (Schmuck et al., 2014), perturbation observer based sliding–mode control (Yang et al., 2016b), power–synchronization control (Zhang et al., 2011), multi–variable optimal control (Beccuti et al., 2014), and passive control (Yang et al., 2018a). Despite this, all investigations present high performance, and all of them are designed in a stationary reference frame also known as *dq*—reference frame. This indicates that their performance is highly dependent on current decoupling entirety, which is typically done with a PLL. The PLL introduces time delays that will considerately degrade the performance of the system. Besides, the interaction between the PLL

and the network impedance under different operation conditions may generate stability problems (Leon et al., 2010; Dong et al., 2015).

A model for the VSC based on instantaneous active and reactive power called DPC avoids using the PLL and all the problems it contain (Song et al., 2016). The DPC model transforms the VSC model in the $\alpha\beta$ reference frame to a static two–phase reference frame, which does not require the synchronous reference transformation, therefore facilitating its implementation (Gui et al., 2018). The authors of (Yang et al., 2017b) adopted the DPC model for the VSC–HVDC system applications. They proposed an integral plus resonant sliding mode DPC for the VSC–HVDC systems considering the unbalanced network voltage conditions. However, the control scheme did not take into account the dc side dynamics, which do not allow guaranteeing of the VSC–HVDC system, thus ensuring its robust operation. Different from the previous work, we present a passivity–based controller for the VSC–HVDC systems. This controller takes advantage of the passive structure of the VSC–HVDC system in open–loop to propose a control law that guarantees asymptotically stable using Lyapunov's theory and retaining its structure passive in closed–loop. The main contributions of this dissertation for HVDC system are as follows:

- A full mathematical model for a two–terminal VSC–HVDC system based on direct power control is presented. This model considers ac and dc electrical dynamics.
- A PI controller design based on passivity theory for a two–terminal VSC–HVDC system is described.
- An evaluation of the performance of the PI–PBC for the VSC–HVDC system under conditions of stable and transient response to demonstrate its robustness is shown. An evaluation considering uncertainties of the resistance and inductance is also presented. Additionally, the PI–PBC is compared to a conventional PI controller and a perturbation observer-based adaptive passive control proposed in (Yang et al., 2017a), whose results verify the effectiveness of PI–PBC against PI and POAPC controllers in all scenarios considered.

1.3.5 Summary of investigations related to small hydro–power plant

Small hydro–power plants (SHPs) are a striking distributed energy sources due to their low impact on the environment, the capacity to forecast production and to improve power generation stability compared to other kinds of renewable energy sources such as photovoltaic and wind power (Borkowski, 2018). A SHP is usually composed by a reservoir, water tunnel, penstock, hydraulic turbine, speed governor, and generator. An SHP is a system that has strong coupling between mechanical, hydraulic and electrical dynamics and this makes the system difficult to analyze (Xu and Qian, 2015). Besides, it presents many different operating points which also complicate its analysis (Borkowski, 2018). These features make that the design and control of the governor system are challenging.

Several works have been focused on proposing controller for governor systems. Typically, two types of governor systems can be found in literature which are PID (Fang et al., 2008; Natarajan, 2005; Fang et al., 2011) and state feedback controller (Jones and Mansoor, 2004; Kishor and Singh,

2007; Guo et al., 2015; Chen et al., 2014). The design of PID controllers is based on system outputs which do not use the internal information of SHP. Therefore, it is not possible to guarantee the stability at all operating points because it loses information about its dynamics. In the case of state feedback controllers, several controllers have been proposed such as nonlinear control (Guo et al., 2015; Chen et al., 2014), intelligent method control (Kishor and Singh, 2007), sliding mode control (Yuan et al., 2016; Xu and Qian, 2015), fuzzy control (Cerman and Hušek, 2012; Nagode and Škrjanc, 2014; Li et al., 2017a), fault tolerant control (Simani et al., 2016), predictive control (Jones and Mansoor, 2004; Zhang et al., 2015), synergetic control (Zhu et al., 2017) and finite–time control (Ma et al., 2018). However, these controllers present problems as difficult adaptation to the large–scale requirements, adjust of parameters, on–line optimization process, problems by the initial state of the system, change of the control rules or stability problems, among other (Ma et al., 2018). In addition, some of these investigations analyze only hydraulic and mechanical dynamics without taking into account electrical dynamics.

In case of SHP integrated through the power electronic converters exist few works that analyze all dynamical system. In (Borkowski and Wegiel, 2013) and (Borkowski, 2017), a model SHP integrated to the ac grid via permanent magnet synchronous generator (PMSG), diode bridge rectifier, boost converter and voltage source converter (VSC) was studied; this model was improved in (Borkowski, 2018), presenting a detailed analysis that considers the electrical power losses to achieve high efficiency. In (Marquez et al., 2010), a multi–level hierarchical structure based on PI controller was proposed, however, in that work, hydraulic dynamics were not considered. Different from these previous works, we take advantage of the pH structure that presents SHP in open–loop to design a controller based on passivity theory that keeps its pH structure in closed–loop and guarantees asymptotically stable in the sense of Lyapunov. The main contributions of the dissertation in this aspect are:

- A mathematical model for a SHP employing a PMSG which is connected to the grid through a *back–to–back* converter is presented. This model contains hydraulic, mechanical and electrical (PMSG and VSC) dynamics. All of them show as a pH structure.
- A controller based on passivity theory for SHP is designed. The PBC is employed since mathematical model for SHP in open–loop exhibits a passive structure which makes it suitable to apply the passivity theory. The proposed control considers the complete non–linear model of the system and guarantees local asymptotic stability in the sense of Lyapunov maintaining its passive structure.
- An analysis of the performance of the proposed controller under conditions of stable and transient response to demonstrate its robustness is shown.

1.4 Dissertation Aims

1.4.1 General Aim

To design passivity–based controllers for a hydro–turbine governing system, photovoltaic plant, and superconducting magnetic energy storage system with the final purpose of improving the dynamics performance in a hydro–solar power system guaranteeing its stability in closed–loop using Lyapunov's theory.

1.4.2 Specific Aims

1. To study mathematical models that provide a complete description of the dynamic behavior of hydro–turbine governing systems, photovoltaic solar plant, and superconducting magnetic energy storage systems.
2. To propose a passivity–based control for hydro–turbine governing systems.
3. To propose a passivity–based control for photovoltaic solar plants.
4. To propose a passivity–based control for superconducting magnetic energy storage systems.
5. To assess the proposed controller for hydro–turbine governing system, photovoltaic plant, and superconducting magnetic energy storage system.

1.5 Scope

This dissertation is focused on designing controls based on passivity theory for the HGTS, PV plants and SMES system for improving the dynamic response in hydro–dominant power system with high–level penetration of PV plants. Since it is not possible to face all the transient problems in just one dissertation, we delimit this research, as follows.

- ✓ The proposed methodology is assessed in the 12–bus test system, which has been employed for stability studies in power system transient with high–level penetration using renewable energy sources, for example in (Remon et al., 2017,b; Mukerjee and Lee, 2014; Remon et al., 2017; Zeni et al., 2016).
- ✓ The HTGS model considers $6n$-order model for the synchronous machines and penstock, which is the HTGS model more common in the Colombian power system (Pico et al., 2012).
- ✓ Unbalances are not considered for the test systems.
- ✓ All the states are available for measurement and the nominal parameters of HTGSs, the PV plants, and the SMES system are known.
- ✓ It is only considered a two–terminal VSC–HVDC system.

1.6 List of Publications

Next, the main results derived from this dissertation are presented.

1.6.1 Journal Papers Derived From this Dissertation

1. **W. Gil–González**, and A. Garcés, and O. Fosso, and A. Escobar–Mejía, "Passivity-Based Control of Power Systems Considering Hydro-Turbine with Surge Tank," in *IEEE Transactions on Power Systems*, early access, **2019**, pp 1–1. 10.1109/TPWRS.2019.294836. **SJR 2019 Q1**.

2. **W. Gil–González**, and O. D. Montoya and A. Garcés., "Standard passivity-based control for multi-hydro-turbine governing systems with surge tank," in *Applied Mathematical Modelling*, vol 79, **2020**, pp 1–17. https://www.sciencedirect.com/science/article/pii/S0307904X19306754. **SJR 2019 Q1**.

3. **W. Gil–González**, and O. D. Montoya and A. Garcés., "Modeling and Control of a Small Hydro–Power Plant for a DC Microgrid," in *Electric Power Systems Research*, vol 180, **2020**, pp 106104. https://www.sciencedirect.com/science/article/pii/S0378779619304237. **SJR 2019 Q1**.

4. **W. Gil–González**, and O. D. Montoya and A. Garcés., "Direct power control for VSC-HVDC systems: An application of the global tracking passivity-based PI approach," *International Journal of Electrical Power & Energy Systems*, vol 110, pp 588–597, Sept, **2019**. https://www.sciencedirect.com/science/article/pii/S0142061518333519?dgcid=author. **SJR 2019 Q1**.

5. **W. Gil–González**, and O. D. Montoya and A. Garcés., "Direct power control of electrical energy storage systems: A passivity-based PI approach," *Electric Power Systems Research*, vol 175, pp 105885, Oct, **2019**. https://www.sciencedirect.com/science/article/pii/S0378779619302044?dgcid=author. **SJR 2019 Q1**.

6. **W. Gil–González**, and A. Garcés and A. Escobar–Mejía., "Passivity–based control and stability analysis for hydro–turbine governing systems," *Applied Mathematical Modelling*, vol 68, pp 471–486, April, **2019**. http://www.sciencedirect.com/science/article/pii/S0307904X18305870. **SJR 2019 Q1**.

7. **W. Gil–González**, and O. D. Montoya and A. Garcés., "Control of a SMES for mitigating subsynchronous oscillations in power systems: A PBC–PI approach," *Journal of Energy Storage*, vol 20, **2018**, pp 163–172. https://www.sciencedirect.com/science/article/pii/S2352152X18303852. **SJR 2019 Q1**.

8. **W. Gil–González**, and O. D. Montoya., "Passivity–based PI control of a SMES system to support power in electrical grids: A bilinear approach," in *Journal of Energy Storage*, vol 18, **2018**, pp 459–466. https://doi.org/10.1016/j.est.2018.05.020. **SJR 2019 Q1**.

The following works are currently under review:

9. **W. Gil–González**, and O. D. Montoya, "Control of photovoltaic plants interconnected through a VSC for the improvement of power oscillations in a power system," *Engineering Science and Technology, an International Journal*. **SJR 2019 Q1**.

10. **W. Gil–González**, and A. Garcés, and O. Fosso, "Passivity-based control for a small hydro-power plant," *Renewable Energy*. **SJR 2019 Q1**.

11. **W. Gil–González**, and O. D. Montoya and A. Garcés, "Bilinear control for three-phase microgrids: a proportional-integral passivity-based design," *Electric Power Components and Systems*. **SJR 2019 Q2**.

1.6.2 Additional Journal Papers

1. **W. Gil–González**, O. D. Montoya and A. Garces., "Economic dispatch of energy storage systems in dc microgrids employing a semidefinite programming model," *Journal of Energy Storage*, vol 21, Feb. **2019**, pp 1–8. https://doi.org/10.1016/j.est.2018.10.025. **SJR 2019 Q1** .

2. **W. Gil–González** and O. D. Montoya, "Active and reactive power conditioning using SMES devices with PMW–CSC: A feedback nonlinear control approach," *Ain Shams Engineering Journal*, early access, **2019**, pp 1–10. https://www.sciencedirect.com/science/article/pii/S209044791930005X. **SJR 2019 Q1** .

3. **W. Gil–González**, and A. Garcés and A. Escobar–Mejía., "A generalized model and control for supermagnetic and supercapacitor energy storage," *Ingeniería y Ciencia*, vol. 13, no 26, **2017**, pp. 147–171. http://www.scielo.org.co/scielo.php?script=sci_arttext&pid=S1794-91652017000200147. **Colciencias Q3** .

1.6.3 Other Journals as Coauthor

1. O. D. Montoya, **W. Gil–González** and L. F. Grisales–Noreña, "Relaxed convex model for optimal location and sizing of DGs in DC grids using sequential quadratic programming and random hyperplane approaches," International Journal of Electrical Power & Energy Systems 115, **2020**, pp 105442. https://www.sciencedirect.com/science/article/pii/S014206151930242X. **SJR 2019 Q1**.

2. L. F. Grisales–Noreña, and O. D. Montoya, **W. Gil–González**, "Integration of energy storage systems in AC distribution networks: Optimal location, selecting, and operation approach based on genetic algorithms," Journal of Energy Storage 25, **2019**, pp 100891. https://www.sciencedirect.com/science/article/pii/S2352152X19301835. **SJR 2019 Q1**.

3. O. D. Montoya, **W. Gil–González** and L. F. Grisales–Noreña, "Vortex Search Algorithm for Optimal Power Flow Analysis in DC Resistive Networks with CPLs," *IEEE Transactions on*

Circuits and Systems II: Express Briefs, early access, **2019**, pp 1–5. https://ieeexplore.ieee.org/document/8821394. **SJR 2019 Q1**.

4. O. D. Montoya, **W. Gil–González** and A. Garces, "Distributed energy resources integration in single-phase microgrids: An application of IDA-PBC and PI-PBC approaches," International Journal of Electrical Power & Energy Systems 112, **2019**, pp 221–231. https://www.sciencedirect.com/science/article/pii/S0142061518324359. **SJR 2019 Q1**

5. O. D. Montoya, **W. Gil–González** and V. Garrido, "Voltage Stability Margin in DC Grids with CPLs: A Recursive Newton–Raphson Approximation," *IEEE Transactions on Circuits and Systems II: Express Briefs*, early access, **2019**, pp 1–5. https://ieeexplore.ieee.org/document/8664198. **SJR 2019 Q1**.

6. O. D. Montoya, **W. Gil–González** and A. Garces, "Sequential quadratic programming models for solving the OPF problem in DC grids," *Electric Power Systems Research*, vol 169, April **2019**, pp 18–23. https://doi.org/10.1016/j.epsr.2018.12.008. **SJR 2019 Q1**.

7. O. D. Montoya, V. M. Garrido, **W. Gil–González** and L. F. Grisales–Noreña, "Power Flow Analysis in DC Grids: Two Alternative Numerical Methods," *IEEE Transactions on Circuits and Systems II: Express Briefs*, early access, **2019**, pp 1–5. https://ieeexplore.ieee.org/document/8606244. **SJR 2019 Q1**.

8. O. D. Montoya, **W. Gil–González**, and A. Garces., "Control for EESS in Three–Phase Microgrids Under Time–Domain Reference Frame via PBC Theory," in *IEEE Transactions on Circuits and Systems II: Express Briefs*, early access, **2019**, pp 1–5. https://ieeexplore.ieee.org/document/8618425. **SJR 2019 Q1** .

9. O. D. Montoya, and **W. Gil–González**., "Time–Domain Analysis for Current Control in Single–Phase Distribution Networks Using SMES Devices with PWM–CSCs," in *Electric Power Components and Systems*, **2019**, pp 1–10. https://doi.org/10.1080/15325008.2018.1531325. **SJR 2019 Q2** .

10. O. D. Montoya, **W. Gil–González** and A. Garces., "Optimal Power Flow on DC Microgrids: A Quadratic Convex Approximation," *IEEE Transactions on Circuits and Systems II: Express Briefs*, early access, **2018**, pp 1–5. https://ieeexplore-ieee-org.ezproxy.utp.edu.co/document/8469013. **SJR 2019 Q1**.

11. O. D. Montoya, **W. Gil–González**, A. Garcés, and G. Espinosa–Pérez., "Indirect IDA–PBC for Active and Reactive Power Support in Distribution Networks Using SMES Systems with PWM–CSC," in *Journal of Energy Storage*, vol 17, **2018**, pp 261–271. https://doi.org/10.1016/j.est.2018.03.004. **SJR 2019 Q1** .

12. O. D. Montoya, **W. Gil–González**, and F. M. Serra., "PBC Approach for SMES Devices in Electric Distribution Networks," in *IEEE Transactions on Circuits and Systems II: Express*

Briefs, vol. 65, no. 12, pp. 2003–2007, Dec. **2018**. https://ieeexplore.ieee.org/document/8290947/. **SJR 2019 Q1** .

1.6.4 Conference Papers

1. **W. Gil–González**, A. Garces, A. Escobar–Mejía and O. Danilo Montoya, "Passivity–Based Control for Hydro-Turbine Governing Systems," 2018 IEEE PES Transmission & Distribution Conference and Exhibition - Latin America (T&D–LA), Lima, 2018, pp. 1–5. https://ieeexplore.ieee.org/abstract/document/8511641.

2. **W. Gil–González**, O. D. Montoya, A. Garcés and G. Espinosa–Pérez., "IDA Passivity–Based Control for Superconducting Magnetic Energy Storage with PWM–CSC," *2017 Ninth Annual IEEE Green Technologies Conference (GreenTech)*, Denver, CO, **2017**, pp. 89–95. https://ieeexplore.ieee.org/document/7923943/.

3. **W. Gil–González**, O. D. Montoya, A. Garcés and A. Escobar–Mejía., "Supervisory LMI–Based State–Feedback Control for Current Source Power Conditioning of SMES," *2017 Ninth Annual IEEE Green Technologies Conference (GreenTech)*, Denver, CO, **2017**, pp. 145–150. https://ieeexplore.ieee.org/document/7923951/.

1.6.5 Additional Conference Papers

1. **W. Gil–González**, O. D. Montoya, A. Garcés, F. M. Serra, and G. Magaldi, "Output Voltage Regulation For dc–dc Buck Converters: a Passivity-–Based PI Design," *2019 IEEE 10th Latin American Symposium on Circuits & Systems (LASCAS)*, Armenia, Quindío, Colombia., Feb. **2018**. **2019**. https://ieeexplore.ieee.org/document/8667557

2. O. D. Montoya, V. M. Garrido, **W. Gil-González**, A. Garces, and L. F. Grisales-Noreña ., "Controller Design for VSCs in Distributed Generation Applications: an IDA-PBC Approach," *2018 IEEE International Autumn Meeting on Power, Electronics and Computing (ROPEC 2018)*, Ixtapa, Mexico., Nov. **2018**. https://ieeexplore.ieee.org/document/8661360

3. O. D. Montoya, V. M. Garrido, **W. Gil-González**, E. Holguín, and A. Garces., "An Exact Feedback Linearization Control of a SMES System to Support Power in Electrical Grids," *IEEE 2018 9th Power, Instrumentation and Measurement Meeting (EPIM 2018)*, Salto, Uru., Nov. **2018**.

4. O. D. Montoya, J. E. Campillo, **W. Gil-González**, and A. Garces., "Integration of PV Arrays in DC Power Grids via Unidirectional Boost Converters: a PBC Approach," *IEEE 2018 9th Power, Instrumentation and Measurement Meeting (EPIM 2018)*, Salto, Uru., Nov. **2018**.

5. O. D. Montoya, **W. Gil-González**, and A. Garcés., "SCES Integration in Power Grids: a PBC Approach under ABC, $\alpha\beta 0$ and dq0 Reference Frames," *2018 IEEE PES Transmission*

and Distribution Conference and Exhibition – Latin America (T&D LA 2018), Lima, Perú, Sept. **2018**, pp. 1–5. https://ieeexplore.ieee.org/document/8511707

6. O. D. Montoya, **W. Gil-González**, A. Escobar-Mejía, A. Garcés, and L. F. Grisales., "Nonlinear Control for Battery Energy Storage Systems in Power Grids," *2018 IEEE Green Technologies Conference (GreenTech)*, Austin, TX, **2018**, pp. 65-70. https://ieeexplore.ieee.org/document/8373604/

1.7 Outline

This dissertation is organized as follows.

Chapter 2 reviews the main concept related to port–Hamiltonian systems and passivity–based control theory applied to affine and non–affine system.

Chapter 3 describes the mathematical modeling associated with the HTGS, PV plants, SMES system, VSC–HVDC system and electrical network. The DPC model for PV plants, SMES system, and VSC–HVDC system is also developed. Each mathematical modeling is condensed into a pH model.

Chapter 4 presents the control design for the HTGS, PV plants, SMES system, and VSC–HVDC system based on PBC theory. In addition, it shows the proposed methodology of the power oscillation damper for the PV plants and the SMES system.

Chapter 5 presents the test system used to assess the performance and robustness controller. The scenarios and cases to test the proposed controllers are described, and their respective results are analyzed.

Chapter 6 presents the conclusions and summarizes possible future researches.

Appendix A shows a PBC for a small hydro–power plant and its performance is tested and compared with a conventional PI controller in a 13.2 kV distribution feeder. This appendix shows a different application of PBC theory on a related subject. The study of a small hydropower plant is beyond the objective of this dissertation but it shows some advances in the integration of renewable energies at the level of distribution systems.

Appendix B presents all data parameters used in this dissertation.

Chapter 2

Preliminaries

This chapter describes the main concepts of Lyapunov's theory and Hamiltonian system, focusing on system with port–Hamiltonian structure. In addition, the control design for non–linear system based on passivity theory such as interconnection and damping assignment as well as proportional–integral control for affine and non–affine systems are presented.

2.1 Notation

We denote the n–by–n identity matrix by 1_n, an n–by–n null matrix by 0_n and an n–by–m null matrix by $0_{n\times m}$. The diagonal matrix with diagonal elements $d_1, ..., d_n$ is denoted by $diag(d_1, ..., d_n)$ and any column vector with n-elements is denoted by $\text{col}(d_1, ..., d_n)$. $x \in \mathbb{R}^n$ is the state vector and $u \in \mathbb{R}^m$, $(m \leq n)$ is the control input. The gradient of a scalar field y with respect to $x = (x_1, ..., x_n)$ is a vector given by $\frac{\partial y}{\partial x} = \left[\frac{\partial y}{\partial x_1} \; ... \; \frac{\partial y}{\partial x_n}\right]^\top$. Therefore, the gradient is assumed as a column vector. Any matrix R is positive semidefinite symmetric and meets $R = R^\top \succ 0$. Any matrix $J \in \mathbb{R}^{n\times n}$ is skew–symmetric; hence it satisfies that $J = -J^\top$, and

$$J_2 = \begin{bmatrix} 0 & -1 \\ 1 & 0 \end{bmatrix}.$$

2.2 Lyapunov's Theory

Lyapunov stability theory is a standard theory and one of the most important tools in the stability analysis of nonlinear systems (Khalil, 2002). Consider the following nonlinear autonomous system:

$$\frac{d}{dt}x = f(x), \tag{2.1}$$

where $f : \mathcal{D} \longrightarrow \mathbb{R}^n$ is a locally Lipschitz map from the domain $\mathcal{D} \subseteq \mathbb{R}^n$ to $\mathbb{R}^n$. Suppose that the system shown in (2.1) has an equilibrium point in $x^* \in \mathcal{D}$ (i.e., $f(x^*) = 0$). The method of

Lyapunov allows identifying sufficient conditions for the stability of the equilibrium point x^*. First, it assumes that x^* is the origin of state space. This does not mean that generality is lost since we can always apply a change of variables to $\xi = x - x^*$ to obtain (Khalil, 2002; Vidyasagar, 2002):

$$\frac{d}{dt}\xi = f(\xi + x^*) \equiv g(\xi).$$

Now, the stability study is done for the new system with respect to $\xi = 0$. Two types of stability are analyzed (Khalil, 2002).

Definition 1 (Lyapunov's stability) *The equilibrium point $x = 0$ of (2.1) is*

1. ***Stable** if, for each $\epsilon > 0$, there exists a $\alpha = \alpha(\epsilon) > 0$ such that*

$$\|x(t_0)\| < \alpha \Rightarrow \|x(t_0)\| < \epsilon, \ \forall \ t > t_0.$$

2. ***Asymptotically stable** if, it is stable and α can be chosen such that*

$$\|x(t_0)\| < \alpha \Rightarrow \lim_{t \longrightarrow \infty} x(t) = 0.$$

Also, it defined unstable if, it is not stable.

The stability can be determined by means of functions which are defined in the state space (Khalil, 2002). As presented in the following result:

Theorem 2.2.1 (Lyapunov's Theorem) *Consider the system (2.1) and suppose that there exists a continuously differentiable function $W : \mathcal{D} \longrightarrow \mathbb{R}$ such that*

$$\begin{array}{rcll} W(0) & = & 0, & \\ W(x) & > & 0, & x \in \ \mathcal{D} \ \forall \ x \neq 0 \\ \dot{W}(x) & = & \dfrac{\partial W}{\partial x} f(x) \leq 0, & x \in \ \mathcal{D}. \end{array} \tag{2.2}$$

If the above is true, the equilibrium point is stable in the sense of Lyapunov. If it also meets

$$\dot{W}(x) = \frac{\partial W}{\partial x} f(x) < 0, \quad x \in \ \mathcal{D},$$

then, the equilibrium point is asymptotically stable.

Fig. 2.1 illustrates the differences among stability in the sense of Lyapunov, asymptotic stability and unstable.

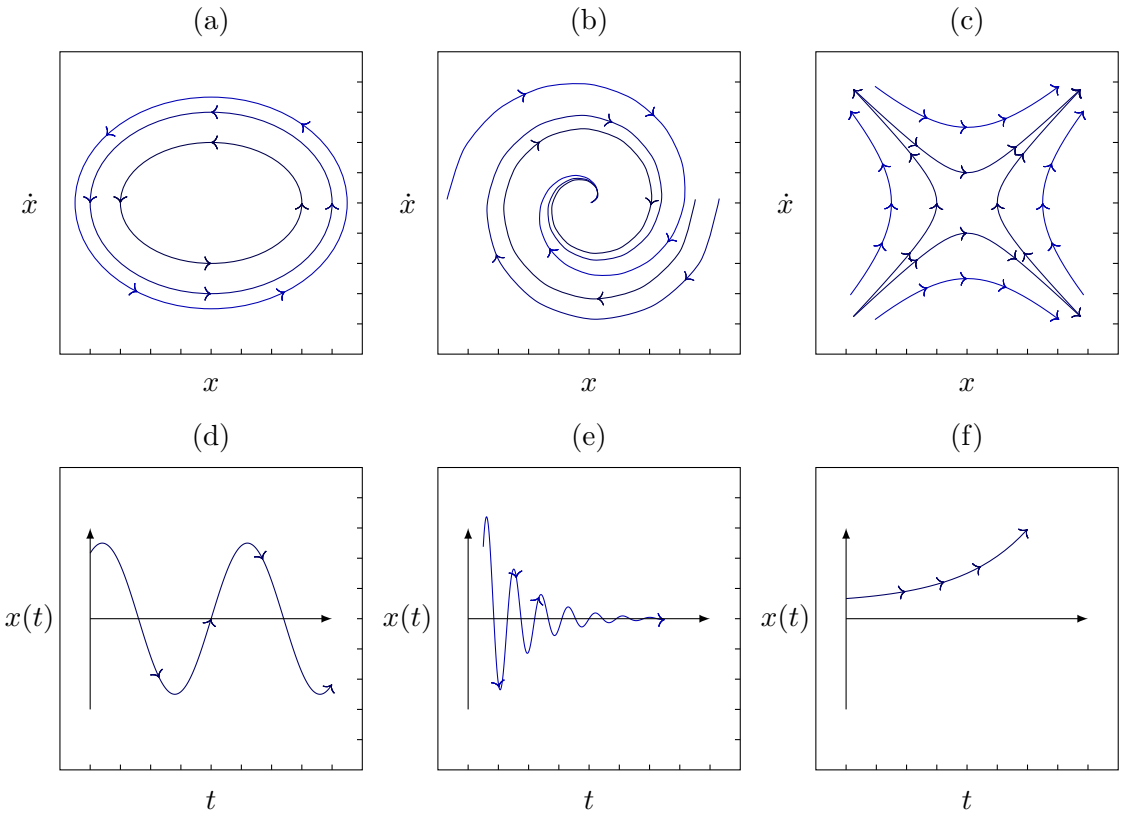

Figure 2.1: Phase portrait for stable and unstable equilibrium point: (a) Stable in the sense of Lyapunov, (b) Asymptotically stable, (c) Unstable (saddle), (d) time domain for an stable equilibrium point, (e) time domain for an asymptotically stable equilibrium point, and (f) dynamic behavior of an unstable equilibrium point.

2.3 Passivity

Passivity is an intrinsic property of some systems, especially electromechanical (Ortega et al., 2013). Consider the dynamic system presented in Fig. 2.2, where $f : \mathbb{R}^n \times \mathbb{R}^m \mapsto \mathbb{R}^n$ is locally Lipschitz map, $h : \mathbb{R}^n \times \mathbb{R}^m \mapsto \mathbb{R}^m$ is a continuous mapping, $f(0,0) = 0$ and $h(0,0) = 0$. The system shown in Fig. 2.2 is passive if the energy it absorbs in any period $[0,\ t]$, is greater than or equal to the increase in stored energy by the system in the same time, i.e.,

$$\int_0^t u(\tau)y(\tau)d\tau \geq S(x) - S(x(0)), \tag{2.3}$$

where $S(x)$ is an energy like function. Because (2.3) must be met for all $t \geq 0$, the internal power flow of the system must be greater than or equal to the rate of change of the energy stored. Which

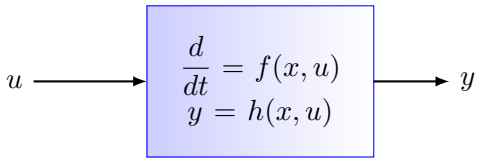

Figure 2.2: Generic representation of a nonlinear dynamical system.

is expressed in the following definition.

Definition 2 (Passive system) *The system shown in Fig. 2.2 is passive if there exists a continuously differentiable positive-semidefinite function $S(x)$, called storage function such that*

$$u^T y \geq \dot{S}(x) = \frac{\partial S}{\partial x} f(x,u),\ \forall (x,u) \in \mathbb{R}^n \times \mathbb{R}^m.$$

Moreover, it is said to be a system

- *Lossless if $u^\top y = \dot{S}(x)$.*
- *Strictly passive if $u^\top y = \dot{S}(x) + S_d(x)$, with $S_d(x) \succeq 0$ (called as dissipative function).*

2.4 Port–Hamiltonian Systems

We shall consider nonlinear port–Hamiltonian (pH) systems with dissipation, whose dynamics can be described as follows

$$\begin{aligned} \mathcal{P}\frac{d}{dt}x &= (J(x,u) - R(x))\frac{\partial H(x)}{\partial x} + g(x)u, \\ y &= g(x)^T \frac{\partial H}{\partial x}, \end{aligned} \tag{2.4}$$

where $x \in \mathbb{R}^n$ is the state (or Hamiltonian variables) vector, $R(x) = R^\top(x) \in {\mathbb{R}_+}^{n\times n}$ is the positive semidefinite symmetric dissipation matrix, and $J(x,u) \in \mathbb{R}^{n\times n}$ is a skew–symmetric matrix called the interconnection matrix, which satisfies $J(x,u) + J(x,u)^\top = 0$, and $\mathcal{P} \in \mathbb{R}^{n\times n}$ is the inertial matrix. $H(x) \in \mathbb{R}_+$ denotes the energy of the system known Hamiltonian function, $g(x) \in \mathbb{R}^{n\times m}$ represents the input force matrix and $g(x)$ denotes the generalized forces resulting from the control inputs $u \in \mathbb{R}^m$. $y \in \mathbb{R}^m$ is the output function and the inner product between u and y defines *supply rate* of the system.

The pH system (2.4) is passive and satisfies Definition 2. Taking derivative of $H(x)$ with respect

to t along trajectories of (2.4) is

$$\begin{aligned}\dot{H}(x) =& \frac{\partial H(x)}{\partial x}^{\top} \mathcal{P}\dot{x}, = \frac{\partial H(x)}{\partial x}^{\top} \left((J(x,u) - R(x)) \frac{\partial H(x)}{\partial x} + g(x)u \right), \\ =& \frac{\partial H(x)}{\partial x}^{\top} (J(x,u) - R(x)) \frac{\partial H(x)}{\partial x} + \frac{\partial H(x)}{\partial x}^{\top} g(x)u, \\ =& - \frac{\partial H(x)}{\partial x}^{\top} R(x) \frac{\partial H(x)}{\partial x} + u^{\top} y.\end{aligned} \tag{2.5}$$

From (2.5) it is easy to notice that if $R(x) \succeq 0$ is positive semidefinite, then, it is possible to obtain the following relationship

$$\dot{H}(x) \leq u^{\top} y. \tag{2.6}$$

Remark 1 *Note that* (2.6) *is a passive pH system since the change in the total energy stored is less than or equal to* $u^{\top}y, \forall t \geq 0$ *(van der Schaft, 2017), as described in Definition 2.*

2.5 Passivity–Based Control Theory

Passivity–based control (PBC) is a technique designed for concentrated parameter systems interconnected to the external environment via some port power variables u and y, which are combined in the sense that their product turns out to be power units (i.e., voltages and currents in electrical systems, or forces and speeds in mechanical systems) (Ortega et al., 2001). This technique is used for linear and nonlinear controllers which has shown to be of great utility for the solution of control problems related to physical systems, in particular for mechanical and electrical systems (van der Schaft, 2017).

The PBC seeks to incorporate energy principles in the design of controllers, making both the plant and the controller appear as interconnected power transformers (Ortega et al., 2013). If the system is controlled, have a physical structure and satisfy the energy balances, then it is possible to say that the problem reduces to assigning a new energy function. There are two PBC approaches are common in the literature: interconnection and damping assignment passivity–based control (IDA–PBC) (Ortega et al., 2002; van der Schaft, 2017) and proportional–integral passivity–based control (PI–PBC) (Cisneros et al., 2015; Aranovskiy et al., 2016). The use of these approaches depends on the structure in open–loop system under study, i.e., the IDA–PBC is more adequate for nonlinear systems with affine structure (e.g., hydro and thermal power plants), while the PI–PBC is ideal for bilinear systems, such as these integrated by electronic power converters (e.g., wind and solar generation and energy storage systems) (Ortega et al., 2013; van der Schaft, 2017; Gil-González et al., 2019; Gil-González and Montoya, 2018).

The IDA–PBC and PI–PBC methods allow a design of a feedback loop that stabilize a nonlinear system given by

$$\frac{d}{dt}x = f(x) + g(x)u + d. \tag{2.7}$$

where $d \in \mathbb{R}^n$ is an external vector.

2.5.1 Control via IDA–PBC

The IDA–PBC technique seeks to design a control input such as the closed–loop system has a pH structure, where the storage function, interconnection and damping matrices will have the desired structure, such that the point of equilibrium (minimum energy desired) will be stable (Ortega et al., 2002; van der Schaft, 2017). The pH system in closed–loop is presented as follows:

$$\mathcal{P}\frac{d}{dt}x = (J_d - R_d)\frac{\partial H_d(x)}{\partial x}, \tag{2.8}$$

where $J_d = -J_d^\top$ is a desired interconnection matrix which allows interconnect the controlled variables with non–controlled variables (Ortega et al., 2002). $R_d \succ 0$ is the desired damping matrix which is conventionally chosen as diagonal positive definite matrix (Ortega et al., 2002; van der Schaft, 2017). $H_d(x)$ is the desired Hamiltonian function which represents the total stored energy of the system and needs to fulfill

$$x^* = \arg\min\ H_d(x), \tag{2.9}$$

where x^* is an assignable point equilibrium.

The main idea of this technique is to transform the system (2.7) into a Hamiltonian system, of the form (2.8) with desired storage function, through the feedback of an adequate control input, such as

$$f(x) + g(x)u + d = (J_d - R_d)\frac{\partial H_d(x)}{\partial x},$$

However, the system (2.8) has only a solution when it is possible to solve the coupling equation, which is given by (2.10).

$$g(x)^\perp \left((J_d - R_d - f(x) - d)\frac{\partial H_d}{\partial x} \right) = 0, \tag{2.10}$$

where $g(x)^\perp$ is a full–rank left annihilator of $g(x)$, i.e., $g(x)^\perp g(x) = 0$ and (2.9) is satisfied. Therefore, the system (2.8) in closed–loop is achieved with the control input

$$u = G(x)\left((J_d - R_d)\frac{\partial H_d}{\partial x} - f(x) - d \right). \tag{2.11}$$

where $G(x) = \left(g(x)^\top g(x)\right)^{-1} g(x)^\top$.

Remark 2 *To apply (2.11), it is necessary that $G(x)$ must be full–rank, which always meets for any affine system, i.e., $G(x)$ is constant.*

To prove the stability of the closed–loop system (2.8) it is possible to select $H_d(x)$ as a quadratic Lyapunov function candidate

$$W(\tilde{x}) = H_d(\tilde{x}) = \frac{1}{2}\tilde{x}^\top \mathcal{P}\tilde{x}, \tag{2.12}$$

where $\tilde{x} = x - x^*$.

Remark 3 *Lyapunov function does not necessarily have to be a quadratic function of a general form it can be represented as* $W(\tilde{x}) = H_d(\tilde{x}) - H_{d_{min}}$. *However, the stability of the system used in this dissertation can be demonstrated using only a quadratic Lyapunov function.*

Note that $W(\tilde{x})$ corresponds to a quadratic positive definite function, which fulfills the first two Lyapunov stability conditions, i.e., $W(\tilde{x})) > 0 \; \forall \; x \neq x^*$ and $W\tilde{x}) = 0 \; \forall \; x = x^*$ (see (2.2)), and its temporal derivative is

$$\begin{aligned} \dot{W}(\tilde{x}) = \dot{H}_d(\tilde{x}) = \tilde{x}\mathcal{P}\dot{\tilde{x}} \; &= \tilde{x}\left(J_d - R_d\right)\tilde{x} \\ &= -\tilde{x}R_d\tilde{x} \leq 0. \end{aligned} \tag{2.13}$$

Remark 4 *The pH system* (2.8) *can present there kind of stability depending on* R_d *in* (2.13) *(Perko, 2013), which are:*

- If $R_d \succeq 0$, then, the pH system (2.8) will be stable in the sense of Lyapunov.
- If $R_d \succ 0$, then, the pH system (2.8) will be asymptotically stable in the sense of Lyapunov.
- If $R_d \succ 0$ and guarantees that $\dot{W}(\tilde{x}) < \beta W(\tilde{x})$, where $\beta \leq \lambda_{min}(\mathcal{P}^{-1}R_d)$, then, the pH system (2.8) will be exponentially stable in the sense of Lyapunov.

2.5.2 Control via PI–PBC

The PI–PBC is a control technique adequate for the bilinear system with pH structure. Any electrical power component integrated to power system via power electronic converters presents a pH structure in open–loop (Hernandez-Gomez et al., 2010; Cisneros et al., 2015). A bilinear system with a pH structure can be defined as

Definition 3 (Bilinear system) *A dynamic bilinear system with pH structure corresponds to a non–affine system in which there exists the product between the control inputs and the state variables with the following structure*

$$\mathcal{P}\frac{d}{dt}x = \left(J_o + \sum_{i=1}^{m} J_i u_i - R\right)x + d. \tag{2.14}$$

Note that an assignable equilibrium of the pH system (2.14) depends on the control inputs u and the external inputs d are bounded. Based on this, the achievable (steady–state) behavior of the pH system (2.14) can be defined as

Definition 4 (Assignable equilibrium point) *An assignable equilibrium point in* (2.14) *is uniquely established by the (constant) vectors* x^*, *such that*

$$0 = \left(J_o + \sum_{i=1}^{m} J_i u_i^* - R\right)x^* + d, \tag{2.15}$$

for some (constant) vector u^*. In other words, from (2.7) the assignable equilibrium point is determined by

$$\left\{x^* \in \mathbb{R}^n \mid g(x^*)^\perp \left(f(x^*) + d\right) = 0\right\},$$

and its corresponding equilibrium control input u^* is univocally determined by

$$u^* = -G(x^*)\left(f(x^*) + d\right). \tag{2.16}$$

2.5.3 Incremental Passivity Model

The PI–PBC technique has been developed for Hamiltonian systems based on the incremental passivity model (Hernandez-Gomez et al., 2010). Since this model allows solving tracking trajectory or regulation problems with a transformation via the incremental model (Hernandez-Gomez et al., 2010; Cisneros et al., 2015). The incremental passivity model for the pH system (2.14) is defined as (2.12).

$$\mathcal{P}\frac{d}{dt}x = \left(J_o + \sum_{i=1}^{m} J_i\left(\tilde{u}_i + u_i^*\right) - R\right)\left(\tilde{x} + x^*\right) + d, \tag{2.17}$$

where $\tilde{(\cdot)} = (\cdot) - (\cdot)^*$ are the incremental variables.

Subtracting (2.15) from (2.17) we obtain (2.18).

$$\mathcal{P}\dot{\tilde{x}} = \left(J_o + \sum_{i=1}^{4} J_i u_i - R\right)\tilde{x} + \left(\sum_{i=1}^{2} J_i \tilde{u}_i\right)x^*. \tag{2.18}$$

The incremental passivity dynamic model is passive if it satisfies Definition 2. We assume that the storage function $S(\tilde{x})$ is

$$S(\tilde{x}) = \frac{1}{2}\tilde{x}^\top \mathcal{P}\tilde{x},$$

whose its derivative along the trajectories of the incremental model (2.18) yields

$$\begin{aligned}
\dot{S}(\tilde{x}) &= \tilde{x}^\top \mathcal{P}\dot{\tilde{x}} \\
&= \tilde{x}^\top \left(\left(J_o + \sum_{i=1}^{m} J_i u_i - R\right)\tilde{x} + \left(\sum_{i=1}^{4} J_i \tilde{u}_i\right)x^*\right) \\
&= -\tilde{x}^\top R\tilde{x} + \tilde{x}^\top \left(\sum_{i=1}^{m} J_i \tilde{u}_i\right)x^* \\
&\leq \tilde{x}^\top \left(\sum_{i=1}^{m} J_i \tilde{u}_i\right)x^* = \tilde{y}^\top \tilde{u},
\end{aligned}$$

The output function $\tilde{y}$ that guarantees the dynamic model of incremental is passive, is

$$\tilde{y} = C(x^*)\tilde{x}, \tag{2.19}$$

with $C : \mathbb{R}^m \longrightarrow \mathbb{R}^{m \times n}$

$$C(x^*) = \begin{bmatrix} {x^*}^\top J_1^\top \\ \vdots \\ {x^*}^\top J_m^\top \end{bmatrix}.$$

This output function $\tilde{y}$ was established in (Hernandez-Gomez et al., 2010).

2.5.4 PI Controller Design

Consider that the pH system (2.14) reaches an admissible point in closed–loop with the PI controller (Hernandez-Gomez et al., 2010; Cisneros et al., 2015):

$$\begin{aligned} \tilde{u} &= -K_p\tilde{y} + K_i z \\ \dot{z} &= -\tilde{y}, \end{aligned}$$

where $K_p = K_p^\top \succ 0$ and $K_i = K_i^\top \succ 0$. For any initial condition, the trajectories in closed–loop of the pH system (2.14) have a bounded range such that

$$\lim_{t \longrightarrow \infty} \tilde{y}(t) = 0.$$

and the equilibrium point $\left(x^*, K_i^{-1}u^*\right)$ is globally asymptotically stable, defining the following radially unbounded Lyapunov function candidates

$$W(\tilde{x}, z) = \frac{1}{2}\tilde{x}^\top \mathcal{P}\tilde{x} + \frac{1}{2}\left(z - K_i^{-1}u^*\right)^\top K_i \left(z - K_i^{-1}u^*\right),$$

where its time derivative is

$$\begin{aligned} \dot{W}(\tilde{x}, z) &= \frac{1}{2}\tilde{x}^\top D\dot{\tilde{x}} + \frac{1}{2}z^\top K_i \dot{z} \\ &= -\tilde{x}^\top R\tilde{x} + \tilde{y}^\top \tilde{u} - \frac{1}{2}z^\top K_i \tilde{y} \\ &= -\tilde{x}^\top R\tilde{x} - \tilde{y}^\top K_p \tilde{y}, \end{aligned}$$

which proves that PI–PBC is stable. The asymptotic convergence is proved in (Hernandez-Gomez et al., 2010).

For a wide overview on passivity–based control, see the excellent books and papers (Ortega et al., 2002; Hernandez-Gomez et al., 2010; Cisneros et al., 2015; van der Schaft, 2017; Ortega et al., 2013).

2.6 Summary of the Chapter

This chapter presented the most important features for the stability analysis of nonlinear systems based on Lyapunov's theory. The concepts passivity and Hamiltonian systems were also presented. Lastly, the design of passivity-based controllers based on interconnection and damping assignment as well as on proportional–integral actions were described for affine and non–affine systems.

Chapter 3

Power System Modeling

This chapter describes the power system model, which includes the dynamics of hydraulic, electrical, and mechanical subsystems of each hydro–turbine governing system as well as photovoltaic solar plants, superconducting coil energy storage, VSC–HVDC system, and the electrical network. Additionally, all the dynamics will be condensed into a port–Hamiltonian model.

All along this dissertation we make the following assumptions:

Assumption 1 *The power system model is a balanced and symmetrical system.*

Assumption 2 *The rotor power angle δ is known, therefore, the Park transformation can be employed.*

Assumption 3 *All the elements that compose the power system can be represented by lumped parameters models.*

3.1 Hydro–Turbine Governing System Modeling

In this subsection hydro–turbine governing system modeling is introduced, which includes the dynamics of hydraulic, electrical, and mechanical. Here each part of the system is described separately.

3.1.1 Hydraulic–Turbine Model

A dynamic model of a hydraulic turbine with penstock and surge tank where incompressible water is assumed, has been recommended by the working group on prime mover and energy supply models (IEEE working group report, 1992; Jiang, 1995b). Fig. 3.1 illustrates a general scheme of the hydroelectric power plant. The dynamic model of a hydraulic turbine with penstock is in per–unit

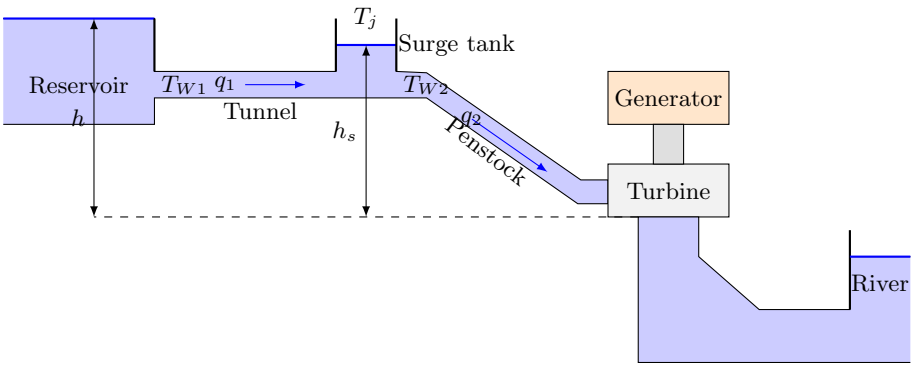

Figure 3.1: A general scheme of the hydro power plant (image taken from (Gil-González et al., 2019)).

values given by:

$$\begin{aligned} T_{W1}\frac{d}{dt}q_1 &= 1 - h_s - k_{f1}q_1^2, \\ T_j\frac{d}{dt}h_s &= q_1 - q_2, \\ T_{W2}\frac{d}{dt}q_2 &= h_s - h - k_{f2}q_2^2, \\ T_y\frac{d}{dt}y &= u_y - y_g, \end{aligned} \tag{3.1}$$

where h and h_s are the head at turbine and the head at surge tank respectively; q_1 and q_2 are the normalized flow rates of tunnel and penstock respectively, and y_g denotes the servomotor position; k_{f1} and k_{f2} are friction losses on conduit respectively. T_{W1} and T_{W2} are the starting time of water in tunnel and penstock, which are defined as:

$$T_W = \frac{Lq_{base}}{Ah_{base}g},$$

where q_{base} is the turbine's flow rate when the gate is fully open; L and A are the length and the area of the tunnel or penstock, respectively, and g is the gravitational acceleration. $T_j = \frac{A_s h_{base}}{q_{base}}$ is a storage constant of the surge tank, where A_s is the cross section area of a surge tank. T_y is the time constant of the servomotor.

The pressure head through the turbine is associated with the flow rate and gate position, assuming that the turbine can be depicted by the valve feature, as follows:

$$h = \left(\frac{q_2}{y_g}\right)^2.$$

To ensure a mathematically stable equilibrium point, we make the next assumptions:

Assumption 4 *The water flow rate of penstock is positive since the water flow rate in normal operation always goes in the same direction. In addition, it is bounded by* q_{nl} *and* 1*, i.e.,* $q_{nl} < q_2 \leq 1$.

Assumption 5 *The gain position in per–unit value is bounded between* $0 < y \leq 1$.

For a wide overview on this subject, see the excellent books and papers (Machowski et al., 2008; Anderson and Fouad, 2003; Xu et al., 2012; IEEE working group report, 1992; Jiang, 1995b).

3.1.2 Mechanical Model

Generally, a synchronous machine is composed of two parts: rotor and stator. The rotor consists of a shaft where the turbine torque is balanced by the electrical torque developed by the synchronous machine (Machowski et al., 2008; Anderson and Fouad, 2003). This shaft rotation can write as a torque acting balance on the rotor shaft as follows:

$$M\frac{d}{dt}\omega = \tau_m - \tau_e - b\omega, \tag{3.2}$$

$$\frac{d}{dt}\delta = \omega - \omega_b, \tag{3.3}$$

where δ is the rotor angle (also known as power angle), M is the inertia of the rotor shaft, b is the friction constant, and ω_b is the synchronous speed ($\omega_b = 2\pi f_b$, f_b is the nominal frequency of the ac grid). τ_m and τ_e are mechanical and electrical torque, which can be written as

$$\tau_m = \frac{A_t q_2^2 \left(q_2 - q_{nl}\right)}{y_g^2 \omega}, \tag{3.4}$$

$$\tau_e = \psi_q i_d - \psi_d i_q,$$

where q_{nl} denotes its no–load and A_t represents the proportionality constant of the hydro–turbine (Machowski et al., 2008).

3.1.3 Synchronous Machine Modeling

The synchronous machine has three identical circuits connected in the stator called *stator windings* (labeled with letters a, b and c). The circuits in the rotor are called *field and damper windings* (labeled with letters f for field winding and, D and Q for damper windings). All the generator windings are magnetically coupled, i.e., that the flux in each winding depends on the currents in all the other windings (Machowski et al., 2008). This relation between flux linkage and currents is in the dq reference frame given by

$$\psi = Li,$$

with,

$$L = \begin{bmatrix} L_{11} & L_{12} \\ L_{12}^{\top} & L_{22} \end{bmatrix} \quad L_{11} = \begin{bmatrix} L_d & 0 \\ 0 & L_q \end{bmatrix} \quad L_{12} = \begin{bmatrix} L_{md} & L_{md} & 0 \\ 0 & 0 & L_{mq} \end{bmatrix} \quad L_{22} = \begin{bmatrix} L_f & L_{md} & 0 \\ L_{md} & L_D & 0 \\ 0 & 0 & L_Q \end{bmatrix},$$

where L_d and L_q represent the stator direct and quadrature inductances, respectively; L_f denotes the field inductance; L_{md} and L_{mq} are the direct and quadrature magnetization inductances, respectively. $\psi = \text{col}(\psi_d, \psi_q, \psi_f, \psi_D, \psi_Q)$, ψ_d and ψ_q represent the stator direct and quadrature axis flux linkages, ψ_f denotes the field flux, ψ_D, and ψ_Q are the rotor damping winding flux linkages; $i = \text{col}(i_d, i_q, i_f, i_D, i_Q)$, i_d and i_q represent the stator direct and quadrature axis currents, i_f denotes the field current, i_D and i_Q are the rotor damping winding currents.

Kirchhoff's voltage law applied to the circuit shown in Fig. 3.2, gives:

$$\frac{d}{dt}\psi = -R_g i + J_\omega \psi - v, \tag{3.5}$$

where $v = \text{col}(v_d, v_q, -v_f, 0, 0)$, v_d and v_q denote the stator direct and quadrature axis voltages, v_f represents the field voltage; $R_g = \text{diag}(r_s, r_s, r_f, r_D, r_Q)$, r_s denotes the stator resistance, r_f represents the field resistance, r_D and r_Q are the rotor damping winding resistances; and

$$J_\omega = \begin{bmatrix} J_2\omega & 0_{2\times 3} \\ 0_{3\times 2} & 0_3 \end{bmatrix}.$$

For a wide overview on synchronous machine model and its deduction from *abc* reference frame to *dq* reference frame, see the excellent book (Machowski et al., 2008, Cap. 11).

3.1.4 Equivalent port–Hamiltonian Model

Starting from the energy properties of the HTGS, it is possible to obtain a mathematical representation of the model given by (3.1) to (3.5) in pH structure. The energy function for the i–th HTGS connected to the power system is given by

$$H_i = H_{ti} + H_{mi} + H_{ei},$$

where H_i is the Hamiltonian energy function for the i–th HTGS, which is composed by the sum of the hydro–turbine energy H_{ti}, mechanical energy H_{mi}, and the electrical energy H_{ei}. The hydro–turbine energy is given by

$$H_{ti} = \frac{1}{2}T_{W1i}x_{1i}^2 + \frac{1}{2}T_{ji}x_{2i}^2 + \frac{A_{ti}x_{3i}^2(x_{3i} - q_{nli})}{x_{4i}},$$

with, $x_{ti} = \text{col}(q_{1i}, h_{si}, q_{2i}, y_i)$ and $\mathcal{P}_{ti} = \text{diag}(T_{W1i}, T_{ji}, T_{W2i}, T_{yi})$.

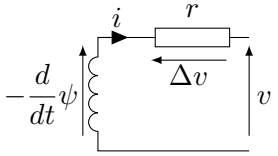

Figure 3.2: Kirchhoff's voltage law applied to the generator circuit.

The kinetic mechanical energy is defined as a quadratic function of the rotor speed

$$H_{mi} = \frac{1}{2} M \omega_i^2,$$

and, the electrical energy is selected as a quadratic function of the rotor fluxes, i.e.,

$$H_{ei} = \frac{1}{2} \psi_i^\top L_i \psi_i.$$

The dynamic systems from (3.1), (3.2), and (3.5) can be rewritten as

$$\mathcal{P}_i \dot{x}_i = (J_i - R_i) \frac{\partial H_i}{\partial x_i} + g_i u_i + d_i + c_i, \tag{3.6}$$

where $x_i = \text{col}(x_{t1}, \omega_i, \psi_i) = \text{col}(x_1, ..., x_{10})$, $u_i = \text{col}(u_{yi}, v_{fi})$, $c_i = \text{col}(0, -x_{3i}, x_{2i}, 0, 0, 0, 0, 0, 0, 0)$, $d_i = \text{col}(1, 0, 0, 0, 0, -v_{di}, -v_{qi}, 0, 0, 0)$, $\mathcal{P}_i = \text{diag}\big(T_{W1i}, T_{ji}, T_{W2i}, T_{yi}, M_i, L_i^{-1}\big)$, $g_i = \begin{bmatrix} 0_{3\times1} & 1 & 0_{6\times1}; & 0_{7\times1} & 1 & 0_{2\times1} \end{bmatrix}^\top$, $R_i = \text{diag}(k_{f1i} x_{1i}, 0, r_{3i}, r_{4i}, b_i, R_{gi}) + R_{2i}$,

$$R_{2i} = \begin{bmatrix} 0_3 & 0_{3\times2} & 0_{3\times5} \\ 0_{2\times3} & \begin{bmatrix} 0 & \frac{1}{2x_{5i}} \\ \frac{1}{2x_{5i}} & 0 \end{bmatrix} & 0_{2\times5} \\ 0_{5\times3} & 0_{5\times2} & 0_5 \end{bmatrix},$$

$$J_i = \begin{bmatrix} J_2 & 0_{2\times8} \\ 0_{8\times2} & J_{1i} \end{bmatrix}$$

$$J_{1i} = \begin{bmatrix} 0_1 & 0_{1\times4} & 0_{2\times3} \\ 0_{3\times2} & \begin{bmatrix} 0 & \frac{1}{2x_{5i}} & 0 & 0 \\ -\frac{1}{2x_{5i}} & 0 & \psi_{qi} & -\psi_{di} \\ 0 & -\psi_{qi} & 0 & 0 \\ 0 & \psi_{di} & 0 & 0 \end{bmatrix} & 0_3 \\ 0_{4\times1} & 0_3 & 0_3 \end{bmatrix},$$

$$r_{3i} = \frac{x_{3i}^2 \left(k_{f2i} + \frac{1}{x_{4i}^2} \right)}{\frac{\partial H_i}{\partial x_{3i}}}, \quad r_{4i} = \frac{x_{4i}}{\frac{\partial H_i}{\partial x_{4i}}}.$$

It is important to mention that the dynamic model of (3.6) does not consider the rotor angle dynamic. The justification is that the next chapter will develop a control scheme for the system (3.6), where the convergence will be guaranteed based on the IDA–PBC method described in Section 4.1. Since this includes the rotor speed, the rotor angle will converge to a constant value and (3.3) can be omitted (Huerta et al., 2018; Fiaz et al., 2012).

3.2 Photovoltaic Power Plant

Photovoltaic power plants are large–scale photovoltaic systems (PV plants) designed to supply electricity into the power systems. They are composed mainly of photovoltaic modules and power electronic converters (Breeze, 2016; Yang et al., 2018b). Power electronic converters are used to interconnect the ac and dc side of a PV plant. Generally, two types of converters are used, dc–dc boost converter for maximum power point tracking (MPPT) and voltage source converter (VSC) for dc–ac conversion (Esram and Chapman, 2007). The MPPT is an algorithm based on the principle of extracting the maximum power available in the panels under different conditions and supplying this to the dc–link (Esram and Chapman, 2007; Ramli et al., 2017). Different models have been used to analyze the dynamics of the VSC in power systems. Commonly, the VSC model is approximated to an average value model ignoring the fast switching of the converters (Chaudhuri et al., 2014; Ortega and Milano, 2016). An average model is used in this dissertation for transient stability studies. We make the following assumption for each PV plant:

Assumption 6 *The PV plants deliver constant power in shorter time intervals (less than* $5s$*) since the solar radiation can be considered constant for transient stability studies (Remon et al., 2017b).*

3.2.1 Dynamic Model of a VSC

Fig. 3.3 shows the typical configuration of a VSC (Ortega and Milano, 2016). This configuration contains a capacitor, a two–level converter and a transformer in the ac side. The dynamic model for the VSC in $\alpha\beta$ reference frame can be achieved by applying Kirchhoff's voltage law at the ac side and Kirchhoff's current law on dc–link voltage side, as follows

$$\begin{aligned} L_t \frac{d}{dt} i_\alpha &= -r_t i_\alpha + m_\alpha v_{dc} - v_\alpha, \\ L_t \frac{d}{dt} i_\beta &= -r_t i_\beta + m_\beta v_{dc} - v_\beta, \\ C \frac{d}{dt} v_{dc} &= i_{dc} - m_\alpha i_\alpha - m_\beta i_\beta, \end{aligned} \tag{3.7}$$

where $i_{\alpha\beta}$ is the output currents of the VSC to the ac grid, $e_{\alpha\beta}$ is the voltage of the ac grid. L_t and r_t are inductance and resistance of the transformer, respectively. $m_{\alpha\beta} \in [-1, 1]$ is the modulation index of the VSC, which is considered as the control input for the power converter. v_{dc} is the dc–link voltage of the VSC and C is its capacitor. i_{dc} represents the current delivered by the photovoltaic modules.

3.2.2 Direct Power Model for VSC

The dynamic model of the VSC described in (3.7) can be transformed in function of the active and reactive powers. The instantaneous active and reactive powers invariant power Clarke

transformation are defined as

$$\begin{aligned} P =& v_\alpha i_\alpha + v_\beta i_\beta, \\ Q =& v_\beta i_\alpha - v_\alpha i_\beta, \end{aligned} \tag{3.8}$$

where P and Q are the instantaneous active and reactive power outputs of the VSC, and their respective derivatives are

$$\begin{aligned} \frac{dP}{dt} =& i_\alpha \frac{v_\alpha}{dt} + v_\alpha \frac{di_\alpha}{dt} + i_\beta \frac{dv_\beta}{dt} + v_\beta \frac{di_\beta}{dt}, \\ \frac{dQ}{dt} =& i_\alpha \frac{v_\beta}{dt} + v_\beta \frac{di_\alpha}{dt} - i_\beta \frac{dv_\alpha}{dt} - v_\alpha \frac{di_\beta}{dt}. \end{aligned} \tag{3.9}$$

Now, defining $v_{\alpha\beta}$ as

$$\begin{aligned} v_\alpha =& V \cos(\omega_b t), \\ v_\beta =& V \sin(\omega_b t), \end{aligned} \tag{3.10}$$

where V is the the magnitude of the grid voltage in $\alpha\beta$ reference frame and ω_b is its the angular frequency.

Now, derivative with respect to time (3.10) helps reach

$$\begin{aligned} \frac{dv_\alpha}{dt} =& -\omega_b V \sin(\omega_b t) = -\omega_b v_\beta, \\ \frac{dv_\beta}{dt} =& \omega_b V \cos(\omega_b t) = \omega_b v_\alpha. \end{aligned} \tag{3.11}$$

Substituting the two first equations of (3.7) and (3.11) in (3.9) is obtained:

$$\begin{aligned} L_t \frac{dP}{dt} =& -r_t P - \omega_b L_t Q + (v_\alpha m_\alpha + v_\beta m_\beta) v_{dc} - V^2, \\ L_t \frac{dQ}{dt} =& \omega_b L_t P - r_t Q + (v_\beta m_\alpha - v_\alpha m_\beta) v_{dc}. \end{aligned}$$

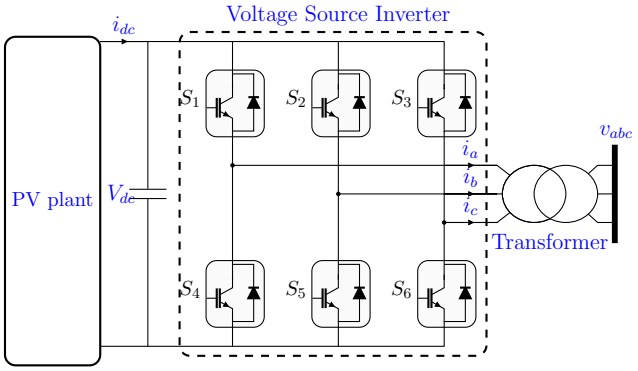

Figure 3.3: Typical interconnection of a VSC for PV plants.

Solving for $i_{\alpha\beta}$ on (3.8) can be obtained

$$\begin{pmatrix} i_\alpha \\ i_\beta \end{pmatrix} = \frac{1}{V^2} \begin{bmatrix} v_\alpha & v_\beta \\ v_\beta & -v_\alpha \end{bmatrix} \begin{pmatrix} P \\ Q \end{pmatrix},$$

now, substituting $i_{\alpha\beta}$ in the third equation of (3.9) obtains

$$V^2 C \frac{dv_{dc}}{dt} = i_{dc} V^2 - (v_\alpha m_\alpha + v_\beta m_\beta) P - (v_\beta m_\alpha - v_\alpha m_\beta) Q.$$

The direct power model (DPC) model for the VSC is

$$\begin{aligned} L_t \frac{dP}{dt} &= - r_t P - \omega_b L_t Q + (v_\alpha m_\alpha + v_\beta m_\beta) v_{dc} - V^2, \\ L_t \frac{dQ}{dt} &= \omega_b L_t P - r_t Q + (v_\beta m_\alpha - v_\alpha m_\beta) v_{dc}, \\ V^2 C \frac{dv_{dc}}{dt} &= i_{dc} V^2 - (v_\alpha m_\alpha + v_\beta m_\beta) P - (v_\beta m_\alpha - v_\alpha m_\beta) Q. \end{aligned} \tag{3.12}$$

It is important to mention that the controller design for the DPC dynamical system described in (3.12) can complicate since this system is a non–autonomous and its control inputs are coupled to control P and Q. To simplify this problem, we use the following orthogonal transformation

$$\begin{bmatrix} m_d \\ m_q \end{bmatrix} = \begin{bmatrix} \cos(\omega_b t) & \sin(\omega_b t) \\ -\sin(\omega_b t) & \cos(\omega_b t) \end{bmatrix} \begin{bmatrix} m_\alpha \\ m_\beta \end{bmatrix}, \tag{3.13}$$

which allows decoupling $u_{\alpha\beta}$ and becomes the DPC model in an autonomous system.

Applying (3.13) in (3.12) yields

$$\begin{aligned} L_t \frac{dP}{dt} &= - r_t P - \omega_b L_t Q + V m_d v_{dc} - V^2, \\ L_t \frac{dQ}{dt} &= \omega_b L_t P - r_t Q - V m_q v_{dc}, \\ V^2 C \frac{dv_{dc}}{dt} &= i_{dc} V^2 - V m_q P + V m_q Q. \end{aligned} \tag{3.14}$$

The control laws can be computed in $\alpha\beta$ reference frame applying (3.13), as follows

$$\begin{bmatrix} m_\alpha \\ m_\beta \end{bmatrix} = \begin{bmatrix} \cos(\omega_b t) & \sin(\omega_b t) \\ -\sin(\omega_b t) & \cos(\omega_b t) \end{bmatrix} \begin{bmatrix} m_d \\ m_q \end{bmatrix}. \tag{3.15}$$

Now, multiply and divide by V in (3.15), and using (3.10), the original control laws are

$$\begin{bmatrix} m_\alpha \\ m_\beta \end{bmatrix} = \frac{1}{V} \begin{bmatrix} v_\alpha & -v_\beta \\ v_\beta & v_\alpha \end{bmatrix} \begin{bmatrix} m_d \\ m_q \end{bmatrix}. \tag{3.16}$$

Remark 5 *Note that this formulation avoids using phase–locked–loop (PLL) to integrate a VSC, which that increases the reliability of the system without time delay while diminishing the investment costs in electronic devices.*

3.2.3 Equivalent port–Hamiltonian Model

The dynamic model of the VSC presented in (3.14) can be represented like a pH system with a stored energy function H_{pv} given by:

$$H_{pv} = \frac{1}{2} x_{pv}^{\top} \mathcal{P} x_{pv},$$

where $x_{pv} = \text{col}(P, Q, V_{dc})$ and $\mathcal{P}_{pv} = \text{diag}\big(L_t, L_t, V^2 C\big)$,

$$\frac{d}{dt} x_{pv} = \left(J_{o_{pv}} + V \sum_{i=1}^{2} J_{i_{pv}} u_{i_{pv}} - R_t \right) x_{pv} + d_{pv}, \tag{3.17}$$

where $u_{pv} = \text{col}(m_d, m_q)$, $d_{pv} = \text{col}(-V^2, 0, V^2 i_{dc})$, $R_t = \text{diag}(r_t, r_t, 0)$, while

$$J_{o_{pv}} = \begin{bmatrix} J_2 \omega_b L_t & 0_{2\times 1} \\ 0_{1\times 2} & 0 \end{bmatrix} J_{1_{pv}} = \begin{bmatrix} 0 & 0 & 1 \\ 0 & 0 & 0 \\ -1 & 0 & 0 \end{bmatrix} \; J_{2_{pv}} = \begin{bmatrix} 0 & 0 & 0 \\ 0 & 0 & -1 \\ 0 & 1 & 0 \end{bmatrix}.$$

3.3 Superconducting Magnetic Energy Storage System

Superconducting magnetic energy storage (SMES) is a system that energy storage in the form of a magnetic field by the dc current in the superconducting coil. The electrical losses caused by Joule effect can be negligible since the superconductor coil is cooled below its superconducting critical temperature (Zobaa, 2013; Grbović, 2013). Most important features of SMES systems are summarized as: Fast dynamic response in charge–discharge states (bidirectional operation), active and reactive power control independently, high energy density and low degradations in each operative cycle, and deep discharge capability (Ali et al., 2010).

Fig. 3.4 illustrates the basic structure of a SMES system connected to the power system through a VSC (Lin and Lei, 2017). The SMES system consists of two converters: a two–level VSC and a dc–dc chopper. These converters are interconnected through of a common dc–link capacitor.

The DPC model for the SMES system is obtained similarly to the DPC model for the PV plants, it is only necessary to add the dynamic of the superconducting coil which is defined as

$$L_s \frac{d}{dt} i_s = -m_s v_{dc}, \tag{3.18}$$

where $m_s \in [-1, 1]$ is the modulation index of the dc–dc chopper and i_s is current delivered (or absorbed) by the superconducting coil.

Now, the dynamic model in DPC for the SMES system is full by using (3.14) and (3.18), as

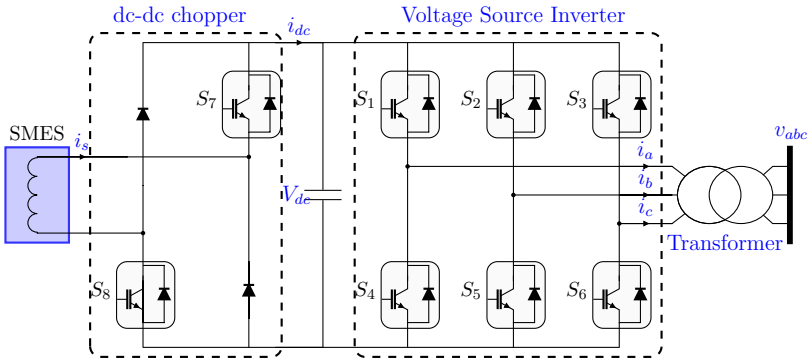

Figure 3.4: Connection of a SMES system with dc-dc chopper.

follows

$$\begin{aligned} L_t\frac{dP}{dt} &= -r_tP - \omega_bL_tQ + Vm_dv_{dc} - V^2, \\ L_t\frac{dQ}{dt} &= \omega_bL_tP - r_tQ - Vm_qv_{dc}, \\ V^2C\frac{dv_{dc}}{dt} &= V^2i_sm_s - Vm_qP + Vm_qQ, \\ V^2L_s\frac{d}{dt}i_s &= -V^2m_sv_{dc}. \end{aligned} \tag{3.19}$$

3.3.1 Equivalent port–Hamiltonian Model

The dynamic model of the SMES system presented in (3.19) can be represented like a pH system with a stored energy function H_{sc} given by:

$$H_{sc} = \frac{1}{2}x_{sc}^\top \mathcal{P} x_{sc},$$

where $x_{sc} = \text{col}(P, Q, V_{dc}, i_s)$ and $\mathcal{P}_{sc} = \text{diag}\big(L_t, L_t, V^2C, V^2L_s\big)$,

$$\frac{d}{dt}x_{sc} = \left(J_{o_{sc}} + V\sum_{i=1}^{3} J_{i_{sc}}u_{i_{sc}} - R_{sc}\right)x_{sc} + d_{sc}, \tag{3.20}$$

where $u_{sc} = \text{col}(m_d, m_q, m_s)$, $d_{sc} = \text{col}(-V^2, 0, 0, 0)$, $R_{sc} = \text{diag}(r_t, r_t, 0, 0)$, while

$$J_{o_{sc}} = \begin{bmatrix} J_2\omega_bL_t & 0_2 \\ 0_2 & 0_2 \end{bmatrix} J_{1_{sc}} = \begin{bmatrix} 0 & 0 & 1 & 0 \\ 0 & 0 & 0 & 0 \\ -1 & 0 & 0 & 0 \\ 0 & 0 & 0 & 0 \end{bmatrix} J_{2_{sc}} = \begin{bmatrix} 0 & 0 & 0 & 0 \\ 0 & 0 & -1 & 0 \\ 0 & 1 & 0 & 0 \\ 0 & 0 & 0 & 0 \end{bmatrix} J_{3_{sc}} = \begin{bmatrix} 0 & 0 & 0 & 0 \\ 0 & 0 & 0 & 0 \\ 0 & 0 & 0 & 1 \\ 0 & 0 & -1 & 0 \end{bmatrix}.$$

3.4 VCS–HVDC System

The VSC–HVDC systems are flexible dc networks that have attracted interest in recent years. They present many advantages such as improving power quality, fast control on the active and reactive power independently, connection to remote generation or feeding of load isolated and facilitating power grid connections, among others (Beerten et al., 2014; Zheng et al., 2015; Liao et al., 2017). These advantages have permitted a growing role in energy transmission systems throughout the world and have shown the potential for large–scale application in power transmission and distribution systems (Haruni et al., 2013; Yang et al., 2018a).

A two–terminal VSC–HVDC system portrayed in Fig. 3.5 is interfaced to the ac network through the transformer. The ac network consists of an ac voltage source and two transmission lines in parallel, which are also connected to the transformer. This point of interconnection is known as the point of common coupling (PCC). The DPC model for the VSC–HVDC system is obtained similarly to the DPC model for the PV plants described in Section 3.2, it is only necessary to add the dynamic of the dc transmission line which is expressed by

$$L_{dc}\frac{d}{dt}i_{dc} = -r_{dc}i_{dc} + v_{dc1} - v_{dc2}, \tag{3.21}$$

where r_{dc} and L_{dc} are the resistive and inductive effects of the dc–cable.

Now, the dynamic model in DPC model for the VSC–HVDC system is full by using (3.14) and (3.21), as follows

$$\begin{aligned}
L_t\frac{dP_1}{dt} &= -r_tP_1 - \omega_1 L_tQ_1 - Vv_{dc1}m_{d1} + V^2,\\
L_t\frac{dQ_1}{dt} &= \omega_1 L_tP_1 - r_tQ_1 + Vv_{dc1}m_{q1}\\
V^2C\frac{dv_{dc1}}{dt} &= -V^2i_{dc} + VP_1m_{d1} - VQ_1m_{q1}\\
L_t\frac{dP_2}{dt} &= -r_tP_2 - \omega_2 L_tQ_2 + Vv_{dc2}m_{d2} - V^2,\\
L_t\frac{dQ_2}{dt} &= \omega_2 L_tP_2 - r_tQ_2 - Vv_{dc2}m_{q2}\\
V^2C\frac{dv_{dc2}}{dt} &= V^2i_{dc} - VP_2m_{d2} + VQ_2m_{q2},
\end{aligned} \tag{3.22}$$

where ω_1 and ω_2 are angular frequency of ac network 1 and 2, respectively.

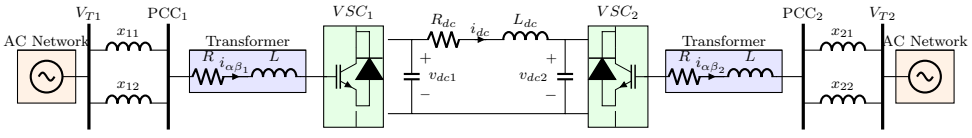

Figure 3.5: Configuration of a two–terminal VSC–HVDC system.

It is important to point out that the instantaneous power for the VSC_1 is the input while for the VSC_2 is the output.

3.4.1 Equivalent port–Hamiltonian Model

The dynamic model of the two–terminal VSC–HVDC system presented in (3.22) can be represented like a pH system with a stored energy function H_{hv} given by:

$$H_{hv} = \frac{1}{2} x_{hv}^{\top} \mathcal{P}_{hv} x_{hv},$$

and its dynamic is

$$\mathcal{P}_{hv} \dot{x}_{hv} = \left(J_{hv_o} + \sum_{i=1}^{4} J_{hv_i} u_{hv_i} - R_{hv} \right) x_{hv} + d_{hv}, \tag{3.23}$$

where $J_{hvo_{12}} = -L\omega_1$, $J_{hvo_{76}} = -L\omega_2$, $J_{hvo_{43}} = J_{hvo_{54}} = V^2$, $J_{hv1_{13}} = -V$, $J_{hv2_{23}} = V$, $J_{hv3_{65}} = -V$, $J_{hv4_{75}} = V$, while

$$\begin{aligned}
x_{hv} =& \text{col}(P_1, Q_1, v_{dc1}, i_{dc}, v_{dc2}, Q_2, P_2),\\
u_{hv} =& \text{col}(m_{d1}, m_{q1}, m_{d2}, m_{q2}),\\
d_{hv} =& \text{col}(V^2, 0, 0, 0, 0, 0, -V^2),\\
\mathcal{P}_{hv} =& \text{diag}\big(L_t, L_t, V^2 C, V^2 L_{dc}, V^2 C, L_t, L_t\big)\\
R_{hv} =& \text{diag}\big(r_t, r_t, 0, V^2 r_{dc}, 0, r_t, r_t\big),
\end{aligned}$$

3.5 Electrical Network Model

A modern power system may include n generators, m transmission lines, t transformers, renewable sources n_r, energy storage systems l and k loads as shown in Fig. 1.1. Here, each HTGS (hydro power plant) is modeled by (3.6) and each thermal power plant and their governors are modeled by IEEEG1 steam turbine model (Pourbeik et al., 2013). Their mechanical and electrical models are represented by (3.2) and (3.3). The PV plants, SMES systems, and VSC–HVDC systems are modeled by (3.17), (3.20), and (3.23), respectively. Each transmission line and transformer can be modeled by the π–equivalent circuits (Machowski et al., 2008). Here, loads, transformers, and transmission lines are represented by the standard phasor representation neglecting their dynamics as these are significantly faster than the mechanical dynamics of each generator (Machowski et al., 2008; Loukianov et al., 2009). In addition, considering the loads as constant impedances, the electrical network model can be reduced by using Kron's reduction, as follows

$$\mathbf{I} = \mathbf{Y}(\delta_1, ..., \delta_n)\mathbf{V}, \;\; \mathbf{Y}(\cdot) \in \mathcal{R}^{2n \times 2n}$$

where $\mathbf{Y}(\cdot)$ is the reduced admittance matrix in the terminal nodes of the synchronous machines, the PV systems or the SMES systems, $\mathbf{I} = \text{col}(i_{d1}, i_{q1}, ..., i_{dn}, i_{qn})$ and $\mathbf{V} = \text{col}(v_{d1}, v_{q1}, ..., v_{dn}, v_{qn})$ represent the vectors of the currents (i_{di} and i_{qi}) and voltages (v_{di} and v_{qi}), respectively. See (Machowski et al., 2008, Cap. 3) for more details.

3.6 Summary of the Chapter

This chapter showed the mathematical model for the component of power system such as hydro–turbine governing system, synchronous machines as well as photovoltaic solar plants, superconducting coil energy storage, VSC–HVDC system, and the electrical network. In addition each model was condensed into a pH structure.

Chapter 4

Power System Control

This chapter presents the control design for each component of the power system described in Chapter 3. Each control design is based on the PBC theory presented in Chapter 2. Additionally, it describes the proposed methodology of the power oscillation damper for the PV plants and the SMES system. This Chapter is developed under the following assumptions:

Assumption 7 *The nominal parameters of HTGSs, the PV plants, and the SMES systems are known.*

Assumption 8 *All the states are available for measurement.*

4.1 Controller Design for the HTGS

The control aims for each HTGS are to stabilize the rotor speed and regulate the generator terminal voltage to improve power system stability under small and large disturbances. The control design is based on the IDA–PBC presented in Section 2.5.1. To apply this method, it is necessary to establish the desired total stored $H(\tilde{x}_i)_{di}$, the desired interconnection matrix J_{di}, and the desired damping matrix R_{di}. We select $H(\tilde{x}_i)_d$ as the quadratic function:

$$H(\tilde{x}_i)_{di} = \frac{1}{2}(x_i - x_i^*)^T \mathcal{P}_i (x_i - x_i^*),$$

where x_i^* is desired assignable equilibrium point for each i–HTGS of the power system, also known as the steady–state vector and its the derivative can be calculated as

$$\frac{\partial H(\tilde{x}_i)_{di}}{\partial x_i} = \begin{bmatrix} x_{1i} - x_{1i}^* \\ x_{2i} - x_{2i}^* \\ x_{3i} - x_{3i}^* \\ x_{4i} - x_{4i}^* \\ x_{5i} - x_{5i}^* \\ x_{6i} - x_{6i}^* \\ x_{7i} - x_{7i}^* \\ x_{8i} - x_{8i}^* \\ x_{9i} - x_{9i}^* \\ x_{10i} - x_{10i}^* \end{bmatrix} = \begin{bmatrix} q_{1i} - q_{1i}^* \\ h_{si} - h_{si}^* \\ q_{2i} - q_{2i}^* \\ y_i - y_i^* \\ \omega_i - \omega_b \\ i_i - i_i^* \end{bmatrix}.$$

Remark 6 *The desired total stored $H(\tilde{x}_i)_{di}$ is a quadratic positive definite function, which meets the first two Lyapunov stability conditions presented in (2.2). In addition, its minimum $x_i = x_i^*$ fulfills*

$$\frac{\partial H(\tilde{x}_i)_{di}}{\partial \tilde{x}_i} \mid_{x_i = x_i^*} = 0$$
$$\frac{\partial^2 H(\tilde{x}_i)_{di}}{\partial \tilde{x}_i^2} = \mathcal{P}_i \mid_{x_i = x_i^*} > 0,$$

therefore, x_i^* will be a stable equilibrium point of the closed–loop system.

Now, we define the matrices R_{di} and J_{di} as having a relation between the control aims and control variables, as follows:

$$R_{di} = \text{diag}(r_{1i}, ..., r_{10i}),$$
$$J_{di} = \begin{bmatrix} 0_2 & 0_{2\times 3} & 0_{2\times 5} \\ 0_{3\times 2} & \begin{bmatrix} 0 & 0 & k_{2i} \\ 0 & 0 & k_{1i} \\ -k_{2i} & -k_{1i} & 0 \end{bmatrix} & 0_{3\times 5} \\ 0_{5\times 2} & 0_{5\times 3} & 0_5 \end{bmatrix},$$

where $r_{ji} > 0 \; \forall \; j = 1, ..., 10$, $k_{1i} \neq 0$, and $k_{2i} \neq 0$.

If (2.16) is used, the control laws are:

$$\begin{aligned} u_{yi} &= x_{4i} - k_{1i}(x_{5i} - x_{5i}^*) - r_{4i}(x_{4i} - x_{4i}^*), \\ v_{fi} &= r_{fi} x_{8i} - r_{8i}(x_{8i} - x_{8i}^*). \end{aligned} \tag{4.1}$$

The governing system typically regulates the rotor speed and manages the electrical power generated by synchronous machine by changing gate position. For this reason, the x_{3i}^* and x_{5i}^* are

chosen to fulfill these aims. By defining an admissible equilibrium point from (3.1), it is possible to compute:

$$\begin{aligned} x_{1i}^* =& x_{3i}^*, \\ x_{2i}^* =& 1 - k_{f1i}\left(x_{3i}^*\right)^2, \\ x_{4i}^* =& \frac{x_{3i}^*}{\sqrt{1-\left(x_{3i}^*\right)^2\left(k_{f1i}+k_{f2i}\right)}}, \\ 0 =& \left(k_{f1i}+k_{f2i}\right)\left(x_{3i}^*\right)^3 - q_{nli}(k_{f1i}+k_{f2i})\left(x_{3i}^*\right)^2 - x_{3i}^* + \left(\frac{P_{mi}^*}{A_{ti}} + q_{nli}\right), \end{aligned} \tag{4.2}$$

where P_{mi}^* is the desired mechanical power delivered by machine i, which can write in term of P_i^* is the electrical power delivered, as follows,

$$P_{mi}^* = P_i^* + ||i_{dqi}||^2 r_{si}.$$

Note that fourth equation of (4.2) has three solutions, but, only one of them satisfies Assumption 4 and to solve for this polynomial online may complicate the controller. For this reason, we propose to compute x_{3i}^* with the following approximation

$$x_{3i}^* \approx \frac{P_{mi}^*}{A_{ti}} + q_{nli} + q_{nli}\left(k_{f1i}+k_{f2i}\right)\left(4P_{mi}^* + \frac{1}{2}\right)\left(P_{mi}^*\right)^2. \tag{4.3}$$

Fig. 4.1 illustrates the error of x_{3i}^* is computed as the difference between (4.2) and (4.3).
The reference rotor speed x_{5i}^* is defined as

$$x_{5i}^* = \omega_b.$$

The field current controls the voltage magnitude of the generator terminal, which in the dq reference frame is defined as:

$$v_{ti}^2 = v_{di}^2 + v_{qi}^2. \tag{4.4}$$

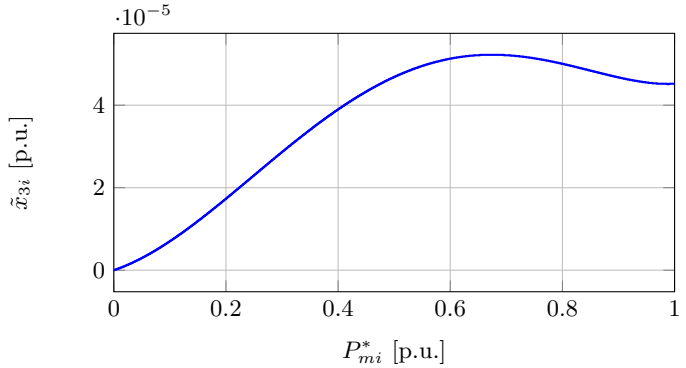

Figure 4.1: Error of approximation for the $\tilde{x}_{3i}$.

Now, using (3.5) and (4.4) at an equilibrium point, it is possible to obtain x_{8i}^* to control the terminal voltage magnitude, as

$$x_{8i}^* = \frac{v_{qi}^* + r_{si}x_{7i}^* + L_{di}x_{5i}^*x_{6i}^*}{L_{mdi}x_{5i}^*}. \tag{4.5}$$

with

$$v_{qi}^* = \sqrt{v_{ti}^{2\,*} - v_{di}^{*\,2}},$$

where v_{di}^* is determined by

$$v_{di}^* = v_{ti}^* \sin(\delta_i),$$

To apply the control laws of (4.1), it is necessary to compute the non–controlled variables that can be found by defining the left annihilator of g_i as

$$g_i^\perp = \begin{bmatrix} 0_{3\times 4} & 1_3 & 0_3 \end{bmatrix}^T,$$

and using (2.10), the non–controlled variables are:

$$\begin{aligned} x_{4i}^* =& \frac{b_i x_{5i}^* - \tau_{mi} + \tau_{ei} + k_{1i}x_{4i} - r_{5i}(x_{5i} - x_{5i}^*) + k_{2i}(x_{3i} - x_{3i}^*)}{k_{1i}}, \\ x_{6i}^* =& \frac{-v_{di} + \psi_{qi}x_{5i}^* + (r_{6i} + r_{si})x_{6i}}{r_{6i}}, \\ x_{7i}^* =& \frac{-v_{qi} + \psi_{di}x_{5i}^* + (r_{7i} + r_{si})x_{7i}}{r_{7i}}. \end{aligned} \tag{4.6}$$

Remark 7 *The proposed control for the HTGS has main advantage that is decentralized, thus avoiding all problems of communication among the generators.*

4.1.1 Adaptive IDA–PBC

In this subsection, we assume that some parameters are unknown such as A_{ti}, k_{f1i}, k_{f2i}, and r_f. It is important to highlight that consistent estimates are required to carry out the stability analysis (Hernandez-Gomez et al., 2010). For this reason, we use the Immersion and Invariance (I&I) methodology developed in (Astolfi et al., 2007) to estimate those parameter since an asymptotically stable is ensured. Define the parameter error

$$\tilde{\theta} = \hat{\theta} - \theta, \tag{4.7}$$

where $\tilde{\theta}$ is estimation error, θ is the parameter to estimate, and $\hat{\theta}$ is an estimate of θ, is given by

$$\hat{\theta} = \gamma\xi + \lambda\beta(\chi) \tag{4.8}$$

where $\gamma,\ \lambda > 0$, and ξ and $\beta(\chi)$ are to be designed. χ represents any state of system, which can be written as

$$\chi = e_k^T x, \tag{4.9}$$

where $e_k \in \mathcal{R}^n$ is the kth vector of the standard n–dimensional Euclidean basis. Any dynamic system can be written as

$$\dot{x} = f(x,u) = f'(x,u) + \theta e_k \chi. \tag{4.10}$$

It is important to mention that the parameter θ is not identifiable if $\chi = 0$. Therefore, a reasonable consideration is that[1]

$$\chi^* = e_k^T x^* \neq 0.$$

Differentiating $\tilde{\theta}$ with respect to time gets

$$\begin{aligned}
\dot{\tilde{\theta}} &= \dot{\hat{\theta}} \\
\dot{\tilde{\theta}} &= \gamma\dot{\xi} + \lambda\beta'(\chi)\dot{\chi} \\
\dot{\tilde{\theta}} &= \gamma\dot{\xi} + \lambda\beta'(\chi)e_k^T\dot{x} \\
\dot{\tilde{\theta}} &= \gamma\dot{\xi} + \lambda\beta'(\chi)\left[e_k^T f'(x,u) + \theta e_k^T e_k \chi\right] \\
\dot{\tilde{\theta}} &= \gamma\dot{\xi} + \lambda\beta'(\chi)\left\{e_k^T f'(x,u) + \chi\left[\gamma\xi + \lambda\beta(\chi) - \tilde{\theta}\right]\right\}
\end{aligned} \tag{4.11}$$

where $\beta'(\cdot)$ denotes differentiation of $\beta(\cdot)$ with respect to its argument; (4.8), (4.9), (4.10), (4.7) have been employed in the second, third, fourth, and fifth lines, respectively. Now, selecting

$$\dot{\xi} = -\frac{\lambda}{\gamma}\beta'(\chi)\left\{e_k^T f'(x,u) + \chi\left[\gamma\xi + \lambda\beta(\chi)\right]\right\}. \tag{4.12}$$

Replacing (4.12) in (4.11) yields

$$\dot{\tilde{\theta}} = -\lambda\beta'(\chi)\chi\tilde{\theta},$$

The design of estimator is completed when a suitable function $\beta(\chi)$ that guarantees stability of the dynamics $\tilde{\theta}$ is selected. Hence, we choose

$$\beta(\chi) = \frac{1}{2}\chi^2 \Rightarrow \dot{\tilde{\theta}} = -\lambda\chi^2\tilde{\theta},$$

for any condition initial of the system and all $\theta(0)$ the asymptotic convergence is ensured

$$\tilde{\theta}(t) = \tilde{\theta}(0)e^{-\gamma\chi^2 t}.$$

By applying I&I method the estimates of the unknown parameters are.

[1] See (Astolfi et al., 2007), for more details.

- For $\hat{A}_{ti}$

$$\dot{\xi} = -\frac{\lambda}{\gamma} x_{5i} \left\{ -\tau_{ei} - b_i x_{5i} + \left(\lambda \frac{1}{2} x_{5i}^2 + \gamma \xi \right) \frac{x_{3i}^2 (x_{3i} - q_{nli})}{x_{4i}^2 x_{5i}} \right\}, \tag{4.13}$$
$$\hat{\theta} = \gamma \xi + \frac{1}{2} x_{5i}^2.$$

- For $\hat{k}_{f1i}$

$$\dot{\xi} = -\frac{\lambda}{\gamma} \frac{x_{1i}}{T_{W1}} \left\{ 1 - x_{2i} - \left(\lambda \frac{1}{2} x_{1i}^2 + \gamma \xi \right) x_{1i}^2 \right\}, \tag{4.14}$$
$$\hat{\theta} = \gamma \xi + \frac{1}{2} x_{1i}^2.$$

- For $\hat{k}_{f2i}$

$$\dot{\xi} = -\frac{\lambda}{\gamma} \frac{x_{3i}}{T_{W2}} \left\{ x_{2i} - \frac{x_{3i}^2}{x_{4i}^2} - \left(\lambda \frac{1}{2} x_{3i}^2 + \gamma \xi \right) x_{3i}^2 \right\}, \tag{4.15}$$
$$\hat{\theta} = \gamma \xi + \frac{1}{2} x_{3i}^2.$$

- For $\hat{r}_{fi}$

$$\dot{\xi} = -\frac{\lambda}{\gamma} x_{8i} \left\{ \frac{L_{mdi}}{L_{di}} \left(-r_{si} x_{6i} - L_{mdi} x_{5i} x_{7i} + v_{di} \right) - v_{fi} - \left(\lambda \frac{1}{2} x_{8i}^2 + \gamma \xi \right) \frac{x_{8i}}{L_{fi}} \right\}, \tag{4.16}$$
$$\hat{\theta} = \gamma \xi + \frac{1}{2} x_{8i}^2.$$

Fig. 4.2 illustrates the proposed decentralized control for HTGS based on the IDA–PBC.

4.2 Controller Design for the PV Plants

The control aims for each PV plant are to deliver all the available power of photovoltaic modules and regulate the dc–link voltage to guarantee an operating adequate of the VSC. The control design is based on the PI–PBC described in Section 2.5.2.

If (2.19) is employed, the output function $\tilde{y}_{pvj}$ for each j-PV plant (see (3.17)) becomes:

$$\tilde{y}_{pvj} = V \begin{bmatrix} P_{pvj} v_{dc_{pvj}}^* - P_{pvj}^* v_{dc_{pvj}} \\ Q_{pvj}^* v_{dc_{pvj}} - Q_{pvj} v_{dc_{pvj}}^* \end{bmatrix}. \tag{4.17}$$

where P_{pvj} and Q_{pvj} are the active and reactive output of the j-PV plant, and $v_{dc_{pvj}}$ is its dc–link voltage.

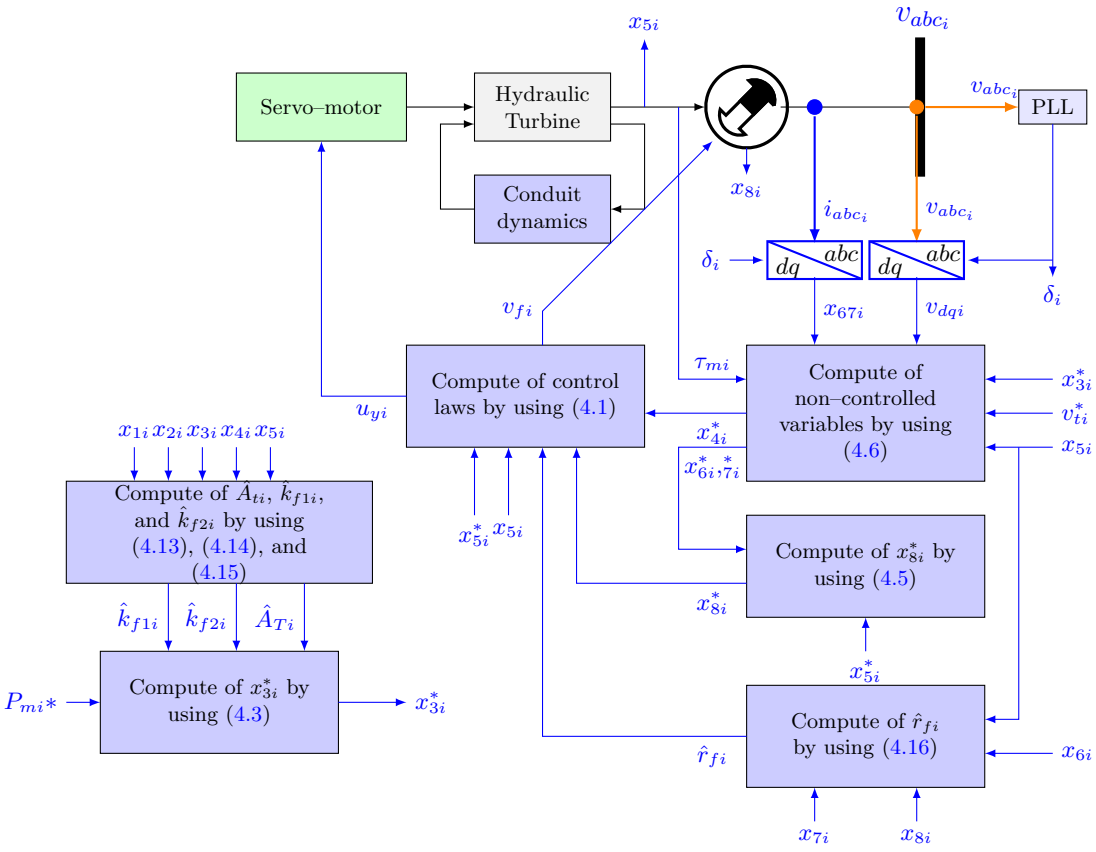

Figure 4.2: The control scheme for HTGS.

The control variables for each PV plant are $v^*_{dc_{pvj}}$ and Q^*_{pvj}. $v^*_{dc_{pvj}}$ is the nominal dc–link of the VSC, i.e., $v^*_{dc_{pvj}} = v^{nom}_{dc}$, and Q^*_{pvj} is its reference value for the reactive power.

Now, the control design is complete when a desired operating point for each PV plant system has already been chosen to know P^*_{pvj}. Even though it is assumed that the equilibrium point is known by steady–state analysis of power flow, the dynamic response will be extremely slow as demonstrated in (Zonetti et al., 2015). This problem has been solved in (Bergna-Diaz et al., 2018) for a multi–terminal HVDC system based on modular multilevel converters a multi–terminal, including a conventional outer–loop control generated by a simple PI controller acting. Therefore, we adopted this strategy to determinate desired operating point of P^*_{pvj}, introducing a simple PI controller acting on the error signal between $v^*_{dc_{pvj}}$ and $v_{dc_{pvj}}$, as follows

$$P^*_{pvj} = P^\star_{pvj} - Kp_{pvj}(v^*_{dc_{pvj}} - v_{dc_{pvj}}) - Ki_{pvj}\int (v^*_{dc_{pvj}} - v_{dc_{pvj}})dt, \tag{4.18}$$

with

$$P^{\star}_{pvj} = v^{*}_{dc_{pvj}} i_{dc_{pvj}}.$$

It is important the mention that the stability proof shown in Section 2.5.3 may be compromised by replacing (4.18) into (4.17), which is only valid when P^{*}_{pvj} is constant at the equilibrium point. We invoke the time–scale separation assumption proposed in (Bergna-Diaz et al., 2018) and (Zonetti, 2016) among the outer–loops and the inner PI–PBC, which possesses the interesting property to treat with the potential lost stability, by tuning only the outer–loop parameters. Fig. 4.3 depicts the DPC scheme based on PI–PBC for each PV plant.

Remark 8 *In (Bergna-Diaz et al., 2018) only includes a conventional outer–loop control of computing the equilibrium point of non–controlled variables which indicates that the proof stability depends exclusively on tuning only the outer–loop parameters. However, we add a term as $P^{\star}_{pvj}$ which permits guaranteeing that the time–scale separation assumption is adequate.*

Remark 9 *Observe that the controller is robust under parametric uncertainty and unmodeled dynamics since it does not depend on them*

4.2.1 Methodology of the Power Oscillation Damper

The proposed methodology for improving power oscillation damper (POD) in a power system with a high–level of PV penetration is based on a washout–filter and gain with a single input signal, which is shown in Fig. 4.4 (Surinkaew and Ngamroo, 2017, 2019). The compensator parameters consists of a gain K_f, a washout time constant (T_W), and a low–filter time constant (s) T_r. The input signal is the frequency deviation ($\Delta f = f - f^{*}$). The output compensator, denoted by v_s, is added at the summing junction at the $v^{nom}_{dc_{pvj}} t$ as shown in Fig. 4.4. Observe that K_f represents the frequency droop contribution of each PV plant, which can be computed:

$$K_f = \frac{1}{R_f},$$

where R_f is referred to as the constant regulation (Machowski et al., 2008; Anderson and Fouad, 2003).

On the other hand, the proposed methodology also takes into account the limitation of the transference of the active and reactive power of VSC. Fig. 4.5 portrays the case where the active power has priority over the reactive power. This priority is selected because the objective of this dissertation is to reduce POD. This strategy limits P^{*}_{pvj} to the maximum power capacity $\pm S^{max}_{pvj}$ and limits Q^{*}_{pvj} up to not exceed the maximum power rating, as follows,

$$P^{lim}_{pvj} \leq S^{max}_{pvj},$$
$$-\sqrt{S^{max\,2}_{pvj} - P^{lim\,2}_{pvj}} \leq Q^{lim}_{pvj} \leq \sqrt{S^{max\,2}_{pvj} - P^{lim\,2}_{pvj}},$$

where S^{max}_{pvj} is maximum power that can support the PV plant (or VSC).

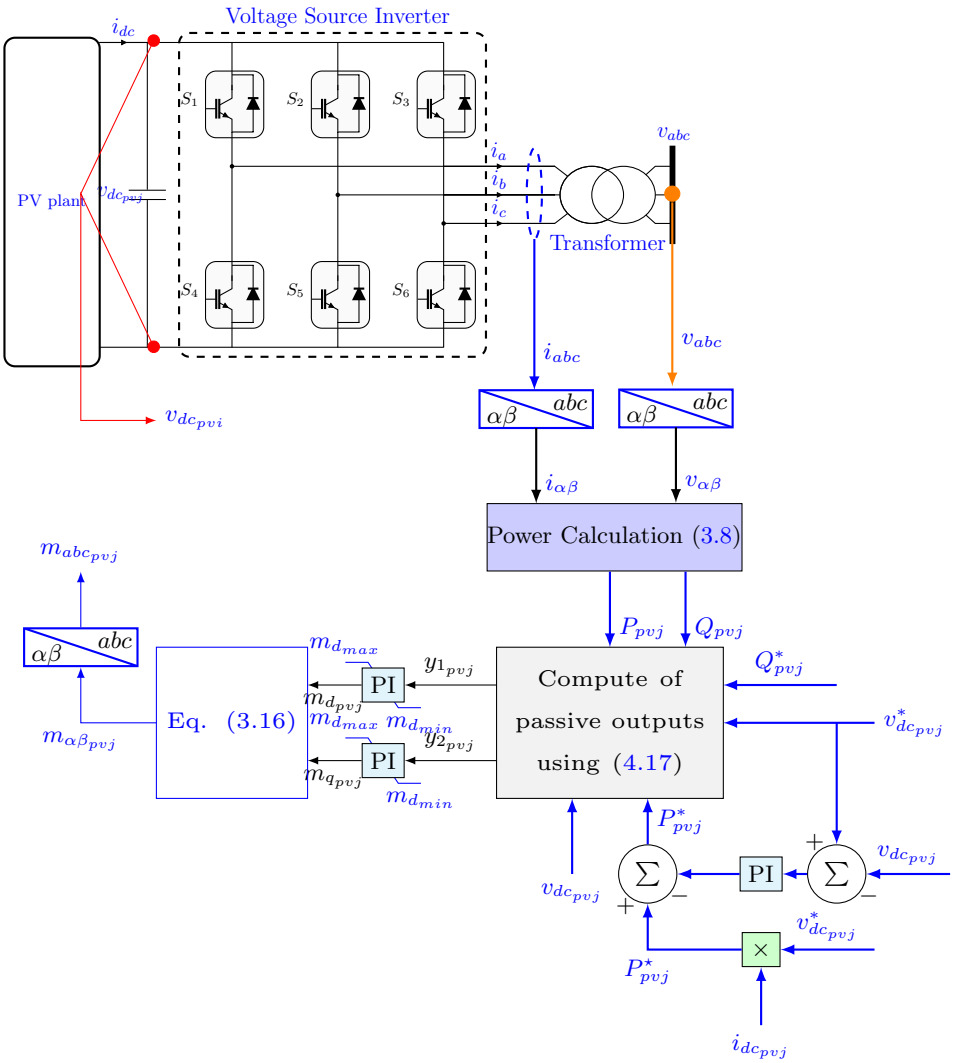

Figure 4.3: The DPC scheme based on PI–PBC for each PV plant.

4.3 Controller Design for the SMES System

The control aims for the SMES system are to control the active and reactive power delivered (or absorbed) by it and regulate the dc–link voltage. The control design is based on the PI–PBC described in Section 2.5.2.

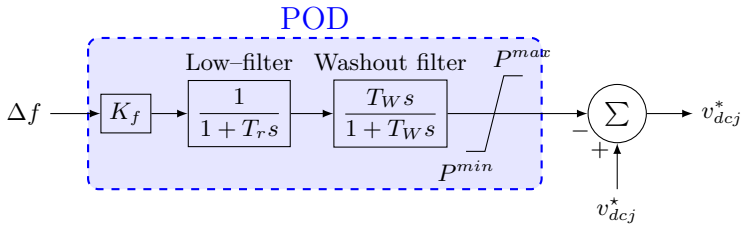

Figure 4.4: POD in dc–link voltage loop.

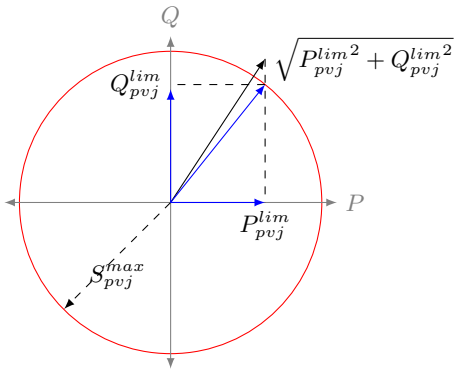

Figure 4.5: Power limiting strategy priority given to P^{lim}_{pvj}.

If (2.19) is used, the output function $\tilde{y}_{scj}$ for each j–SMES system (see (3.20)) becomes:

$$\tilde{y}_{scj} = V \begin{bmatrix} P_{scj} v^*_{dc_{scj}} - P^*_{scj} v_{dc_{scj}} \\ Q^*_{scj} v_{dc_{scj}} - Q_{scj} v^*_{dc_{scj}} \\ V\left(i^*_{sj} v_{dc_{scj}} - i_{sj} v^*_{dc_{scj}}\right) \end{bmatrix}. \tag{4.19}$$

where P_{scj} and Q_{scj} are the active and reactive output of the j–SMES system, $v_{dc_{scj}}$ is its dc–link voltage and $i_{s_{scj}}$ is the current of the superconducting coil.

The control variables for the SMES system are $v^*_{dc_{scj}}$, P^*_{scj}, and Q^*_{scj}. $v^*_{dc_{scj}}$ is the nominal dc–link of the VSC, i.e., $v^*_{sc_{pvj}} = v^{nom}_{dc}$, and Q^*_{scj} and Q^*_{scj} are the desired reference values for the active and reactive power, respectively.

Now, the control design is fulfilled when a desired operating point for j–SMES system has already been selected to know i^*_{sj}. Here we have a similar problem as presented for the photovoltaic plant. Assuming the same the time–scale separation assumption, the operating point of i^*_{sj} is determined by

$$i^*_{sj} = i^\star_{dcj} - Kp_{scj}(v^*_{dc_{scj}} - v_{dc_{scj}}) - Ki_{scj} \int (v^*_{dc_{scj}} - v_{dc_{scj}})dt,$$

$$i^{\star}_{dcj} = \frac{P^{*}_{scj}}{v^{*}_{dc_{scj}}},$$

lastly, in Fig. 4.6 is depicted its control scheme based on PI–PBC.

4.3.1 Methodology for the Improvement of Power Oscillations Damping

In this part, it is described the proposed methodology to compute the active and reactive power references for the improvement of power oscillations in a power system. The proposed methodology

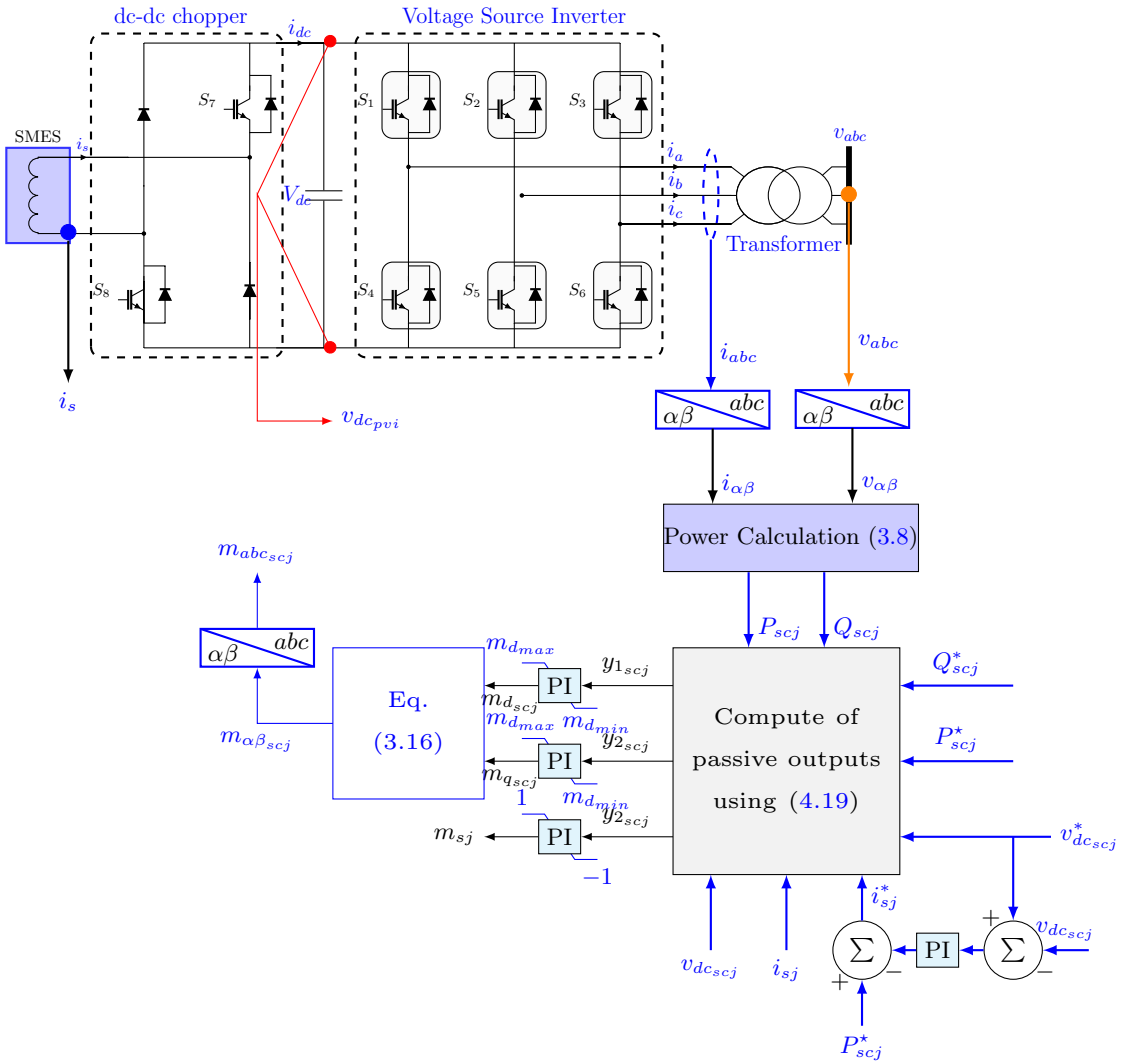

Figure 4.6: The DPC scheme based on PI–PBC for SMES system.

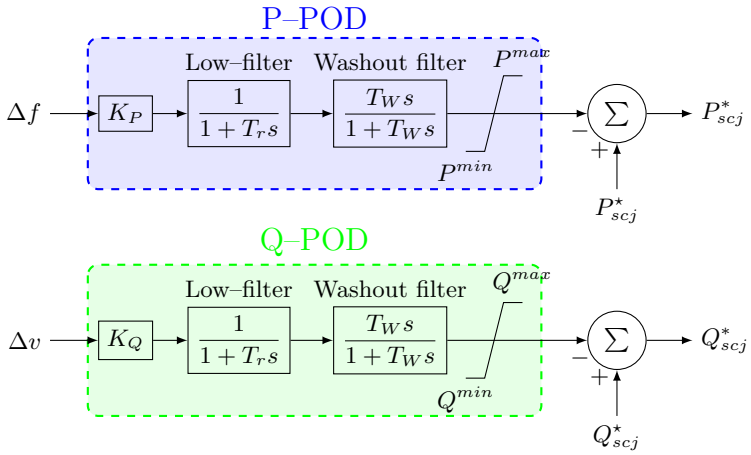

Figure 4.7: The structure of POD for the active and reactive power.

is the same used for the PV plants, which is illustrated in Fig. 4.7. The input signals of the POD for the active (P–POD) and reactive (Q–POD) power are the frequency deviation (Δf) and the voltage deviation ($\Delta v = v - v^*$), respectively. The output signals of the P–POD and Q–POD are sent to the desired active and reactive reference power as shown Fig. 4.7, respectively. These output signals are limited by their maximum and minimum values. The compensator P–POD parameters consists of a gain K_P, a washout time constant (T_W), and a low–filter time constant (s) T_r, and similarly the compesador Q–POD parameters can be defined. The SMES system also takes into account the limitation of the transference of the active and reactive power of VSC as described in Section 4.2.1.

4.4 Controller Design for the VSC–HVDC System

The design of the PI–PBC for the VSC–HVDC system is described in this part.

If we use (2.19), the output function $\tilde{y}_{hv}$ for the VSC–HVDC system is

$$\tilde{y}_{hv} = V \begin{bmatrix} P_1^* v_{dc1} - P_1 v_{dc1}^* \\ Q_1 v_{dc1}^* - Q_1^* v_{dc1} \\ P_2 v_{dc2}^* - P_2^* v_{dc2} \\ Q_2^* v_{dc2} - Q_2 v_{dc1}^* \end{bmatrix}. \tag{4.20}$$

Remark 10 *The proposed control for the VSC–HVDC system has main advantage that is decentralized, thus avoiding all problems of communication among the VSCs (Zonetti et al., 2015).*

It is necessary to define an VSC as a master controller to choose the control variables. Selecting the VSC_2 as the master controller, its control variables are v_{dc2}^* and Q_2^*, while P_1^* and Q_1^* are the control variables for VSC_1. v_{dc2}^* is the nominal dc–link of the VSC_2, i.e., $v_{dc2}^* = v_{dc}^{nom}$, and Q_2^* is its

reference value for the reactive power. P_1^* and Q_1^* are the reference values of the active and reactive power delivered (or absorbed) by the VSC_1.

Now, the control scheme is complete when the operating point are computed, as follows

$$v_{dc1}^* = -Kp_p(P_1^* - P_1) - Ki_p \int (P_1^* - P_1)dt,$$
$$P_2^* = -Kp_v(v_{dc2}^* - v_{dc2}) - Ki_v \int (v_{dc2}^* - v_{dc2})dt.$$

In Fig. 4.8 is depicted the control schemes for the PI–PBC controller applied to a two–terminal VSC–HVDC system.

4.5 General Comments

The DPC model used for the PV plants, SMES system and VSC–HVDC system has some advantages of avoiding the implementation of the PLL compared with conventional controller based on the current decoupling, which are:

- Less states are needed since the conventional PLL requires two integrators (Golestan et al., 2017), while the DPC model does not need it.
- Lees products are made since the conventional PLL requires three multipliers (Golestan et al., 2017), while the DPC model needs two multipliers. This implies that there is a reduction of 33.33% in the number of products required.
- They are avoided the tuning problems the PLL which is not a trivial task, especially when taking into consideration power-quality phenomena (Freijedo et al., 2009). In addition, they are also avoided the problems when appears the second harmonic in the PLL which may generate in a loss of performance (Freijedo et al., 2009).

4.6 Summary of the Chapter

This chapter presented the control design for HTGS based on the IDA–PBC method. In addition, the estimation of some parameters by applying I&I method were also described. The control design for PV plants, SMES system, and VSC–HVDC system based on PI–PBC were also shown. Additionally, the proposed methodologies for enhancing the power oscillation damper using the PV plants and the SMES system were described.

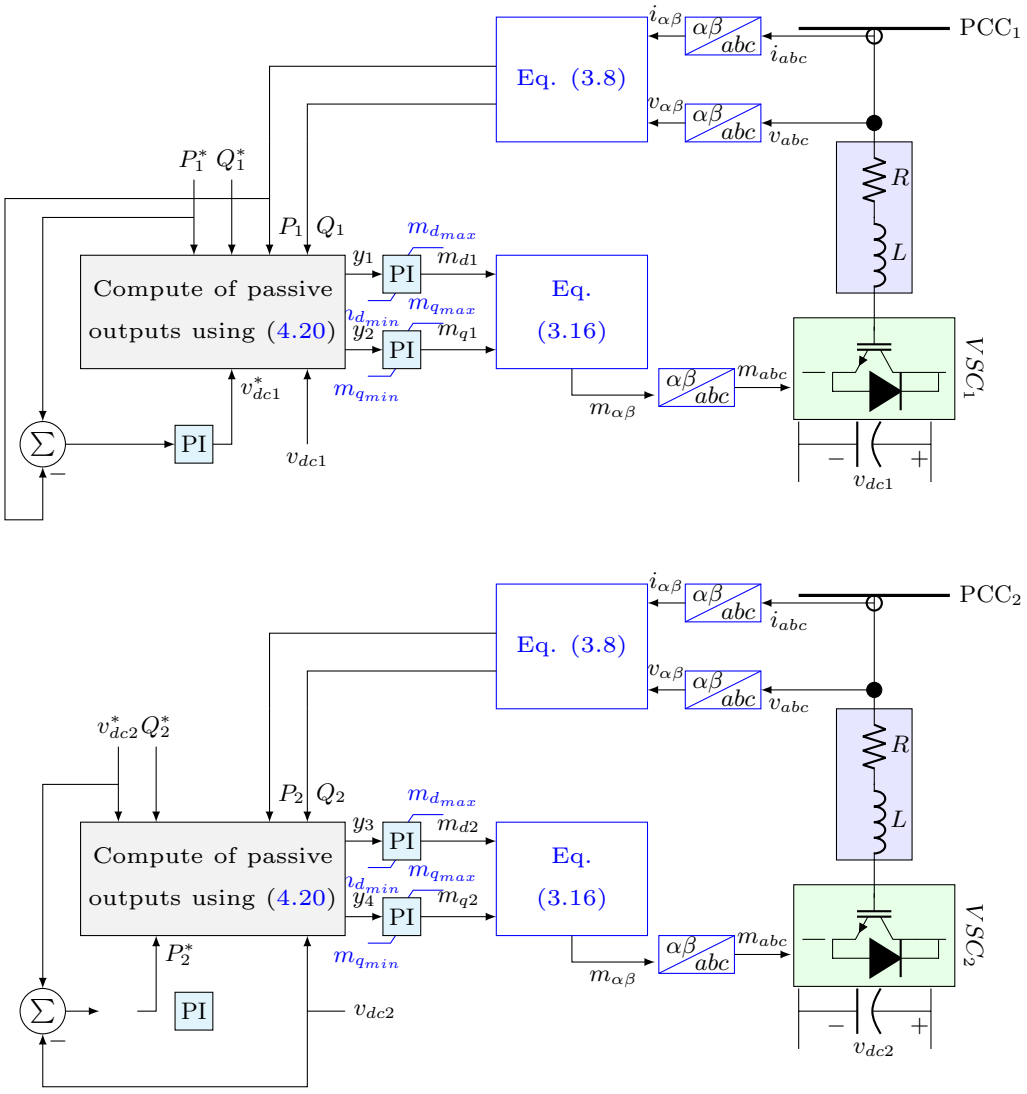

Figure 4.8: Control diagram of the PI–PBC.

Chapter 5

Test System, Simulation and Results

This chapter evaluates the performance of the proposed passivity–based control, for the stabilization of power systems with integration of solar and hydro–thermal units. Each controller described in Chapter 4 is assessed in order to validate its contribution to enhance the dynamic response of the test system. Lastly, all the controllers are evaluated together in the test system.

5.1 Test System

Fig. 5.1 illustrates the 12–bus test system which is used to verify the performance and robustness controller described in Chapter 4 for maintaining the stability of a power system under large disturbances. The test system was proposed in (Adamczyk et al., 2013) and is composed of synchronous generators, eight transmission lines, six two-winding transformers, six loads, two capacitors for compensation and one reactor. The component data are shown in Appendix B. We considered that generators G1, G3, and G4 are hydro–turbines, while generator G2 is a steam–turbine. The excitation control law given by (4.1) was employed in the steam–turbine without making any changes. For comparison, each generator was equipped with IEEE–ST1A excitation systems, power system stabilizer (PSS) IEEE–PSS1A, and turbine governors. The governing systems with static and transient droop to control the hydraulic turbine speed were also considered as shown in Fig. 5.2 (see (Machowski et al., 2008)). The parameters of the hydraulic turbine, IEEE–ST1A excitation systems and the PSSs are presented in Appendix B. The control parameters for the IDA–PBC and PI–PBC are also shown in Appendix B.

Two faults are assumed to demonstrate the robustness and efficiency of the proposed controllers to improve the dynamic response of the power system with renewable energy integration under large disturbances. These two faults will be always employed for each proposed controller in this dissertation, which are described as follows:

- **Fault #1**: This fault is a three-phase to the ground on bus 3 in a period of 200 ms (see Fig. 5.1).

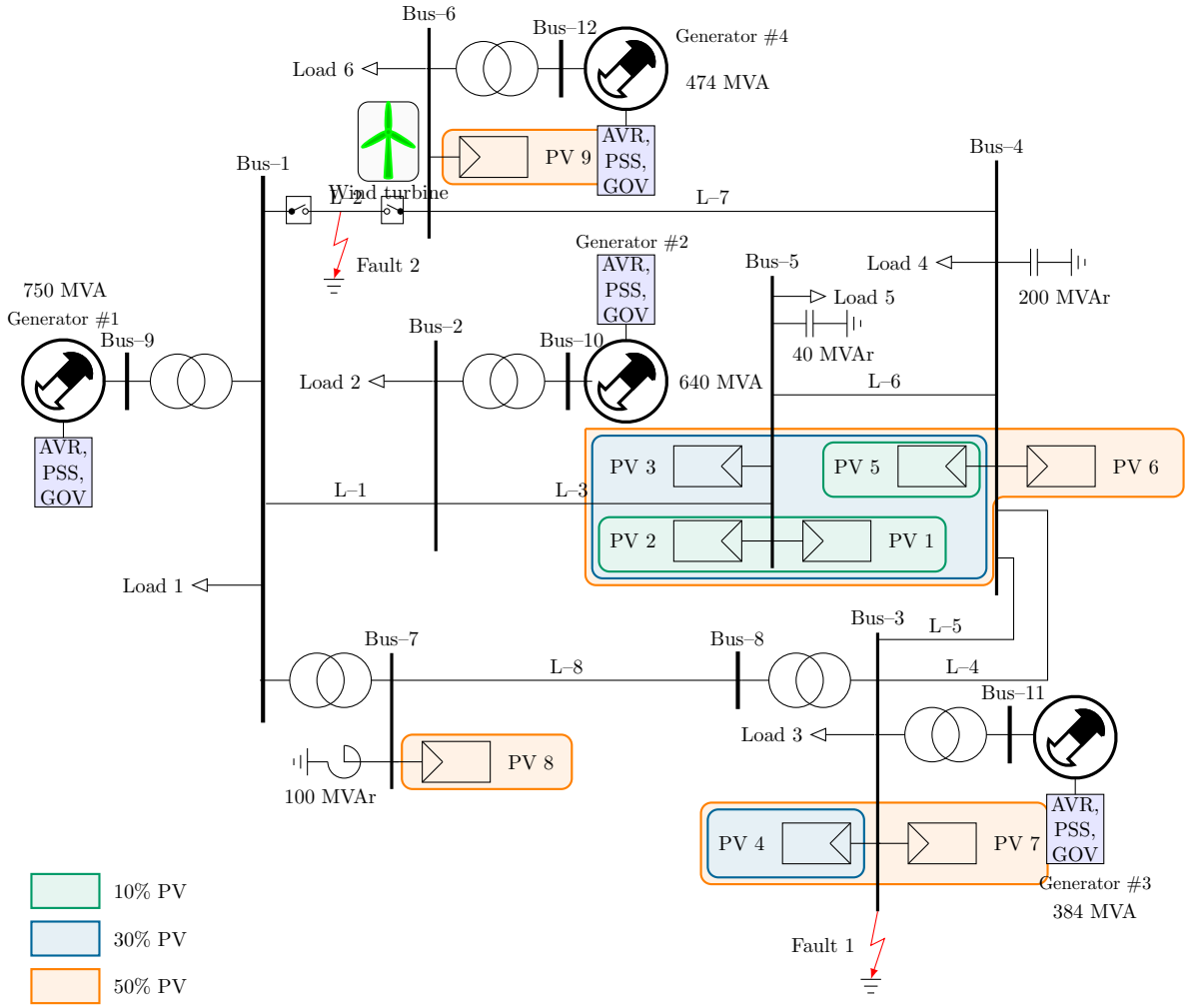

Figure 5.1: 12–bus test system

- **Fault #2**: This is a short–circuit to the ground permanent at the middle of the transmission line L–2 and the protecting system opens the transmission line after 200 ms.

To quantify the performance of the controllers, the integral of the time–weighted absolute error (ITAE) for the rotor speed deviation and the generator terminal voltage is employed, which is

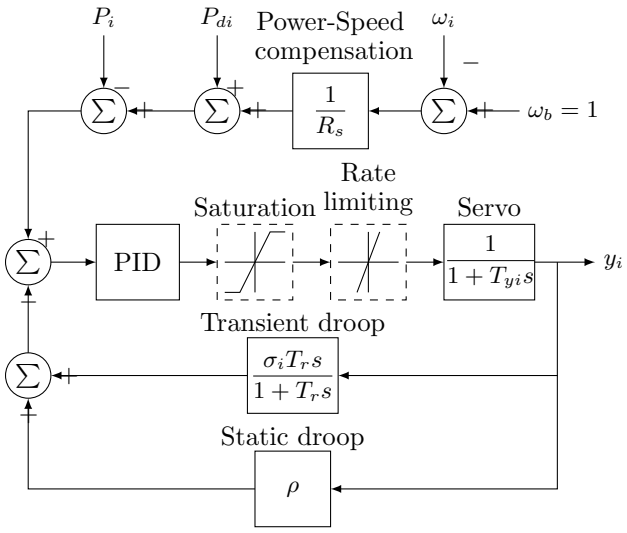

Figure 5.2: Block diagram of the governor system with static and transient droop

computed as follows:

$$\text{ITAEW} = \sum_{i=1}^{4} \int_0^{t_{sim}} t\,|\Delta\omega_i|\,dt,$$

$$\text{ITAEV} = \sum_{i=1}^{4} \int_0^{t_{sim}} t\,|\Delta v_{ti}|\,dt.$$

where t_{sim} is the final simulation time, i denotes each HTGS, $\Delta\omega_i$ is the rotor speed deviation of each generator i, and Δv_{ti} is the difference between the generator terminal voltage i and its voltage reference. The settling time t_s for the rotor speed deviation is also used. Here, the settling time is established when all $|\Delta\omega_i|$ are less than 0.0005 pu, which corresponds to the dead–band for the case of the Colombian power system (CREG, 2000). This dead–band will be marked in figures of rotor speed deviation with a gray stripe.

5.2 Test for the HTGS

This section shows the performance and robustness of the proposed decentralized control for HTGS based on the IDA–PBC to maintain the power system stability in the 12–bus test system under two large disturbances described in Section above. For each HTGS is applied the control scheme shown in Fig. 4.2. In these test only consider the PV penetration level of 10% as shown in Fig. 5.2. It was assumed that each solar power generation, delivers the same active power under similar operating conditions as the synchronous machine listed in Table 5.1.

Table 5.1: Operating Condition of Each Synchronous Machine

G1		G2		G3		G4	
P	V	P	V	P	V	P	V
3.42	1.00	4.00	1.01	2.70	1.01	3.30	1.01

All data are in per unit. $S_{Base} = 100MW$, $V_{Base} = 230kV$.

For the sake of simplicity, when referring to standard controls for the HTGS, the interpretation is as follows: the field system is controlled with an IEEE–SST1A excitation system plus an IEEE–PSS1A while the governing system is controlled with the PID control plus a static and a transient droop.

5.2.1 Fault #1 Analysis

This fault investigates the ability of the proposed control to maintain the stability and improve the power system dynamic performance with renewable energy integrated during and after a large disturbance.

Fig. 5.3 depicts the dynamic responses of the rotor speed deviation of all synchronous generators. Fig. 5.3(a) illustrates the rotor speed deviation of generators G1, G2, and G4 when the IDA–PBC is used, while Fig. 5.3(b) shows the same rotor speed deviations of the generators when the standard controls are employed. Fig. 5.3(c) compares the rotor speed deviation of generator G3 for both controllers.

It can be noted that IDA–PBC stabilizes the system in a shorter time and with lower oscillations compared to the standard controllers. Table 5.2 presents the performance indexes for fault #1, which supports the better performance of the IDA–PBC method than the standard controllers by comparing ITAEW and t_s between controllers, and these indexes are reduced in 39.87% and 22.13% according to the standard controller, respectively. Note also that the standard controller maintain a steady-state error.

Fig. 5.4(a) illustrates the dynamic responses for the voltage profiles of each synchronous generator; terminal voltages of generators G1, G2 and G4 when the IDA–PBC is implemented, while Fig. 5.4(b) depicts the same generator terminal voltages when the standard controls are employed. Fig. 5.4(c) compares the terminal voltages of generators G3 between controllers.

It is observed that the voltage profiles show an improved response when the IDA–PBC is considered. This implies that the proposed control has an enhanced ability to regulate voltage.

Table 5.2: Performance Indexes for Fault #1

	ITAEW	ITAEV	t_s [s]
Standard Controllers	49.48	312.56	10.75
IDA–PBC	29.75	74.06	8.37

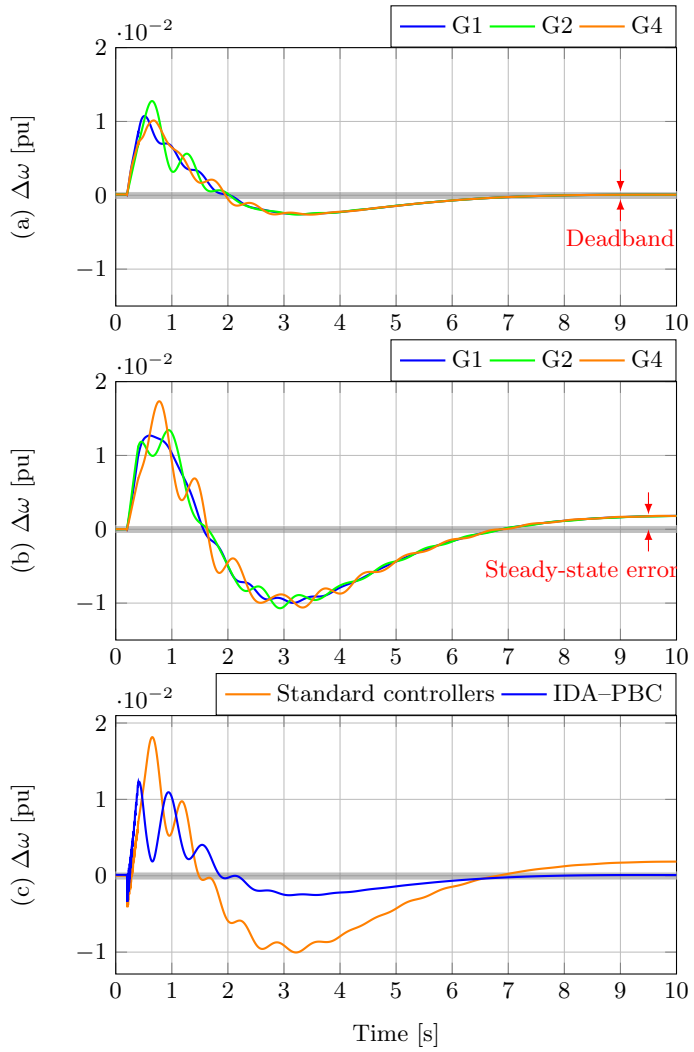

Figure 5.3: Dynamic responses of the rotor speed deviation under fault #1: (a) $\Delta\omega$ using IDA–PBC, (b) $\Delta\omega$ using standard controllers, and (c) Control strategy comparison of $\Delta\omega$ in the generator G3.

This improvement is easier to observe in Fig. 5.4(c), where the enhanced response is more clear for the proposed control. This can be verified by comparing ITAEV between control (see Table 5.2), where this index is lower for the IDA–PBC than the standard control in a 76.30%.

It is important to note that a reduction of the frequency oscillations improve the system operation and benefits the synchronous machines since the stress on the shafts is reduced. Likewise the short stabilization time improves the critical time of the protection system.

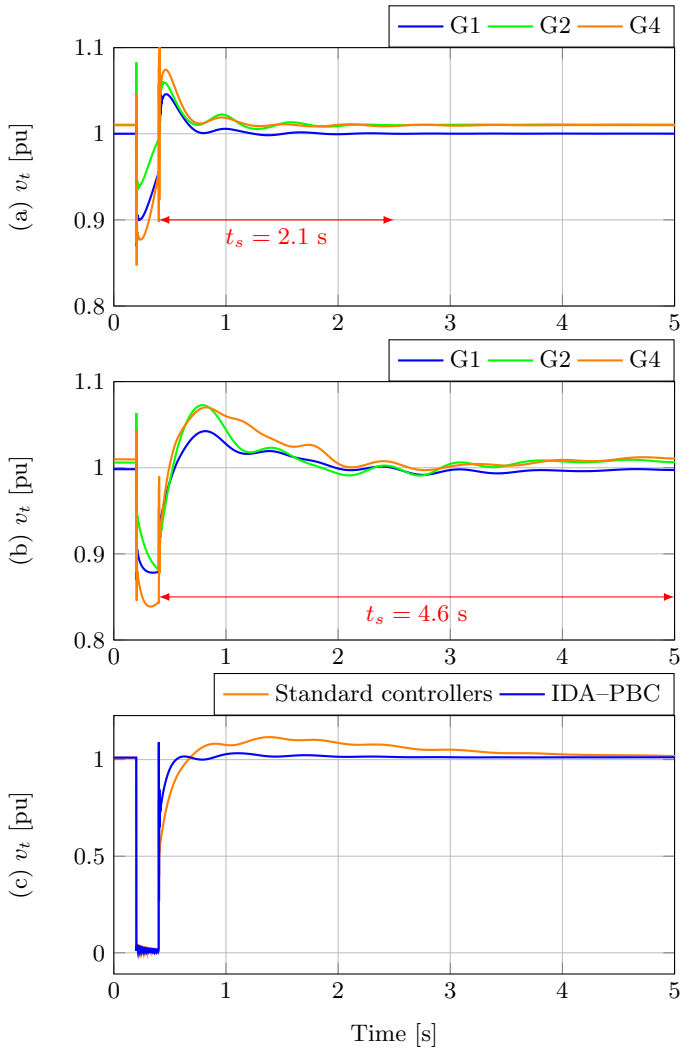

Figure 5.4: Dynamic responses of the generator terminal voltages under fault #1: (a) v_t using IDA–PBC, (b) v_t using standard controllers, and (c) Control strategy comparison of v_t in the generator G3.

5.2.2 Fault #2 Analysis

This fault investigates the ability of the IDA–PBC to improve stability when a topology change such as tripping of the transmission line L–2 occurs. Fig. 5.5 shows the dynamic behavior of the rotor speed deviation of all synchronous generators. Fig. 5.5(a) depicts the rotor speed deviation of generators G1, G2, and G3 when the IDA–PBC is used, while Fig. 5.5(b) shows the same rotor speed deviation of the generators when the standard controls are implemented. Fig. 5.5(c) compares

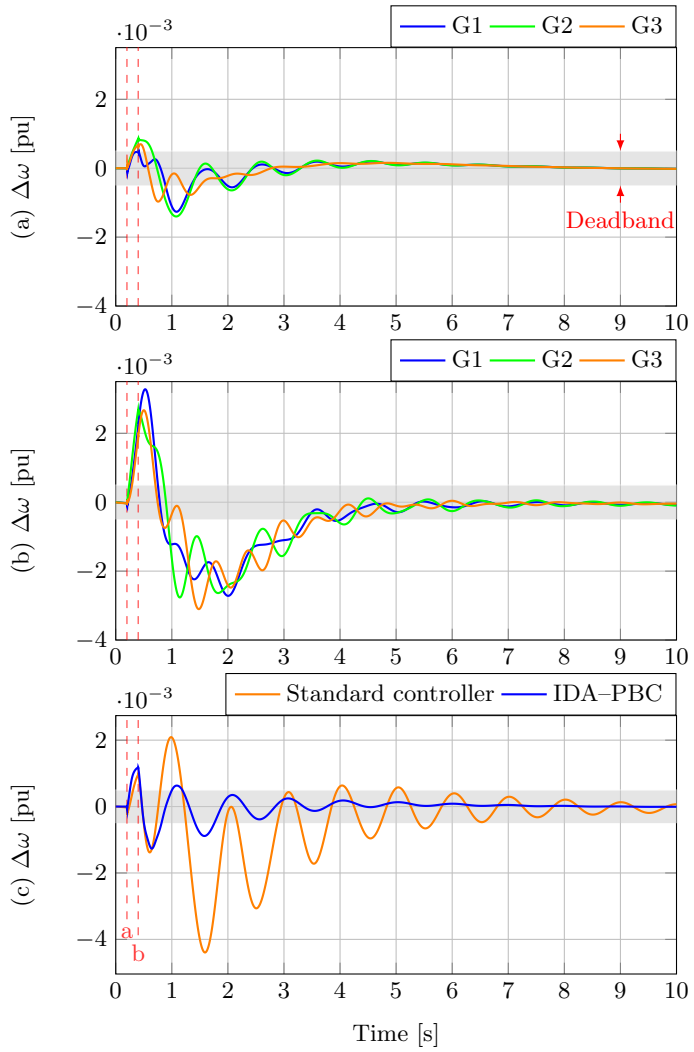

Figure 5.5: Dynamic responses of the rotor speed deviations under fault #2: (a) $\Delta\omega$ using IDA–PBC, (b) $\Delta\omega$ using standard controllers, and (c) Control strategy comparison of $\Delta\omega$ in the generator G4.

the rotor speed deviation of generator G4 for both controllers. The line a represents the instant where occurs the fault and the line b denotes the tripping of te transmission line. The performance indexes for fault #2 were shown in Table 5.3.

Fig. 5.5 shows that the IDA–PBC continues to present an enhanced response of the rotor speed deviation for all generators compared with the standard controller. Therefore, the power system's dynamic behavior is improved. This can be verified with the performance indexes of Table 5.3, where the ITAEW and t_s are lower for the proposed control than the standard control with 84.74%

and 16.11%, respectively. This difference can be observed clearly in Fig. 5.5(c) where the frequency oscillations last longer for the standard controller.

Fig. 5.6 presents the voltage profiles of each synchronous generators for fault #2. Here, Fig. 5.6(a) shows the terminal voltages of generators G1, G2 and G4 when the IDA–PBC is used, while Fig. 5.6(b) shows the same generator terminal voltages when the standard controls are implemented. Fig. 5.6(c) makes a comparison between the terminal voltages of generator G3.

In Fig. 5.6, it is observed that the voltage profiles continue to recover faster for the proposed control than the standard controllers. Here, the ITAEV is lower for the IDA–PBC than the standard control in 53.05%.

5.3 Test for the PV Plants

In this part, the proposed methodology is verified for enhancing POD by using the PV plants. The parameters of PV plants and their PI–PBC gains are in Appendix B Tables B.9 and B.11, respectively. The POD parameters are described in Table B.12. The performance and robustness of the proposed methodology are compared with the PI–PBC without POD (W–POD). In addition, we consider that the models and controls for the generators and governing systems are equipped with the IDA–PBC method used in section above.

A comparison with a classic outer–inner control was not done for two reasons. Firstly, in this part, it only analyzes the impact of the proposed methodology to improve stability in the power system during large disturbances. Secondly, the performance of PI–PBC according to a classic outer–inner control and perturbation observer–based adaptive passive control (POAPC) proposed in (Yang et al., 2017a) is analyzed for a two–terminal HVDC system in Section 5.5.

5.3.1 Different Operative Condition Analysis

Two faults illustrated in Fig. 5.1 were analyzed for the purpose of demonstrating the robustness and efficiency of the proposed methodology to improve POD. Additionally, three different penetration levels of PV plants were also considered to determine the impact of these on the power system oscillations. The number of PV plants and their penetration level was gradually increased in each scenario to show the evolution of power systems.

- Scenario 1: In this scenario, three PV plants with a total penetration level of 10% were considered. The plant locations are shown in Fig. 5.1. This scenario represented a typical power system with renewable energy penetration.

Table 5.3: Performance Indexes for Fault #2

	ITAEW	ITAEV	t_s [s]
Standard Controller	66.34	125.05	6.95
IDA–PBC	10.12	58.07	5.83

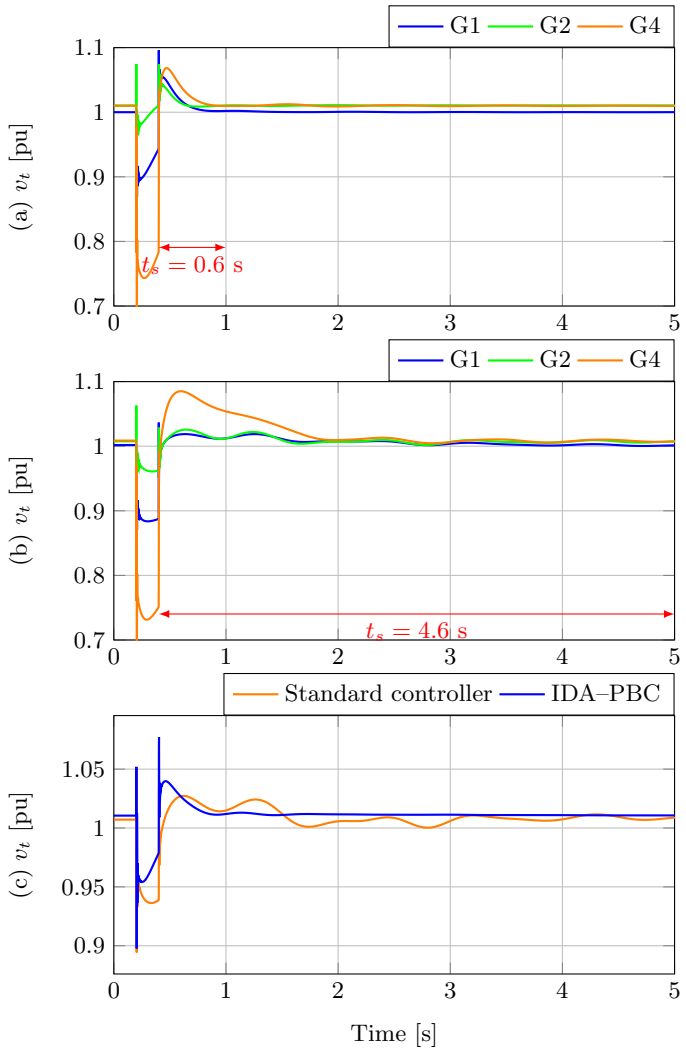

Figure 5.6: Dynamic responses of the generator terminal voltages under fault #2: (a) v_t using IDA–PBC, (b) v_t using standard controllers, and (c) Control strategy comparison of v_t in the generator G3.

- Scenario 2: In this scenario, five PV plants with a total penetration level of 30% were considered (see Fig. 5.1). This scenario evaluated a power system with renewable energy penetration in the near future.
- Scenario 3: In this scenario, nine PV plants with a total penetration level of 50% were considered (see Fig. 5.1). This scenario represents a possible case with high-level penetration that exceeds current limits of renewable penetration.

Table 5.4: Operating Conditions of Each Generator

	Generator							
	G1		G2		G3		G4	
	P	V	P	V	P	V	P	V
Scenario 1	3.42	1.00	4.00	1.01	2.70	1.01	3.30	1.01
Scenario 2	2.53	1.00	3.27	1.01	1.97	1.01	2.57	1.01
Scenario 3	1.82	1.00	2.55	1.01	1.25	1.01	1.85	1.01

All parameters are in per unit. $S_{Base} = 100MW$, $V_{Base} = 230kV$.

Note that the power delivered by each PV plant in each scenario is equal. The operating conditions of each generator for the three scenarios are summarized in Table 5.4. We first assume that dc currents (i_{dc}) of the PV plants are constant (constant radiation) (see Sections 5.3.2 and 5.3.3) and then, we consider three cases of radiation variations to study the impact on the proposed methodology (see Section 5.3.4).

5.3.2 Fault #1 Analysis

This fault investigates the ability of the proposed methodology to improve stability in the power system during and after a transient fault. Fig. 5.7 depicts the dynamic responses of the rotor speed deviations of the generators G1 and G4 for three scenarios considered. Table 5.5 shows the performance indexes for fault #1.

It is important to mention that the rotor speed deviation of generators (G1 and G4) serve as a measure of the frequency behavior of the test system.

Note in Figs. 5.7(a), 5.7(b), and 5.7(c) that the proposed methodology allows the improvement of the POD in the power system stability without forcing the dynamic response of the VSC to behave as a virtual synchronous generator as proposed in (Remon et al., 2017). It is worth noting that, ITAEWs are reduced by 18.12%, 23.50%, and 22.51% for scenarios 1, 2, and 3, respectively (see Table 5.5).

It can be also seen in Fig. 5.7(a) that the rotor speed deviations of generators G1 and G4 for scenario 1, has a more frequency oscillations than in the other two scenarios (compared with Figs. 5.7(b) and 5.7(c)). The reason is that scenarios 2 and 3 have more points of generation distributed in the whole power system, which helps improving the dynamic responses on it. In addition, the

Table 5.5: Performance Indexes for Fault #1

	Scenario 1			Scenario 2			Scenario 3		
	ITAEW	ITAEV	t_s [s]	ITAEW	ITAEV	t_s [s]	ITAEW	ITAEV	t_s [s]
POD	29.55	74.06	9.61	29.01	38.40	6.72	28.10	33.84	6.68
W–POD	23.75	72.79	8.37	22.80	38.01	6.16	21.50	33.19	6.12

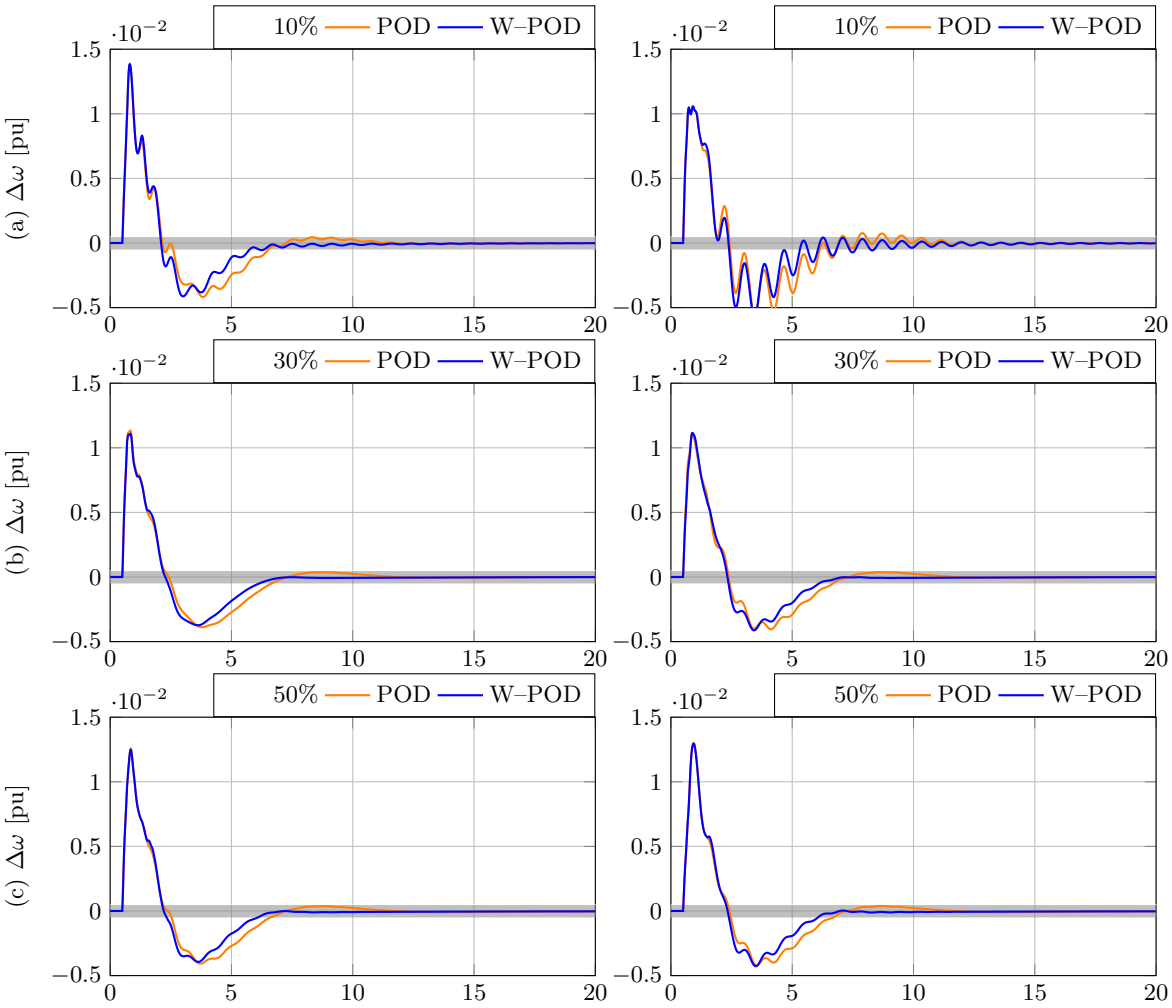

Figure 5.7: Dynamic responses of the rotor speed deviations under fault #1: (a) $\Delta\omega$ of the G1 (left) and G4 (right) for a penetration level of 10%, (b) $\Delta\omega$ of the G1 (left) and G4 (right) for a penetration level of 30%, and (c) $\Delta\omega$ of the G1 (left) and G4 (right) for a penetration level of 50%.

power oscillations are also longer as the penetration level of PV plants decreases. This is supported by comparing t_s in Table 5.5.

Fig. 5.8 illustrates the dynamic responses of the voltage profiles of generators G2 and G4. Note that the POD also helps improving the voltage profiles of power system since ITAEVs are reduced by 1.73%, 1.93%, and 3.22% for scenarios 1, 2, and 3, respectively (see Table 5.5).

Observe that the improvement is not as significant as for the HTGS. This due to the VSCs have a fast response of natural form

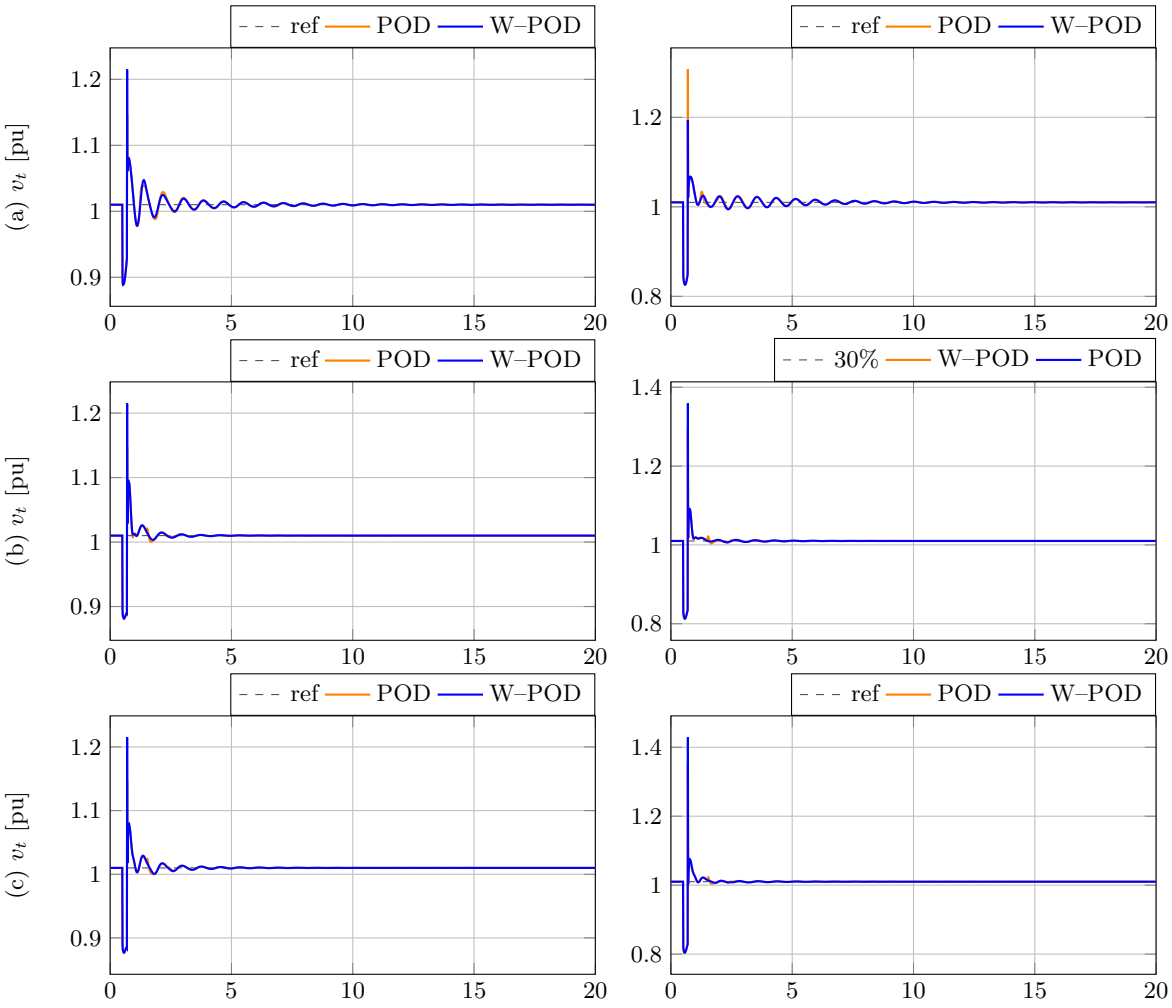

Figure 5.8: Dynamic responses of the voltage profiles under fault #1: (a) v_t of the G2 (left) and G4 (right) for a penetration level of 10%, (b) v_t of the G2 (left) and G4 (right) for a penetration level of 30%, and (c) v_t of the G2 (left) and G4 (right) for a penetration level of 50%.

5.3.3 Fault #2 Analysis

This fault investigates the ability of the proposed methodology to enhance stability for topology changes represented by disconnection of the transmission line L–2. Fig. 5.9 and 5.10 illustrate the dynamic behavior of the rotor speeds of generators (G1 and G4) and the terminal voltages of generators (G2 and G4) during a short–circuit at the middle of the line L–2, respectively. The performance indexes for fault #2 are presented in Table 5.6.

Note in Fig. 5.9 that the proposed methodology continues to improve the power system stability, stabilizing the system faster even for a topology change. For the scenario 1, 2 and 3, the ITAEWs are

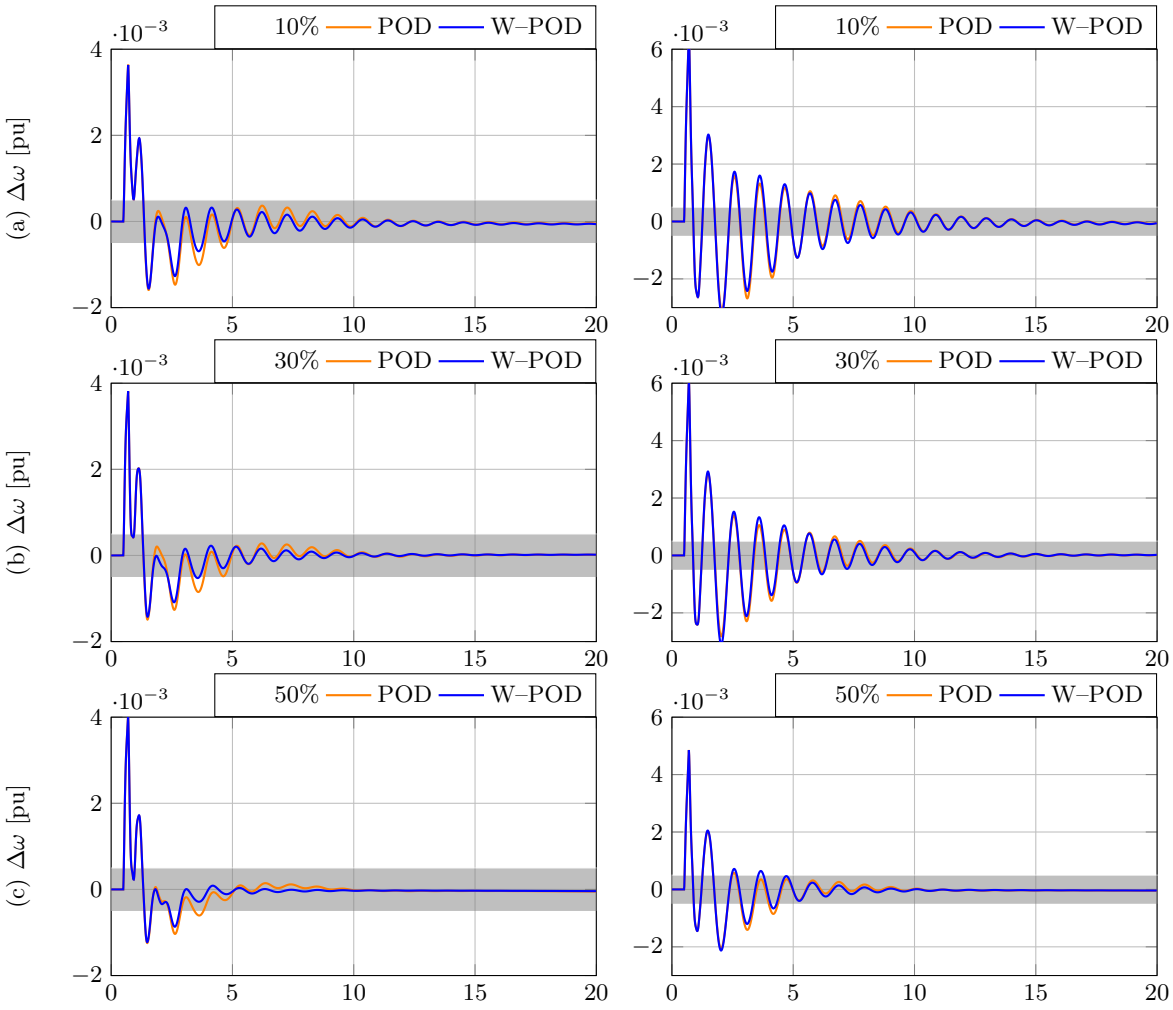

Figure 5.9: Dynamic responses of the rotor speed deviations under fault #2: (a) $\Delta\omega$ of the G1 (left) and G4 (right) for a penetration level of 10%, (b) $\Delta\omega$ of the G1 (left) and G4 (right) for a penetration level of 30%, and (c) $\Delta\omega$ of the G1 (left) and G4 (right) for a penetration level of 50%.

Table 5.6: Performance Indexes for Fault #2

	Scenario 1			Scenario 2			Scenario 3		
	ITAEW	ITAEV	t_s [s]	ITAEW	ITAEV	t_s [s]	ITAEW	ITAEV	t_s [s]
POD	10.12	58.42	8.85	6.60	34.52	7.77	5.52	20.48	4.37
W–POD	9.996	58.07	8.37	5.83	33.43	6.77	4.48	20.48	4.31

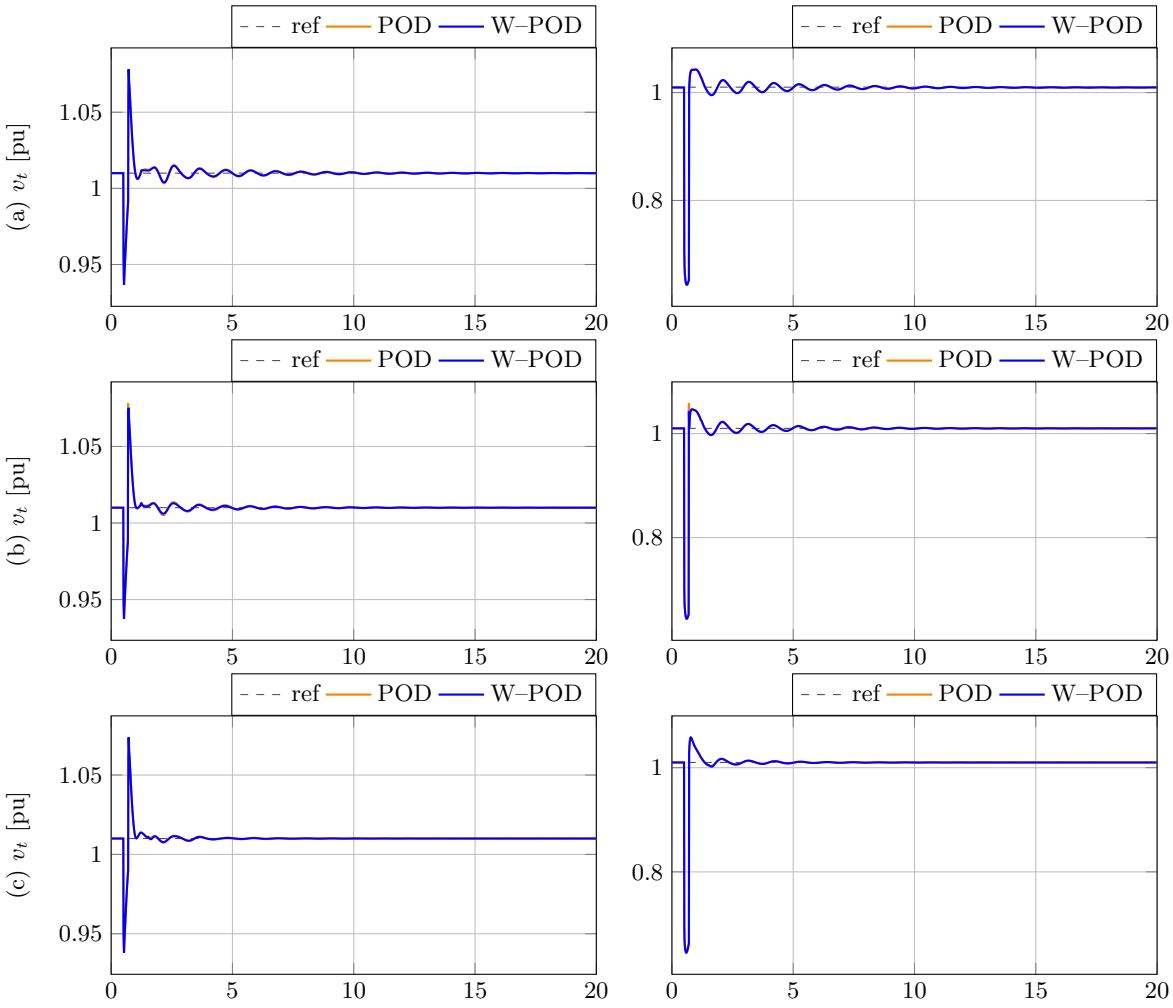

Figure 5.10: Dynamic responses of the voltage profiles under fault #2: (a) v_t of the G2 (left) and G4 (right) for a penetration level of 10%, (b) v_t of the G2 (left) and G4 (right) for a penetration level of 30%, and (c) v_t of the G2 (left) and G4 (right) for a penetration level of 50%.

reduced by 1.52%, 11.65%, and 18.78% when the proposed methodology is used. This demonstrates that the proposed methodology has an impact on the damping of the frequency oscillations. This clearly benefits the synchronous machines by reducing the stress of the shaft.

In Fig. 5.10 can be noted that the regulation of voltage profiles also present an enhanced when the POD is implemented. This can be supported by comparing their ITAEVs since these are reduced by 0.58%, 3.15%, and 3.76% when the proposed methodology is employed.

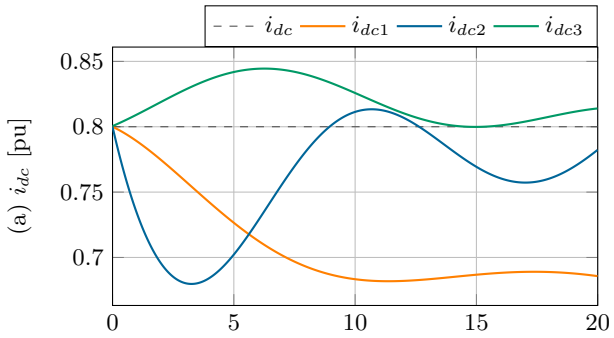

Figure 5.11: The dc current i_{dc} on dc–link of the PV plants: - - - i_{dc} base case, — i_{dc1} radiation deep, — i_{dc3} radiation droop, and — i_{dc3} radiation oscillation.

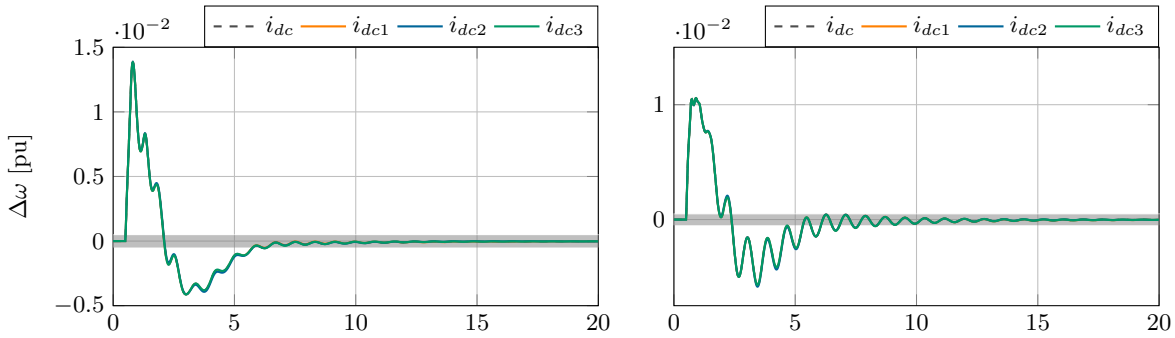

Figure 5.12: Dynamic responses of the rotor speed deviations for radiation variations: $\Delta\omega$ of the G1 (left) and G4 (right) for a penetration level of 10%.

Table 5.7: Performance Index for Radiation Variations

	- - - i_{dc}	— i_{dc1}	— i_{dc3}	— i_{dc3}
ITAEW	23.75	23.97	23.82	23.71

5.3.4 Radiation Variation Analysis

This part analyzes the impact on the proposed methodology when considering radiation variations during and after a large disturbance. Three cases of radiation variations were considered which are illustrated in Fig. 5.11. These cases are only compared when the POD methodology is used for scenario 1 since it scenario presented more frequency oscillations. Fig. 5.12 depicts the dynamic behavior of the rotor speeds of generators (G1 and G4) for fault #1 when radiation variations are considered. The performance indexes for radiation variations are presented in Table 5.7

Note that the radiation does not have a significant effect in the proposed methodology since the dynamic responses maintain the same behavior and the ITEAWs are similarly (see Table 5.7).

5.4 Test for the SMES system

In this part, it studies the proposed methodology shown in Chapter 4 for improving POD by using the SMES system. The SMES system is connected to bus 5, whose model was described in Chapter 3 and its control scheme was illustrated in Fig. 4.6. the use of the SMES system in the improvement of power systems stability is justified in (Ortega and Milano, 2016) since the largest installed SMES system has a capacity of 100 MJ and can provide 100 MW peak and ±50 MW oscillatory power (Luongo et al., 2003). The P–POD and Q–POD of the SMES system were only assessed for scenario 1 since it scenario presented more frequency oscillations. The parameters of SMES system and their PI–PBC gains are in Appendix B Tables B.10 and B.11, respectively. Here, we also consider that the models and controls for the generators and governing systems are equipped with the IDA–PBC method used in section 5.2.1. Four cases are also considered to test the impact of the P–POD and Q–POD for the SMES system in the power system oscillations.

- Case 1: This is a base case, which the generators and governing systems were equipped with the IDA–PBC method with a total penetration level of 10%.
- Case 2: In this case, the POD for the PV plants was employed whose results were shown in the previous section.
- Case 3: In this case, the P–POD and Q–POD for the SMES system were used in the base case (Case 1).
- Case 4: In this case, the P–POD and Q–POD for the SMES system plus the POD for the PV plants were implemented.

5.4.1 Fault #1 Analysis

This fault studied the ability of the proposed methodology for the SMES system of improving stability in the power system during and after a transient fault. Fig. 5.13 shows the dynamic responses of the rotor speed deviations of the generators. Table 5.8 shows the performance indexes for fault #1.

Note in Fig. 5.13 that the proposed methodology for the SMES system helps the improvement of the POD in the power system stability (compare Case 1 and Case 3). The best performance of the dynamic response of the rotor speed deviations presented when the methodologies for the PV plants and the SMES system were implemented at the same time. It should be noted that ITAEWs

Table 5.8: Performance Indexes for Fault #1

	Case 1	Case 2	Case 3	Case 4
ITAEW	29.55	23.75	16.47	16.12
ITAEV	74.06	72.79	65.91	60.32
t_s [s]	9.61	8.37	8.37	8.77

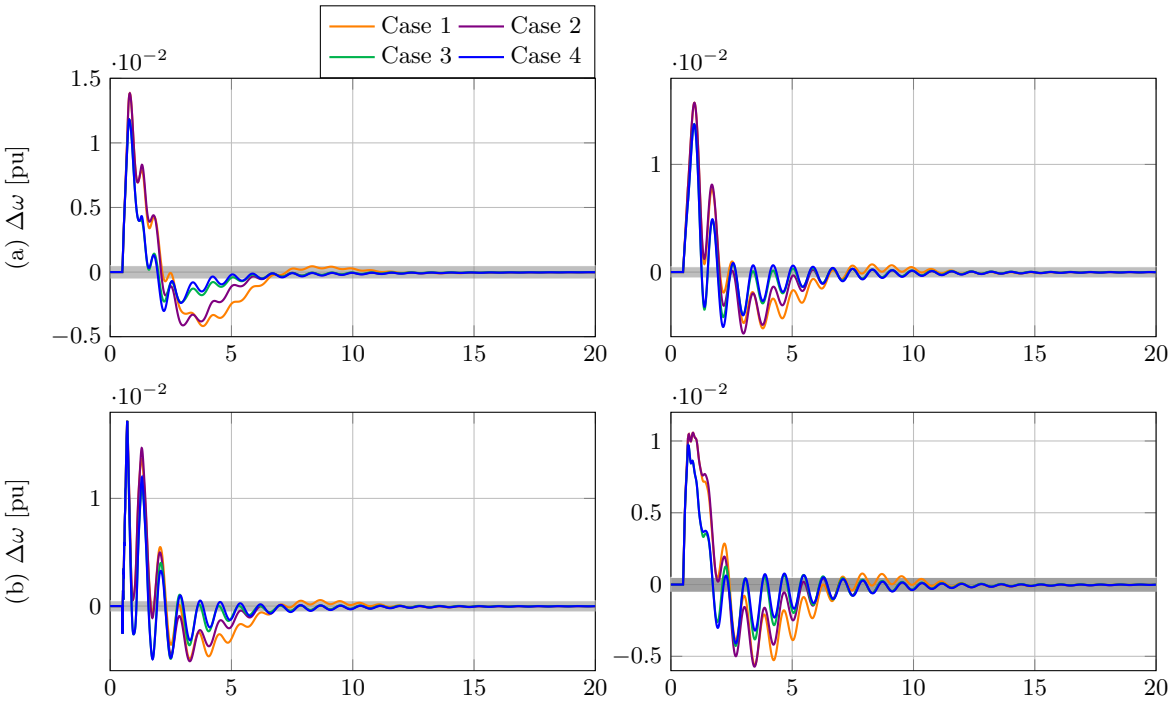

Figure 5.13: Dynamic responses of the rotor speed deviations when the SMES system is implemented for fault #1: (a) $\Delta\omega$ of the G1 (left) and G2 (right) and (b) $\Delta\omega$ of the G3 (left) and G4 (right).

were reduced by 44.26% and 45.44% for cases 2, and 3 according to case 1, respectively (see Table 5.8).

Fig. 5.14 illustrates the dynamic responses of the voltage profiles of generators. Note that the Q–POD also helped improving the voltage profiles of power system since ITAEVs were reduced by 11.01% and 18.67% for cases 2, and 3 according to case 1, respectively (see Table 5.8).

5.4.2 Fault #2 Analysis

This fault analyzed the performance of the proposed methodology for the SMES system of enhancing stability in the power system when a topology change such as tripping of the transmission line L–2 occurs. Fig. 5.15 depicts the dynamic responses of the rotor speed deviations of the generators. Table 5.9 lists the performance indexes for this fault.

In Fig. 5.15, it can be noted that the rotor speed deviation of all generators stabilized the system in a shorter time and with lower oscillations for the case 4 than other cases. This is supported by comparing ITAEW and t_s between cases, and these indexes are reduced by 33.00% and 41.69% for the case 4 according to case 1, respectively.

Fig. 5.16 illustrates the dynamic responses of the voltage profiles of each synchronous generator. As can been note that the voltage profiles present an improved responses when the methodologies

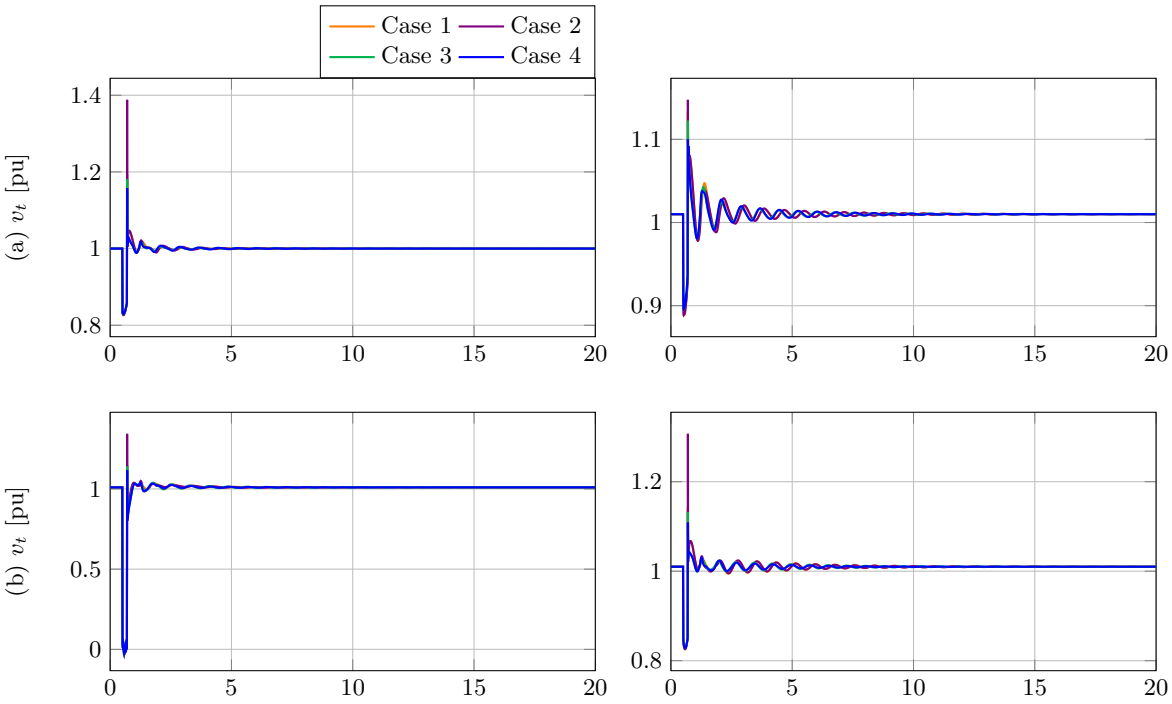

Figure 5.14: Dynamic responses of the voltage profiles of the generators when the SMES system is implemented for fault #1: (a) v_t of the G1 (left) and G2 (right) and (b) v_t of the G3 (left) and G4 (right).

Table 5.9: Performance Indexes for Fault #2

	Case 1	Case 2	Case 3	Case 4
ITAEW	10.12	9.996	7.60	6.78
ITAEV	58.42	58.07	22.13	21.71
t_s [s]	8.85	8.37	5.18	5.16

for the PV plants and the SMES system were implemented at the same time. This was verified by comparing ITAEV between cases (see Table 5.9), where this index was lower for the case 4 than case 1 in a 62.83%.

It is important to highlight that case 4 analyzed in this section corresponds to the test where all the controllers are assessed. The case 4 is when the IDA–PBC for the HTGS and the POD methodologies for the PV plants and the SMES system work together to improve the dynamic responses in the power system which is achieved. Since this case is where the best performances for the ITAEW and the ITAEV are presented (see Tables 5.8 and 5.9). However, the SMES system is the device that contributes most to the enhancement of the POD in the power system stability. This mainly due to the SMES system is dedicated to make this function.

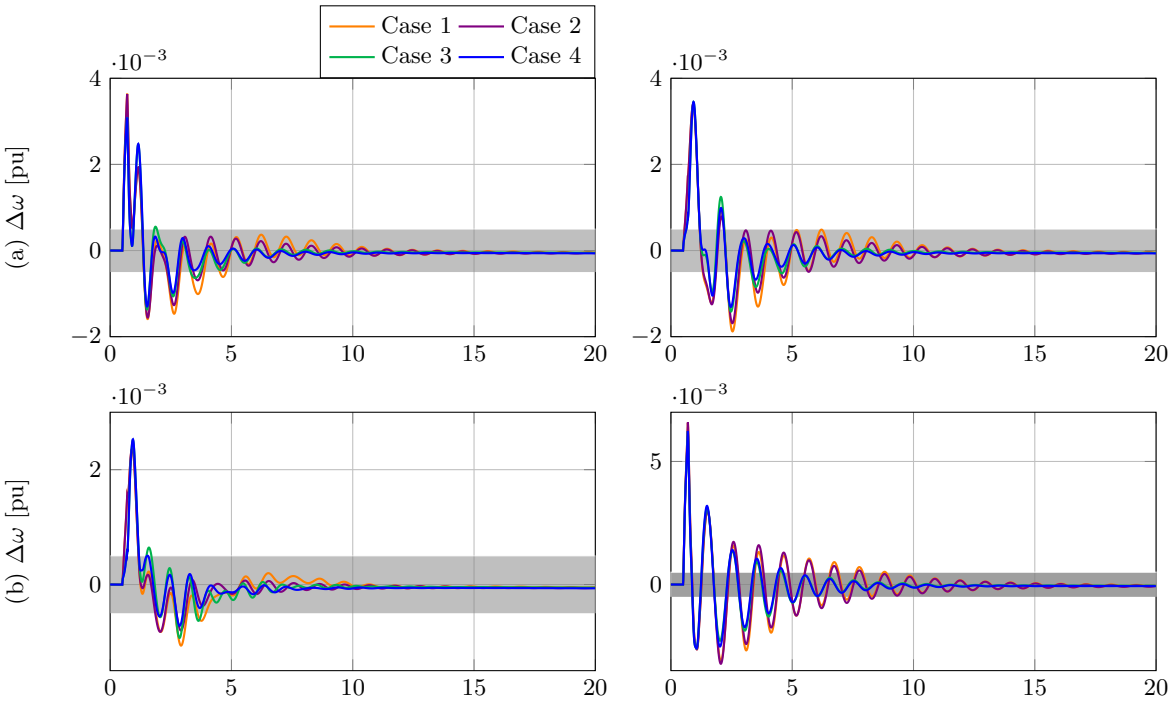

Figure 5.15: Dynamic responses of the rotor speed deviations when the SMES system is implemented for fault #2: (a) $\Delta\omega$ of the G1 (left) and G2 (right) and (b) $\Delta\omega$ of the G3 (left) and G4 (right).

At present, the SMES system is an expensive device, all the same, its cost will be gradually reduced by progressing superconductivity technology. According to the selected SMES system would have approximately an investment of \$50.000.000 ($\approx$ 0.5\$/J (Zhu et al., 2013)). Even though this investment may be considerable, the SMES system can be also used in another application such as reactive power support (Aly et al., 2016), load frequency control (Pappachen and Fathima, 2016), mitigation of subsynchronous resonance (Gil-González et al., 2018; Sedighizadeh et al., 2018), among others. For example, subsynchronous resonance problems can damage the shaft in power plants, which be much more expensive than the SMES. In addition, this could stop the operation in power plant as occurred in Peru in 2016 (SINAC, 2017), where subsynchronous oscillations produced fissures in shafts of 4 units after almost two weeks of entering into operation in July 2016 in the Puerto Bravo thermal power plant (720 MW) (SINAC, 2017). The blackouts can generate significant economic losses that can go up to \$1.000.000/h, as happened in 2014 in Barranquilla (Colombia) (El Heraldo, 2014). Therefore, the possible prolonged interruptions of power plants can produce much higher costs and also affect social consequences than the cost of a SMES system. As a result, it is justified to use SMES power systems to avoid financial losses.

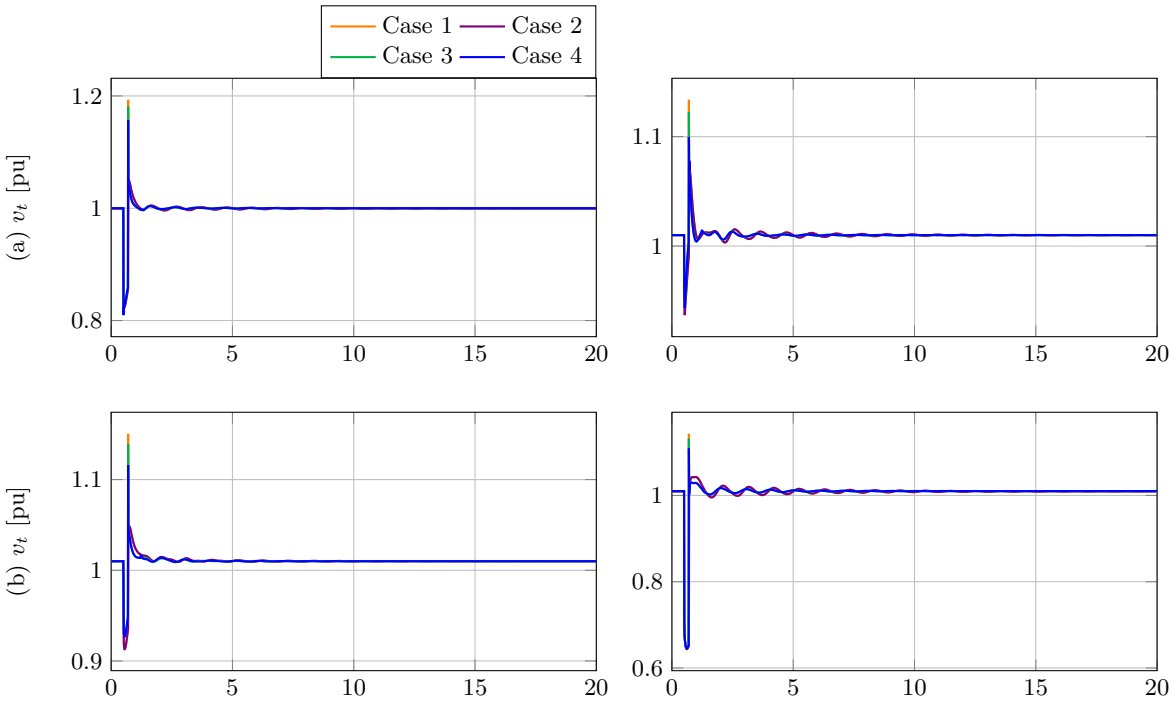

Figure 5.16: Dynamic responses of the voltage profiles of the generators when the SMES system is implemented for fault #2: (a) v_t of the G1 (left) and G2 (right) and (b) v_t of the G3 (left) and G4 (right).

5.5 Test for the VSC–HVDC System

In this part, it is analyzed the proposed controller for a two–terminal VSC–HVDC system and its effect in the power system stability. For this reason, two analyses are taken separately. First, the performance and robustness of the proposed controller is assessed in a single HVDC line that connects two systems with independent frequency. Second, a two–terminal VSC–HVDC system is included in the test system shown Fig. 5.1.

5.5.1 Proposed Controller Assessment for the VSC–HVDC System

The proposed controller is checked in a two–terminal VSC–HVDC system, as presented in Fig. 3.5. We selected the VSC_2, which regulates the dc–link voltage and the reactive power, as the master controller, while the VSC_1 controls the active and reactive power independently. The frequencies of $network_1$ and $network_2$ are 50 Hz and 60 Hz, respectively. The parameters of the VSC–HVDC system are listed in Table B.14, which are presented in (Yang et al., 2018a).

The PI–PBC performance was assessed in different operating cases and compared with PI controller. The PI controller is designed as a standard cascade control structure containing inner

Table 5.10: Average errors for the Case 1.

Controller	P_1 [%]	Q_1 [%]	Q_2 [%]	v_{dc2} [%]
PI controller	0.239	0.045	0.016	0.325
POAPC controller	0.197	0.044	0.016	0.192
PI–PBC	0.097	0.043	0.016	0.123

loop current controllers and outer loop voltage/power controllers. The difference is the standard decoupling of the d–axis and q–axis, while in the DPC model, they are changed by the active and reactive power, respectively. In addition, a comparison with perturbation observer-based adaptive passive control (POAPC) for damping improvement proposed in (Yang et al., 2017a) was also made, which only needs the measurement of dc voltage and active and reactive power, does not depend on the parameters of the system. Tables B.15 and B.16 show the PI–PBC and PI parameters, respectively. The control inputs are bounded like $|m_{di}| \leq \sqrt{2}/2,\ |m_{qi}| \leq \sqrt{2}/2\ \forall i = 1, 2$.

Case 1: Active and reactive power control

Arbitrary references of active and reactive power are selected for the VSC_1, while the VSC_2 have to keep its dc–link voltage in nominal value and control its reactive power. The system responses are provided in Fig. 5.17 and the average errors are shown in Table 5.10. It was observed that all of the controllers achieve the reference values for the active and reactive power. However, the average errors are lower for the proposed controller than the PI and POAPC controllers (see Table 5.10), which presents a better performance when there are changes in active and reactive power. It can also be seen that the voltage of dc-link was affected when it presented a change of power references in either VSC_1 or VSC_2 (see Fig. 5.17(d)). Even though the PI–PBC presented a higher peak than PI and POAPC controllers, it can come back to the desired value in less time. Additionally, The PI controller maintained a steady-state error. On the other hand, we did not consider step references for the active and reactive power since it entails high power changes on the capacitor and transformers that could produce undesired protection operations.

Case 2: Offshore wind farm connection

A wind farm is connected to the ac network$_1$, where all available active power is extracted, and all reactive power is compensated. In addition, the terminal voltage V_{T1} varies in time due to the indeterminacy and stochastic variation of wind speed (Yang et al., 2016a). Fig. 5.18 illustrates the system responses, while Table 5.11 shows their the average errors. In Figs. 5.18(b) and 5.18(d), it can be noted that the controllers can extract all active power available. However, the proposed controller presents a lower average error than the PI controller which indicates that the PI–PBC has better efficiency. Besides, this demonstrated the better performance of the proposed controller for reference tracking. The reactive power compensation is also achieved in the controllers. It was observed in Fig. 5.18(e) that the voltage regulation on dc–link does not is a great difference among controllers. Nevertheless, the proposed controller continues to present a better performance than the PI and POAPC controllers (see Fig. 5.18(d))

Case 3: A three–phase fault at ac bus

A three–phase fault occurs at bus 2 (PCC_2) for 200 ms, which causes a shift from 2.7 s to 2.9 s.

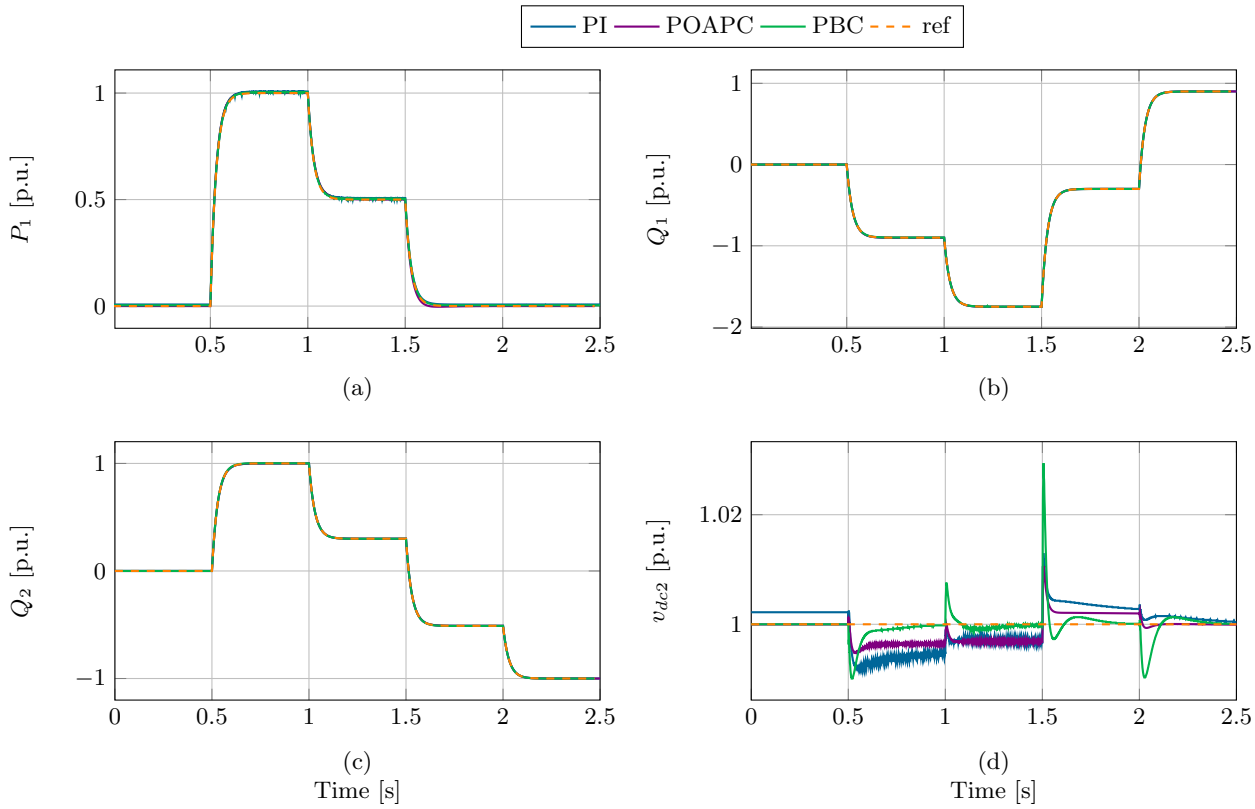

Figure 5.17: System responses for the Case 1: (a) Active power for the VSC_1, (b) Reactive power for the VSC_1, (c) Reactive power for the VSC_2, and (d) dc–link voltage for the VSC_2.

Table 5.11: Average errors for the Case 2.

Controller	P_1 [%]	Q_1 [%]	P_2 [%]	v_{dc2} [%]
PI controller	0.118	0.151	0.120	0.097
POAPC controller	0.003	0.044	0.016	0.052
PI–PBC	0.002	0.001	0.010	0.043

Remember that the fault becomes the magnitude voltage V_{T2} to a critical level. This case wants to show the ability of the controller to regulate the dc–link voltage and maintain the power references under large disturbance in the ac networks. Fig. 5.19 presents the system responses, and the average errors are listed in Table 5.12. Note that the active power absorbed at (PCC_1) does not have a greater effect when a fault at bus 2 occurs (see Fig. 5.19(a)). The reactive power control in VSC_2 is not affected either. Although, the PI–PBC presents a greater disturbance than the PI controller, but, it does not have a steady-state error. It can be observed in Fig. 5.19(c) that the controller exhibit similar behavior and both can successfully restore the active power in a few oscillations.

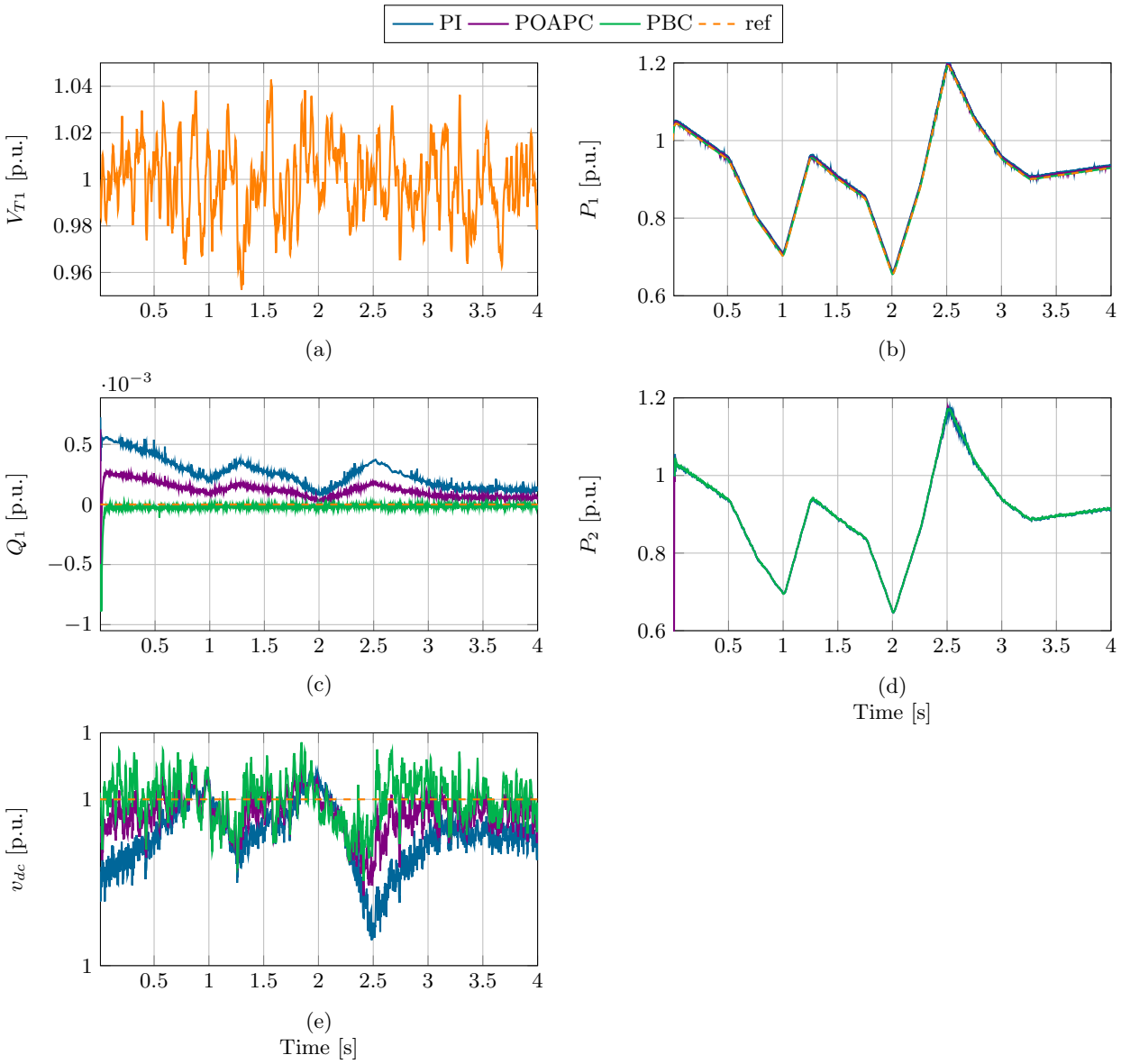

Figure 5.18: System responses for the Case 2: (a) Terminal voltage in the ac network$_1$, (b) Active power for the VSC$_1$, (c) Reactive power for the VSC$_1$, (d) Reactive power for the VSC$_2$, and (e) dc-link voltage for the VSC$_2$.

In Fig. 5.19(d) should be noted that the proposed controller can effectively regulate the dc–link voltage with fewer oscillations than the PI controller. In addition, this has a lower average error as shown in Table 5.12.

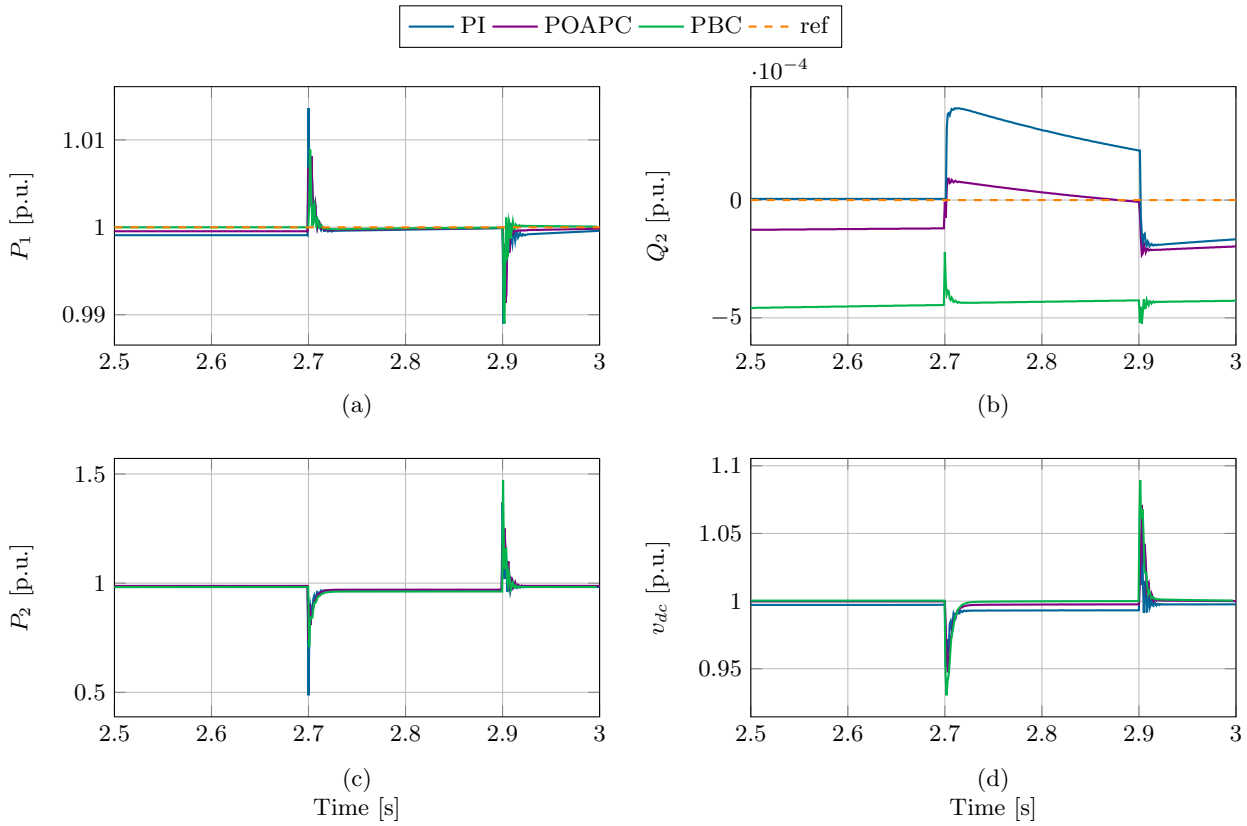

Figure 5.19: System responses for the Case 3: (a) Active power for the VSC_1, (b) Reactive power for the VSC_1, (c) Reactive power for the VSC_2, and (d) dc-link voltage for the VSC_2.

Table 5.12: Average errors for the Case 3.

Controller	P_1 [%]	Q_2 [%]	P_2 [%]	v_{dc2} [%]
PI controller	0.035	0.072	1.232	0.502
POAPC controller	0.022	0.057	1.016	0.329
PI–PBC	0.018	0.044	1.085	0.220

Case 4: Uncertainties in the system resistance and inductance. A variation in the parameters is analyzed since these may change significantly when occurring a fault in power system (Yang et al., 2017a). We assume that there are plant–model mismatches of R_1 and L_1 at the same time with 20% uncertainty when a 30% grid voltage V_{T1} drop appears. Fig. 5.20 illustrates the absolute peak value of the active power $|P_1|$, which is used for a clear comparison. The magnitude variation of the active power $|P_1|$ is around 1%, 0.6%, and 0.1%, for the PI, POAPC, and PI–PBC controllers, respectively. Even though all controller presents a good performance, the PI–PBC can estimate

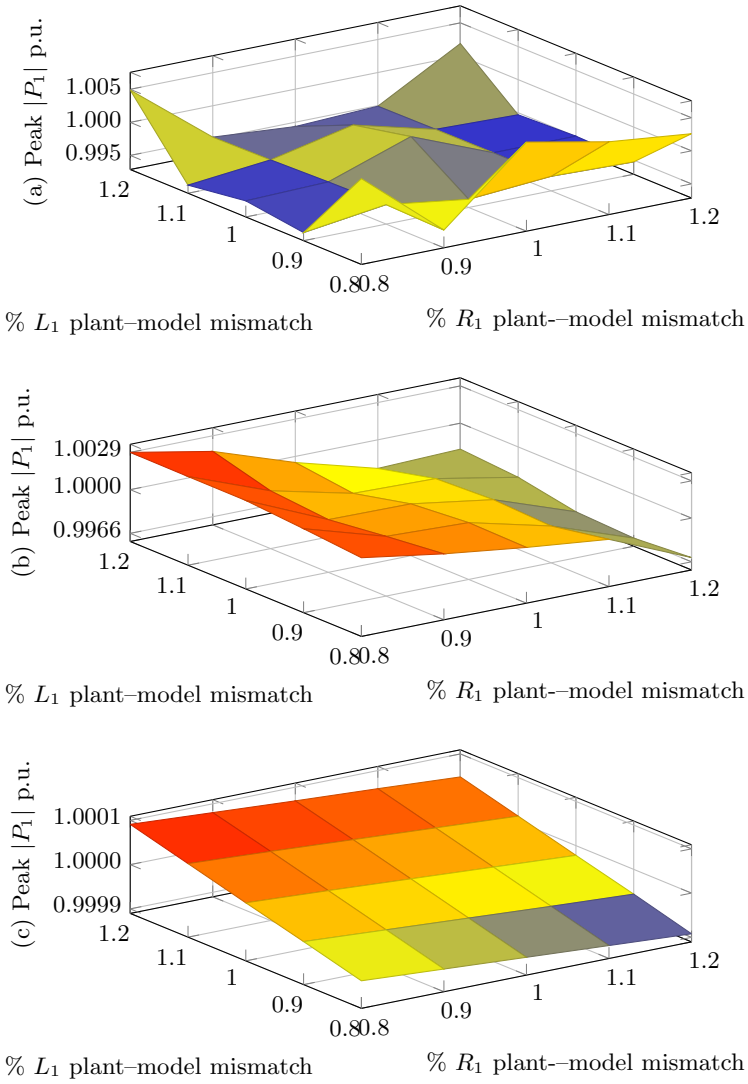

Figure 5.20: The peak active power $|P_1|$ to a 30% grid voltage V_{T1} drop for plant–model mismatches in the range of 20% (different parameters may change at the same time): (a) PI controller, (b) POAPC controller, (c) PI–PBC controller.

and compensate of better form parameter uncertainties than the PI and POAPC controllers.

The ITAE index is used to quantify the controller performance. Table 5.13 lists the ITAE of each case proposed in this Section. Note that PI–PBC has a slightly lower ITAE than the PI and POAPC controllers in the power control, while it can provide greater robustness and better performance in the case of the Offshore wind farm connection and a three–phase fault at ac bus than the PI controller. Since the control law computed for the PI–PBC does not depend on the

system model. Concerning the POAPC controller, the PI–PBC has the advantage that it is easier to implement and the disadvantage is that it needs two more measurements than the POAPC controller like v_{dc1} for the VSC_1 the and P_2 for the VSC_2. The ITAEs for the control laws are also used to compute their efforts of the controllers, which are computed as follows

$$\text{ITAE} = d \int_0^{t_s} \sum_{i=1}^{2} \left(|m_{di}| + |m_{qi}| \, t \right) dt$$

Table 5.14 lists the efforts of the controllers for all cases. Note that all of the controllers employ control efforts similar.

In Fig. 5.21 is shown the control inputs of the VSC_1 for the Case 1. In this figure can be observed that all of the control inputs do not have problem saturation.

5.5.2 Assessment of the Inclusion of a VSC-HVDC System in Power System

In this part, it investigates the effect that has the inclusion of a two-terminal VSC–HVDC system in the 12–bus test system under two large disturbances described in Section 5.1. Here, the transmission line L–5 of the test system shown in Fig. 5.1 is changed by a VSC–HVDC system. The effect of the inclusion is only analyzed for the best case presented in section above, which is the case 4.

Table 5.13: Performance indexes of each control schemes.

Case / Controller	Active and reactive power control			
	$ITAE_{P_1}$	$ITAE_{Q_1}$	$ITAE_{Q_2}$	$ITAE_{v_{dc2}}$
PI controller	7.41	1.13	0.41	8.67
POAPC controller	5.86	1.09	0.41	4.24
PI–PBC	5.85	1.07	0.41	4.11
Case / Controller	Offshore wind farm connection			
	$ITAE_{P_1}$	$ITAE_{Q_1}$	$ITAE_{P_2}$	$ITAE_{v_{dc2}}$
PI controller	27.75	368.83	26.43	5.05
POAPC controller	2.73	20.45	13.97	2.31
PI–PBC	2.72	3.17	13.81	2.12
Case / Controller	A three–phase fault at ac bus			
	$ITAE_{P_1}$	$ITAE_{Q_1}$	$ITAE_{Q_2}$	$ITAE_{v_{dc2}}$
PI controller	0.55	0.60	18.38	6.95
POAPC controller	0.30	0.54	16.16	3.75
PI–PBC	0.26	0.52	16.15	3.09

Table 5.14: The control efforts of each control schemes.

Controller	Case 1	Case 2	Case 3
PI controller	2.71	4.37	1.41
POAPC controller	2.79	4.36	1.52
PI–PBC	2.85	4.52	1.49

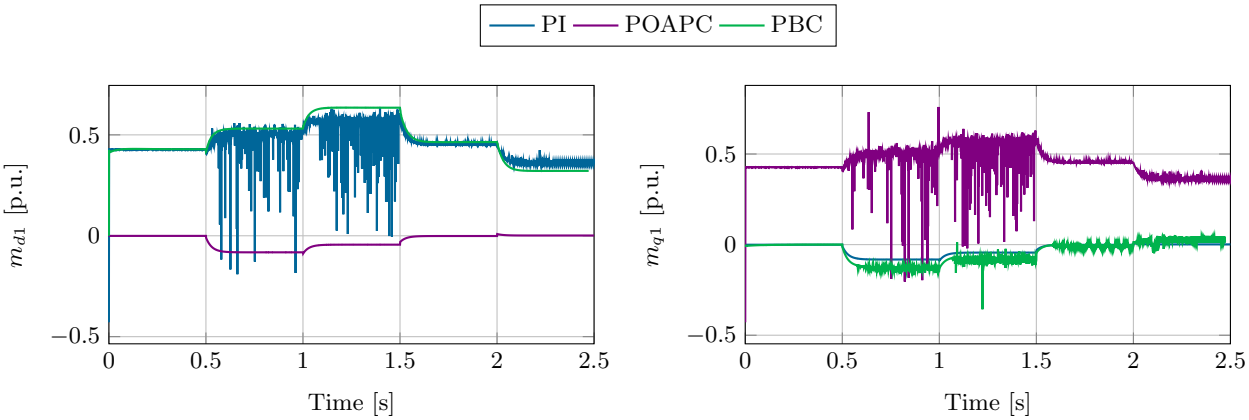

Figure 5.21: Control responses for the Case 1.

5.5.2.1 Fault #1 Analysis

This fault studies the effect of a two–terminal HVDC in the power system stability during and after a transient fault. Fig. 5.22 shows the dynamic responses of the rotor speed deviations of the generators. Table 5.15 shows the performance indexes for fault #1.

Observe in Fig. 5.22 that the inclusion of an HVDC system affects the dynamic response of the rotor speed deviations. For the generator G1 and G3, the HVDC system increases rotor speed oscillations, while the generator G2 and G4, rotor speed oscillations are decreased. This implies that it is not possible to reach a general conclusion as to how the stability in the power system is affected by the inclusion of an HVDC system since it depends on the operation point of the system. Even so though the settling time is reduced by 30.14%.

Fig. 5.23 illustrates the dynamic responses of the voltage profiles of generators. Note that the

Table 5.15: Performance Indexes when the HVDC system is considered

	Fault #1	Fault #2
ITAEW	19.22	6.86
ITAEV	52.60	21.91
t_s [s]	7.71	6.13

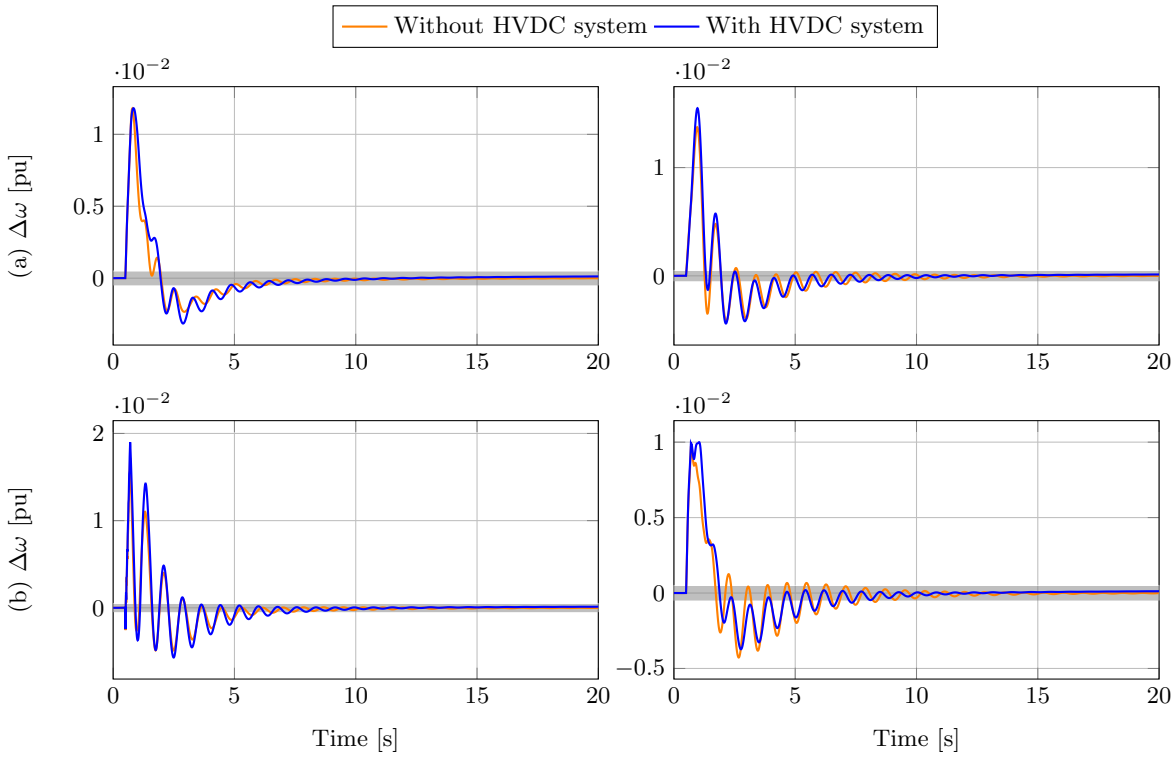

Figure 5.22: Dynamic responses of the rotor speed deviations when the HVDC system is considered for fault #1: (a) $\Delta\omega$ of the G1 (left) and G2 (right) and (b) $\Delta\omega$ of the G3 (left) and G4 (right).

HVDC system helps enhancing the voltage profiles of power system since ITAEV is reduced by 12.79%.

5.5.2.2 Fault #2 Analysis

This fault analyzes the effect of a two–terminal HVDC in the power system stability when a topology change such as tripping of the transmission line L–2 occurs. Figs. 5.24 and 5.25 depict the dynamic responses of the rotor speed deviations and the voltage profiles of the generators. Table 5.15 also lists the performance indexes for fault #2.

Observe in Figs. 5.24 and 5.25 that the inclusion of the HVDC system under fault #2 has a similar dynamic response when it is not considered. This indicates that when there are no large disturbances the behavior of the power system does not sufficiently affect the HVDC system.

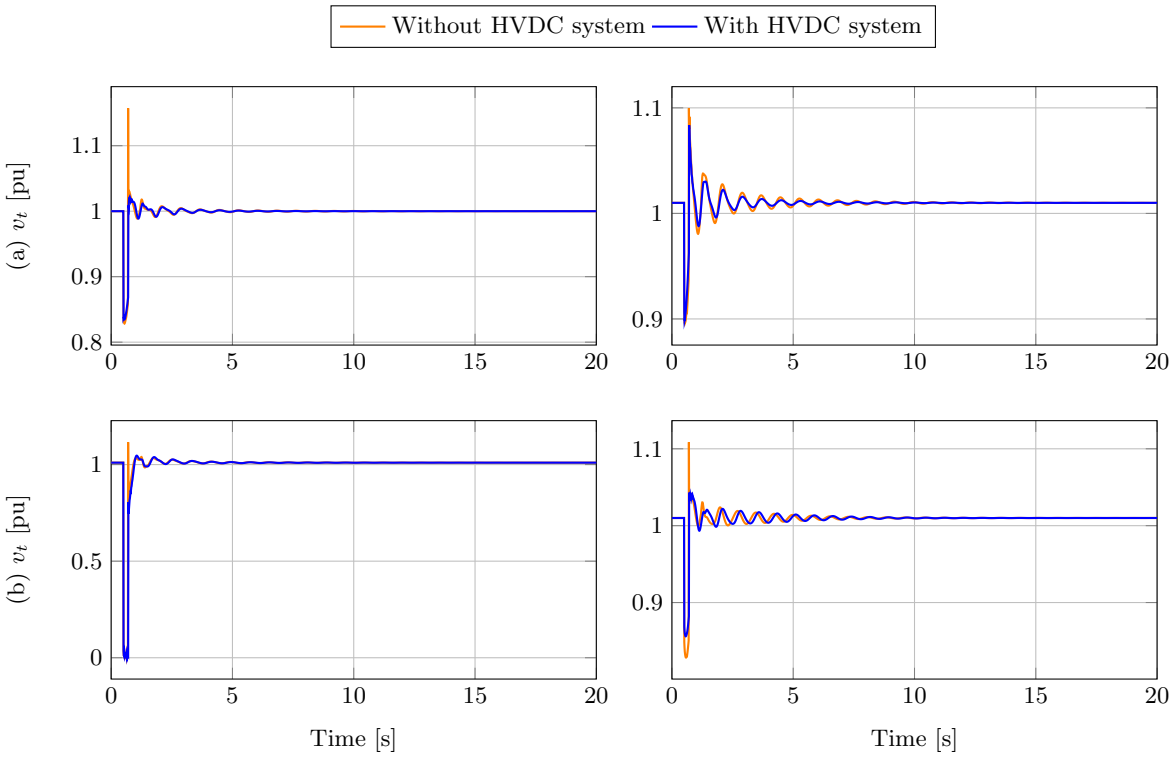

Figure 5.23: Dynamic responses of the voltage profiles of the generators when the HVDC system is considered for fault #1: (a) $\Delta\omega$ of the G1 (left) and G2 (right) and (b) $\Delta\omega$ of the G3 (left) and G4 (right).

5.6 Summary of the Chapter

This chapter analyzed the application of the passivity–based controllers for enhancing the dynamic responses in a power system with high–level penetration of PV plants. As indicated, the proposed decentralized control for HTGS based on the IDA–PBC improved the dynamic responses in the test system compared with standard controllers usually implemented. In addition, the power system oscillations were studied for three different penetration levels of PV plants were studied for enhancing POD by using the PV plants. Four cases to test the impact of the P–POD and Q–POD for the SMES system in the power system oscillations were also considered. It was noted that the SMES system is the one that contributes most to the improvement of the POD in the power system stability. Lastly, an analysis of how affects the inclusion of an HVDC system in the power system was realized.

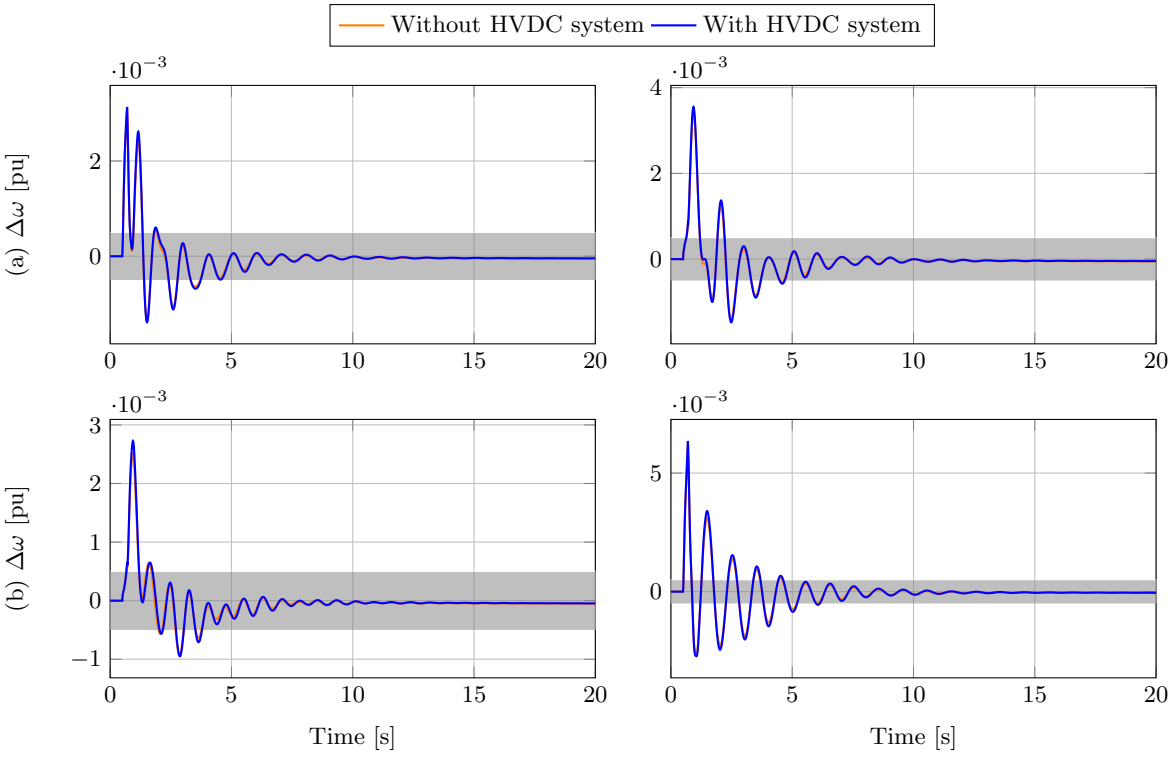

Figure 5.24: Dynamic responses of the rotor speed deviations when the HVDC system is considered for fault #2: (a) $\Delta\omega$ of the G1 (left) and G2 (right) and (b) $\Delta\omega$ of the G3 (left) and G4 (right).

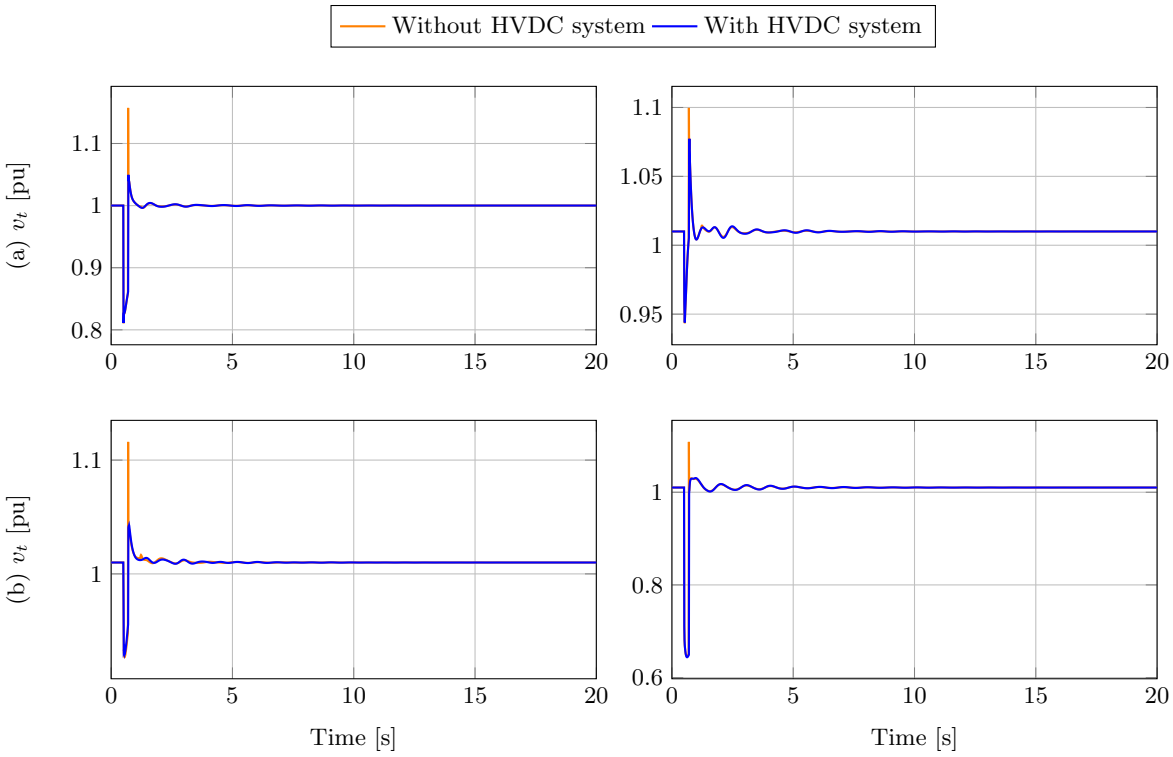

Figure 5.25: Dynamic responses of the voltage profiles of the generators when the HVDC system is considered for fault #2: (a) $\Delta\omega$ of the G1 (left) and G2 (right) and (b) $\Delta\omega$ of the G3 (left) and G4 (right).

Chapter 6

Conclusions

This chapter summarizes the main results of this dissertation and provides recommendations for future work.

6.1 Main Results

Below, the conclusions about the main problems addressed in this dissertation are presented.

- This dissertation accomplished a thorough review of the literature that focus on controllers for HTGS, PV plants, SMES systems, and VSC–HVDC systems, applied to improve the dynamic response of the power system during transients. In addition, the passivity-based control theory in the Hamiltonian structure for HTGS, the PV plants, the SMES system, and VSC–HVDC systems was also presented. Lastly, a summary of investigations related to controllers for small–hydro power plant was also shown.

- This dissertation proposed an adaptive IDA–PBC to control synchronous machines including HTGS with surge tank in multimachine power systems. The aims of the proposed controller were to stabilize the rotor speed and regulate the terminal voltage of each synchronous machine in the power system under test. The main advantage of the proposed controller was that is decentralized, thus, avoiding all problems of communication among the generators. Additionally, it keeps the passive structure in closed–loop guaranteeing its asymptotic stability based on Lyapunov's theory.

- A PI–PBC to control non–affine systems generated by VSCs, such as for the PV plants, the SMES system and two–terminal HVDC system was developed in this dissertation. Because of this, these models exhibited a pH structure in open loop, thus, the PI–PBC takes advantage of this structure to design a classical PI controller guaranteeing global asymptotic stability in closed–loop using Lyapunov's theory. In addition, the controller was robust even with parametric uncertainties and unmodeled dynamics, and is also decentralized.

- A direct power model for PV plants has been developed in this dissertation. The direct power model allowed managing the instantaneous active and reactive powers directly of each PV plant without using inner-loop current regulators. This model avoids the use of a PLL (no time delay), increasing the reliability of the system, and reducing the investment costs in electronic devices. In addition, a methodology to improve the damping of the power oscillation by controlling the active power of each PV plant was also presented. This methodology used a washout–filter and gain with a single input signal; thus it contains the basic components of the primary frequency being able to harmoniously interact with the grid, improving its controllability and stability. Lastly, the radiation did not show any effect in dynamic responses of the system. This was due to the fast natural response of converters and the proposed controllers.

- A study considering three different penetration levels of PV plants was made, in order to determine their impact on the power system oscillations. This study showed that as the penetration levels in the power system increasing, power oscillations were lower. This is due to that increasing distributed generation entails that transmission lines are available to withstand large power changes. Additionally, it was also observed that the proposed methodology worked as an additional inertia for the power system, since it contributes to damper the rate of change of the frequency, and therefore, its maximum deviation. This can be verified by comparing ITAEWs for all these scenarios when the proposed methodology is implemented and when it is not. Additionally, when the PV systems increase their penetration, the decrease in the frequency deviation becomes evident.

- A model to control the instantaneous active and reactive powers directly of the SMES system was described. This model has the same advantages of applied to PV plants. In addition, a methodology to compute active and reactive power reference focused on enhancing the dynamic response in the power system was proposed. Four cases to assess the impact of the proposed methodology for the SMES system in the power system oscillations were also studied. Here, it was observed that the SMES system contributes the most to the improvement of the POD in the power system stability. This is because is only dedicated to make this function.

- A DPC model for interconnecting a two–terminal VSC–HVDC system to an electrical network was presented. The DPC model allowed the control of the instantaneous active and reactive powers directly without employing the inner–loop current regulators. The controller for the VSC–HVDC system modeled as DPC model, was designed via PI–PBC since the system presents a pH structure in open–loop. Four scenarios were studied to demonstrate the performance of the proposed controller. A comparison with a conventional PI controller based on the DPC model and the POAPC controller was also presented. Simulation results showed that PI–PBC had a better regulation for dc–link voltage and active power and reactive power under different operating conditions than the PI and POAPC controllers. The proposed controller continued to show better performance even with uncertainties of the resistance and inductance in the system. Additionally, the effect of a two–terminal VSC–HVDC system in the power system stability during and after large disturbances was studied. It was noted that

it affect in power system depended on the operation point and the location of disturbances in the power system.

- The most significant improvement in the dynamic responses of the power system were achieved when the IDA–PBC method was implemented and the SMES system was considered. This entails two aspects; First, the power system presents a better performance when the controller for electromechanics systems are improved. Second, the SMES system can improve the performance of power system without the applied controller. This indicates that it is more important the devices and the proposed methodology to improve the performance of power system under and after large disturbances that the controller implemented.

6.2 Future Research

Next, some possible research topics about power system stability and control are suggested for future research projects.

- Extend passivity-based control theory for controlling another hydro–turbine models as well as steam–turbine models. In addition, motivated by practical considerations of models is necessary to implement state estimators to make the controller more robust, for example, the partial state feedback version of the controller that is derived by applying the immersion and invariance technique reported in (Astolfi et al., 2007), which guarantees asymptotic stability Lyapunov's theorem.

- Study another energy storage system for improving the dynamic response in the power system during and after large disturbances. Also, to use other methodologies to calculate active and reactive power references such inertial support, virtual synchronous machines, among other.

- Analyze the proposed controller and methodology in weak grids since the adverse impact of the PLL on the small–signal and transient stability used on VSC may deteriorate the stability of power system by introducing the negative incremental resistance at low frequencies. While the direct power model shown in this dissertation avoids implementing the PLL and all its problems.

- Finally, experimental work will be included in future activities to demonstrate the proposed controllers. To this end, a Power System Analyzer (PA3000 from Tektronix®) and a Hardware-in-the-Loop system (microlab box with DS1202 from dSAPACE), among others, will be used.

Bibliography

Abi-Samra, N., Smith, R., McDermott, T., and Chidester, M. (1985). Analysis of thyristor–controlled shunt SSR countermeasures. *IEEE Trans Power App Syst*, (3):583–597.

Adamczyk, A., Altin, M., Göksu, Ö., Teodorescu, R., and Iov, F. (2013). Generic 12–bus test system for wind power integration studies. In *Power Electronics and Applications (EPE), 2013 15th European Conference on*, pages 1–6. IEEE.

Ali, M., Wu, B., and Dougal, R. (2010). An overview of SMES applications in power and energy systems. *IEEE Trans. Sustainable Energy*, 1(1):38–47.

Ali, M. H., Murata, T., and Tamura, J. (2007). A fuzzy logic–controlled superconducting magnetic energy storage for transient stability augmentation. *IEEE Trans. Control Syst. Technol.*, 15(1):144–150.

Ali, M. H., Murata, T., and Tamura, J. (2008). Transient stability enhancement by fuzzy logic–controlled SMES considering coordination with optimal reclosing of circuit breakers. *IEEE Trans. Power Syst.*, 23(2):631–640.

Aly, M. M., Abdel-Akher, M., Said, S. M., and Senjyu, T. (2016). A developed control strategy for mitigating wind power generation transients using superconducting magnetic energy storage with reactive power support. *Int. J. Electr. Power Energy Syst.*, 83:485–494.

Anderson, P. M. and Fouad, A. (2003). *Power System Control and Stability*. Wiley–IEEE Press; 2, 2st edition.

Aranovskiy, S., Ortega, R., and Cisneros, R. (2016). A robust PI passivity–based control of nonlinear systems and its application to temperature regulation. *Int. J. Robust Nonlinear Control*, 26(10):2216–2231.

Astolfi, A., Karagiannis, D., and Ortega, R. (2007). *Nonlinear and adaptive control with applications*. Springer Science & Business Media.

Babunski, D. and Tuneski, A. (2003). Modelling and design of hydraulic turbine–governor system. In *3rd IFAC Workshop on Automatic Systems for Building the Infrastructure in Developing Countries 2003, Istanbul, Turkey*, volume 36, pages 263–267.

Barbero, J. (2013). La infraestructura en el desarrollo integral de américa latina. *Francia*, 167(143):23.

Baroudi, J. A., Dinavahi, V., and Knight, A. M. (2007). A review of power converter topologies for wind generators. *Renew Energy*, 32(14):2369–2385.

Beccuti, G., Papafotiou, G., and Harnefors, L. (2014). Multivariable optimal control of HVDC transmission links with network parameter estimation for weak grids. *IEEE Trans. Control Syst. Technol.*, 22(2):676–689.

Beerten, J., Cole, S., and Belmans, R. (2014). Modeling of multi–terminal VSC–HVDC systems with distributed DC voltage control. *IEEE Trans. Power Syst*, 29(1):34–42.

Bergna-Diaz, G., Zonetti, D., Sanchez, S., Ortega, R., and Tedeschi, E. (2018). PI Passivity–based Control and Performance Analysis of MMC Multi-Terminal HVDC Systems. *IEEE J. Emerg. Sel. Top. Power Electron.*, pages 1–1.

Bevrani, H., Ise, T., and Miura, Y. (2014). Virtual synchronous generators: A survey and new perspectives. *Int. J. Electr. Power Energy Syst.*, 54:244–254.

Bongiorno, M., Angquist, L., and Svensson, J. (2008). A novel control strategy for subsynchronous resonance mitigation using SSSC. *IEEE Trans. Power Del.*, 23(2):1033–1041.

Borkowski, D. (2017). Average-value model of energy conversion system consisting of PMSG, diode bridge rectifier and DPC–SVM controlled inverter. In *Electrical Machines (SME), 2017 International Symposium on*, pages 1–6. IEEE.

Borkowski, D. (2018). Analytical model of small hydropower plant working at variable speed. *IEEE Transactions on Energy Conversion*, 33(4):1886–1894.

Borkowski, D. and Wegiel, T. (2013). Small hydropower plant with integrated turbine–generators working at variable speed. *IEEE Transactions on Energy Conversion*, 28(2):452–459.

Breeze, P. (2016). *Solar Power Generation*. Academic Press.

Cerman, O. and Hušek, P. (2012). Adaptive fuzzy sliding mode control for electro–hydraulic servo mechanism. *Expert Syst. Appl.*, 39(11):10269–10277.

Chaiyatham, T. and Ngamroo, I. (2017). Improvement of Power System Transient Stability by PV Farm With Fuzzy Gain Scheduling of PID Controller. *IEEE Systems Journal*, 11(3):1684–1691.

Chaudhuri, N., Chaudhuri, B., Majumder, R., and Yazdani, A. (2014). *Multi–terminal direct–current grids: Modeling, analysis, and control*. John Wiley & Sons.

Chen, D., Ding, C., Do, Y., Ma, X., Zhao, H., and Wang, Y. (2014). Nonlinear dynamic analysis for a Francis hydro–turbine governing system and its control. *J. Franklin Inst.*, 351(9):4596–4618.

Chen, D., Ding, C., Ma, X., Yuan, P., and Ba, D. (2013). Nonlinear dynamical analysis of hydro–turbine governing system with a surge tank. *Appl. Math. Modell.*, 37(14):7611–7623.

Cisneros, R., Pirro, M., Bergna, G., Ortega, R., Ippoliti, G., and Molinas, M. (2015). Global tracking passivity–based PI control of bilinear systems: Application to the interleaved boost and modular multilevel converters. *Control Eng. Pract.*, 43:109–119.

Corbetta, G., Ho, A., Pineda, I., Ruby, K., Van de Velde, L., and Bickley, J. (2015). Wind energy scenarios for 2030. *European Wind Energy Association (EWEA), Brussels, Belgium, Technical Report*.

CREG–Comisión de Regulación de Energía y Gas. (2000). Resolución CREG–23 de 2000.

CREG–Comisión de Regulación de Energía y Gas. (2017). Resolución 121 de 2017.

Delille, G., Francois, B., and Malarange, G. (2012). Dynamic frequency control support by energy storage to reduce the impact of wind and solar generation on isolated power system's inertia. *IEEE Trans. Sustain. Energy*, 3(4):931–939.

Dong, D., Wen, B., Boroyevich, D., Mattavelli, P., and Xue, Y. (2015). Analysis of phase–locked loop low–frequency stability in three–phase grid–connected power converters considering impedance interactions. *IEEE Trans. Ind. Electron.*, 62(1):310–321.

Edrah, M., Lo, K., and Anaya-Lara, O. (2015). Impacts of high penetration of DFIG wind turbines on rotor angle stability of power systems. *IEEE Trans. Sustain. Energy*, 6(3):759–766.

El Heraldo (2014). Apagón en parte de barranquilla y soledad. https://www.elheraldo.co/local/apagon--en--el--norte--de--barranquilla--y--parte--de--soledad--151417. [Web; accessed el 04–11–2017].

Energy, I. (2016). Medium term market report. *International Energy Agency: Paris, France*.

Esram, T. and Chapman, P. L. (2007). Comparison of photovoltaic array maximum power point tracking techniques. *IEEE Trans Energy Convers*, 22(2):439–449.

Fang, H., Chen, L., Dlakavu, N., and Shen, Z. (2008). Basic modeling and simulation tool for analysis of hydraulic transients in hydroelectric power plants. *IEEE Transactions on energy conversion*, 23(3):834–841.

Fang, H., Chen, L., and Shen, Z. (2011). Application of an improved PSO algorithm to optimal tuning of PID gains for water turbine governor. *Energy Conversion and Management*, 52(4):1763–1770.

Farahani, M. (2012). A new control strategy of SMES for mitigating subsynchronous oscillations. *Physica C*, 483:34–39.

Farahani, M. and Ganjefar, S. (2013). A self–constructing wavelet neural network controller to mitigate the subsynchronous oscillations. *J. Dyn. Syst. Meas. Contr.*, 135(2):1–8.

Fiaz, S., Zonetti, D., Ortega, R., Scherpen, J. M., and v der Schaft, A. (2012). On port–hamiltonian modeling of the synchronous generator and ultimate boundedness of its solutions. *IFAC Proceed. Volumes*, 45(19):30–35.

Freijedo, F. D., Doval-Gandoy, J., Lopez, O., and Acha, E. (2009). Tuning of phase–locked loops for power converters under distorted utility conditions. *IEEE Transactions on Industry Applications*, 45(6):2039–2047.

Fuchs, A., Imhof, M., Demiray, T., and Morari, M. (2014). Stabilization of large power systems using VSC–HVDC and model predictive control. *IEEE Trans. Power Del.*, 29(1):480–488.

Giddani, O., Abbas, A. Y., Adam, G. P., Anaya-Lara, O., and Lo, K. L. (2013). Multi–task control for VSC–HVDC power and frequency control. *Int. J. Electr. Power Energy Syst.*, 53:684–690.

Gil-González, W., Garces, A., and Escobar, A. (2019). Passivity–based control and stability analysis for hydro–turbine governing systems. *Appl. Math. Modell.*, 68:471–486.

Gil-González, W. and Montoya, O. D. (2018). Passivity-based PI control of a SMES system to support power in electrical grids: A bilinear approach. *J. Energy Storage*, 18:459–466.

Gil-González, W., Montoya, O. D., and Garces, A. (2018). Control of a SMES for mitigating subsynchronous oscillations in power systems: A PBC–PI approach. *J. Energy Storage*, 20:163–172.

Gil-González, W., Garces, A., Escobar-Mejía, A., and Montoya, O. D. (2018). Passivity–based control for hydro–turbine governing systems. In *2018 IEEE PES Transmission Distribution Conference and Exhibition - Latin America (T D–LA)*, pages 1–5.

Giraldo, E. and Garces, A. (2014). An adaptive control strategy for a wind energy conversion system based on PWM-CSC and PMSG. *IEEE Transactions on power systems*, 29(3):1446–1453.

Golestan, S., Guerrero, J. M., and Vasquez, J. C. (2017). Three–phase PLLs: A review of recent advances. *IEEE Trans. Power Electron.*, 32(3):1894–1907.

Grbović, P. (2013). *Energy Storage Technologies and Devices*, pages 1–21. John Wiley & Sons, Ltd.

Guan, C. and Pan, S. (2008). Adaptive sliding mode control of electro–hydraulic system with nonlinear unknown parameters. *Control Eng. Pract.*, 16(11):1275–1284.

Gui, Y., Kim, C., Chung, C. C., Guerrero, J. M., Guan, Y., and Vasquez, J. C. (2018). Improved direct power control for grid-connected voltage source converters. *IEEE Trans. Ind. Electron.*

Guo, W., Yang, J., and Teng, Y. (2017). Surge wave characteristics for hydropower station with upstream series double surge tanks in load rejection transient. *Renew Energy*, 108:488–501.

Guo, W., Yang, J., Wang, M., and Lai, X. (2015). Nonlinear modeling and stability analysis of hydro-turbine governing system with sloping ceiling tailrace tunnel under load disturbance. *Energy Conversion and Management*, 106:127–138.

Hammad, A. and El-Sadek, M. (1984). Application of a thyristor controlled var compensator for damping subsynchronous oscillations in power systems. *IEEE Trans Power App Syst*, (1):198–212.

Haruni, A. O., Negnevitsky, M., Haque, M. E., and Gargoom, A. (2013). A novel operation and control strategy for a standalone hybrid renewable power system. *IEEE Trans Sustain Energy*, 4(2):402–413.

Hemeida, M. G., Rezk, H., and Hamada, M. M. (2018). A comprehensive comparison of STATCOM versus SVC-based fuzzy controller for stability improvement of wind farm connected to multi-machine power system. *Electrical Engineering*, 100(2):935–951.

Hernandez-Gomez, M., Ortega, R., Lamnabhi-Lagarrigue, F., and Escobar, G. (2010). Adaptive PI stabilization of switched power converters. *IEEE Trans. Control Syst. Technol.*, 18(3):688–698.

Huerta, H., Loukianov, A., and Cañedo, J. (2018). Passivity sliding mode control of large–scale power systems. *IEEE Trans. Control Syst. Technol.*, (99):1–9.

Ibrahim, H., Ilinca, A., and Perron, J. (2008). Energy storage systems—characteristics and comparisons. *Renew. Sustain. Energy Rev.*, 12(5):1221–1250.

IEEE working group report (1992). Hydraulic turbine and turbine control models for system dynamic studies. *IEEE Trans. Power Syst.*, 7(1):167–179.

Jiang, C., Ma, Y., and Wang, C. (2006). PID controller parameters optimization of hydro–turbine governing systems using deterministic–chaotic–mutation evolutionary programming (DCMEP). *Energy Convers. Manage.*, 47(9):1222–1230.

Jiang, J. (1995a). Design of an optimal robust governor for hydraulic turbine generating units. *IEEE Trans. Energy Convers.*, 10(1):188–194.

Jiang, J. (1995b). Design of an optimal robust governor for hydraulic turbine generating units. *IEEE Trans. Energy Convers.*, 10(1):188–194.

Jones, D. and Mansoor, S. (2004). Predictive feedforward control for a hydroelectric plant. *IEEE transactions on control systems technology*, 12(6):956–965.

Kanchanaharuthai, A., Chankong, V., and Loparo, K. (2015). Nonlinear generator excitation and superconducting magnetic energy storage control for transient stability enhancement via immersion and invariance. *Trans. Inst. Meas. Control*, 37(10):1217–1231.

Khalil, H. (2002). *Nonlinear Systems*. Prentice–Hall, New Jersey, 3rd edition.

Khodabakhshian, A. and Hooshmand, R. (2010). A new PID controller design for automatic generation control of hydro power systems. *Int. J. Electr. Power Energy Syst.*, 32(5):375–382.

Khooban, M. H., Niknam, T., and Sha-Sadeghi, M. (2016). A time–varying general type–II fuzzy sliding mode controller for a class of nonlinear power systems. *J. Intell. Fuzzy Syst.*, 30(5):2927–2937.

Kiaei, I. and Lotfifard, S. (2017). Tube–based model predictive control of energy storage systems for enhancing transient stability of power systems. *IEEE Trans. Smart Grid*, PP(99):1–1.

Kishor, N. and Singh, S. (2007). Simulated response of NN based identification and predictive control of hydro plant. *Expert Syst. Appl.*, 32(1):233–244.

Korai, A. and Erlich, I. (2015). Frequency dependent voltage control by DER units to improve power system frequency stability. In *PowerTech, 2015 IEEE Eindhoven*, pages 1–6. IEEE.

Lee, D. (2016). IEEE recommended practice for excitation system models for power system stability studies – redline. *IEEE Std 421.5–2016 (Revision of IEEE Std 421.5–2005) – Redline*, pages 1–453.

Leon, A., Solsona, J., and Valla, M. (2012a). Comparison among nonlinear excitation control strategies used for damping power system oscillations. *Energy Convers. Manage.*, 53(1):55–67.

Leon, A., Solsona, J., and Valla, M. I. (2012b). Comparison among nonlinear excitation control strategies used for damping power system oscillations. *Energy Convers. Manage.*, 53(1):55–67.

Leon, A. E., Mauricio, J. M., Solsona, J. A., and Gomez-Exposito, A. (2010). Adaptive control strategy for VSC–based systems under unbalanced network conditions. *IEEE Trans. Smart Grid*, 1(3):311–319.

Li, C., Mao, Y., Zhou, J., Zhang, N., and An, X. (2017a). Design of a fuzzy–PID controller for a nonlinear hydraulic turbine governing system by using a novel gravitational search algorithm based on Cauchy mutation and mass weighting. *Applied Soft Computing*, 52:290–305.

Li, H., Chen, D., Zhang, H., Wu, C., and Wang, X. (2017b). Hamiltonian analysis of a hydro–energy generation system in the transient of sudden load increasing. *Appl. Energy*, 185, Part 1:244–253.

Li, S., Haskew, T. A., and Xu, L. (2010). Control of HVDC light system using conventional and direct current vector control approaches. *IEEE Trans. Power Electron.*, 25(12):3106–3118.

Li, X., Hui, D., and Lai, X. (2013). Battery energy storage station (BESS)–based smoothing control of photovoltaic (PV) and wind power generation fluctuations. *IEEE Trans. Sustain. Energy*, 4(2):464–473.

Liang, J., Yuan, X., Yuan, Y., Chen, Z., and Li, Y. (2017). Nonlinear dynamic analysis and robust controller design for Francis hydraulic turbine regulating system with a straight–tube surge tank. *Mech. Syst. Sig. Process.*, 85(Supplement C):927–946.

Liao, S., Yao, W., Han, X., Wen, J., and Cheng, S. (2017). Chronological operation simulation framework for regional power system under high penetration of renewable energy using meteorological data. *Appl. Energy*, 203:816–828.

Lin, X. and Lei, Y. (2017). Coordinated Control Strategies for SMES–Battery Hybrid Energy Storage Systems. *IEEE Access*, 5:23452–23465.

Ling, D. and Tao, Y. (2006a). An analysis of the hopf bifurcation in a hydroturbine governing system with saturation. *IEEE Trans. Energy Convers.*, 21(2):512–515.

Ling, D. and Tao, Y. (2006b). An analysis of the hopf bifurcation in a hydroturbine governing system with saturation. *IEEE Trans. Energy Convers.*, 21(2):512–515.

Liu, F., Mei, S., Xia, D., Ma, Y., Jiang, X., and Lu, Q. (2004). Experimental evaluation of nonlinear robust control for SMES to improve the transient stability of power systems. *IEEE Trans. Energy Convers.*, 19(4):774–782.

Liu, S., Zhang, Y., Li, L., Hu, J., Zhou, Y., Zhao, W., and Xu, R. (2015). 220GHz band–pass filter based on circular resonance cavities with low loss. In *Microwave Conference (EuMC), 2015 European*, pages 1077–1079. IEEE.

Liu, Y., Lan, Q., Qian, C., Qian, W., and Chu, H. (2016). Universal finite–time observer design and adaptive frequency regulation of hydraulic turbine systems. *IET Control Theory Appl.*, 10(4):363–370.

Loukianov, A. G., Huerta, H., Utkin, V., and Cañedo, J. M. (2009). Nonlinear passivity robust decentralized controller for large scale power system. *IFAC Proceed. Volumes*, 42(4):474–479.

Luongo, C. A., Baldwin, T., Ribeiro, P., and Weber, C. M. (2003). A 100 MJ SMES demonstration at FSU-CAPS. *IEEE Transactions on Applied Superconductivity*, 13(2):1800–1805.

Ma, C., Liu, C., Zhang, X., Sun, Y., Wu, W., and Xie, J. (2018). Fixed–time stability of the hydraulic turbine governing system. *Math Probl Eng*, 2018.

Machowski, J., Bialek, J. W., and Bumby, J. R. (2008). *Power system dynamics: Stability and Control*. John Wily & Sons, 2 edition.

Marquez, J., Molina, M., and Pacas, J. (2010). Dynamic modeling, simulation and control design of an advanced micro–hydro power plant for distributed generation applications. *International journal of hydrogen energy*, 35(11):5772–5777.

Meah, K. and Ula, A. S. (2010). A new simplified adaptive control scheme for multi-terminal HVDC transmission systems. *Int J Electr Power Energy Syst*, 32(4):243–253.

Miller, N., Clark, K., and Shao, M. (2011). Frequency responsive wind plant controls: Impacts on grid performance. In *Power and Energy Society General Meeting, 2011 IEEE*, pages 1–8. IEEE.

Mitani, Y., Murakami, Y., and Tsuji, K. (1987). Experimental study on stabilization of model power transmission system by using four quadrant active and reactive power control by SMES. *IEEE Trans. Magn.*, 23(2):541–544.

Mitani, Y., Tsuji, K., and Murakami, Y. (1988). Application of superconducting magnet energy storage to improve power system dynamic performance. *IEEE Trans. Power Syst.*, 3(4):1418–1425.

Mo, O., D'Arco, S., and Suul, J. (2017). Evaluation of virtual synchronous machines with dynamic or quasi–stationary machine models. *IEEE Trans. on Ind. Elec.*, 64(7):5952–5962.

Modirkhazeni, A., Almasi, O. N., and Khooban, M. H. (2016). Improved frequency dynamic in isolated hybrid power system using an intelligent method. *Int. J. Electr. Power Energy Syst.*, 78:225–238.

Moharana, A. and Dash, P. (2010). Input–output linearization and robust sliding–mode controller for the VSC–HVDC transmission link. *IEEE Trans. Power Del.*, 25(3):1952–1961.

Montoya, O. D., Garcés, A., and Serra, F. M. (2018). DERs integration in microgrids using VSCs via proportional feedback linearization control: Supercapacitors and distributed generators. *Journal of Energy Storage*, 16:250–258.

Mukerjee, R. and Lee, S. J. (2014). Detection of weak points and evaluation of their effect on generation performance in the 12–bus benchmark test system. In *2014 Australasian Universities Power Engineering Conference (AUPEC)*, pages 1–6.

Nageshrao, S., Lopes, G., Jeltsema, D., and Babuška, R. (2016). Port–Hamiltonian systems in adaptive and learning control: A survey. *IEEE Trans. Autom. Control*, 61(5):1223–1238.

Nagode, K. and Škrjanc, I. (2014). Modelling and internal fuzzy model power control of a francis water turbine. *Energies*, 7(2):874–889.

Natarajan, K. (2005). Robust PID controller design for hydroturbines. *IEEE Transactions on Energy Conversion*, 20(3):661–667.

Ngamroo, I. (2011). An optimization of robust SMES with specified structure H_∞ controller for power system stabilization considering superconducting magnetic coil size. *Energy Convers. Manage.*, 52(1):648–651.

Ngamroo, I. and Vachirasricirikul, S. (2012). Coordinated control of optimized SFCL and SMES for improvement of power system transient stability. *IEEE Trans. Appl. Supercond.*, 22(3):5600805–5600805.

Ngamroo, I. and Vachirasricirikul, S. (2013). Optimized SFCL and SMES units for multimachine transient stabilization based on kinetic energy control. *IEEE Trans. Appl. Supercond.*, 23(3):5000309–5000309.

Ortega, Á. and Milano, F. (2016). Generalized model of VSC–based energy storage systems for transient stability analysis. *IEEE Trans. Power Syst.*, 31(5):3369–3380.

Ortega, R., Perez, J. A. L., Nicklasson, P. J., and Sira-Ramirez, H. J. (2013). *Passivity–based control of Euler–Lagrange systems: mechanical, electrical and electromechanical applications*. Springer Science & Business Media.

Ortega, R., Schaft, A. J. V. D., Mareels, I., and Maschke, B. (2001). Putting energy back in control. *IEEE Control Syst.*, 21(2):18–33.

Ortega, R., van der Schaft, A., Maschke, B., and Escobar, G. (2002). Interconnection and damping assignment passivity–based control of port–controlled hamiltonian systems. *Automatica*, 38(4):585 – 596.

Padiyar, K. and Prabhu, N. (2006). Design and performance evaluation of subsynchronous damping controller with STATCOM. *IEEE Trans. Power Del.*, 21(3):1398–1405.

Pappachen, A. and Fathima, A. (2016). Load frequency control in deregulated power system integrated with SMES–TCPS combination using ANFIS controller. *Int. J. Electr. Power Energy Syst.*, 82:519–534.

Patil, K., Senthil, J., Jiang, J., and Mathur, R. (1998). Application of STATCOM for damping torsional oscillations in series compensated AC systems. *IEEE Trans. Energy Convers.*, 13(3):237–243.

Perko, L. (2013). *Differential equations and dynamical systems*, volume 7. Springer Science & Business Media.

Pico, H. V., McCalley, J. D., Angel, A., Leon, R., and Castrillon, N. J. (2012). Analysis of very low frequency oscillations in hydro–dominant power systems using multi–unit modeling. *IEEE Trans. Power Syst.*, 27(4):1906–1915.

Pourbeik, P. et al. (2013). Dynamic models for turbine-governors in power system studies. *IEEE Task Force on Turbine-Governor Modeling*, (2013).

Rabbani, M., Devotta, J., and Elangovan, S. (1998). An efficient fuzzy controlled system for superconducting magnetic energy storage unit. *Int. J. Electr. Power Energy Syst.*, 20(3):197 – 202.

Rabbani, M., Devotta, J., and Elangovan, S. (1999). Multi–mode wide range subsynchronous resonance stabilization using superconducting magnetic energy storage unit. *Int. J. Electr. Power Energy Syst.*, 21(1):45–53.

Rahim, A., Mohammad, A., and Khan, M. (1996). Control of subsynchronous resonant modes in a series compensated system through superconducting magnetic energy storage units. *IEEE Trans. Energy Convers.*, 11(1):175–180.

Rahim, A. and Nowicki, E. (2005). A robust damping controller for SMES using loop–shaping technique. *Int. J. Electr. Power Energy Syst.*, 27(5):465–471.

Rajaram, T., Reddy, J. M., and Xu, Y. (2017). Kalman filter based detection and mitigation of subsynchronous resonance with SSSC. *IEEE Trans. Power Syst.*, 32(2):1400–1409.

Raju, D. K., Umre, B. S., Junghare, A. S., and Babu, B. C. (2017). Mitigation of subsynchronous resonance with fractional-order PI based UPFC controller. *Mech. Syst. Sig. Process.*, 85:698–715.

Ramadan, H. S., Siguerdidjane, H., Petit, M., and Kaczmarek, R. (2012). Performance enhancement and robustness assessment of VSC–HVDC transmission systems controllers under uncertainties. *Int. J. Electr. Power Energy Syst.*, 35(1):34–46.

Ramli, M. A., Twaha, S., Ishaque, K., and Al-Turki, Y. A. (2017). A review on maximum power point tracking for photovoltaic systems with and without shading conditions. *Renew. Sustain. Energy Rev.*, 67:144–159.

Remon, D., Cañizares, C., and Rodriguez, P. (2017a). Impact of 100–MW–scale PV plants with synchronous power controllers on power system stability in northern Chile. *IET Gener. Transm. Distrib.*, 11(11):2958–2964.

Remon, D., Cañizares, C. A., and Rodriguez, P. (2017b). Impact of 100–MW–scale PV plants with synchronous power controllers on power system stability in northern Chile. *IET Generation, Transmission & Distribution*, 11(11):2958–2964.

Remon, D., Cantarellas, A. M., Martinez-Garcia, J., Escaño, J. M., and Rodriguez, P. (2017). Hybrid solar plant with synchronous power controllers contribution to power system stability. In *2017 IEEE Energy Conversion Congress and Exposition (ECCE)*, pages 4069–4076.

Remon, D., Cantarellas, A. M., Mauricio, J. M., and Rodriguez, P. (2017). Power system stability analysis under increasing penetration of photovoltaic power plants with synchronous power controllers. *IET Renewable Power Gener.*, 11(6):733–741.

Rodriguez, J., Fernandez, J., Beato, D., Iturbe, R., Usaola, J., Ledesma, P., and Wilhelmi, J. (2002). Incidence on power system dynamics of high penetration of fixed speed and doubly fed wind energy systems: study of the spanish case. *IEEE Trans. Power Syst.*, 17(4):1089–1095.

Ruan, S.-Y., Li, G.-J., Peng, L., Sun, Y.-Z., and Lie, T. (2007). A nonlinear control for enhancing HVDC light transmission system stability. *Int. J. Electr. Power Energy Syst.*, 29(7):565–570.

Sadeghi, M. S., Vafamand, N., and Khooban, M. H. (2016). LMI–based stability analysis and robust controller design for a class of nonlinear chaotic power systems. *J. Franklin Institute*, 353(13):2835–2858.

Sadeghzadeh, S., Ehsan, M., Said, N., and Feuillet, R. (1999). Transient stability improvement of multi–machine power systems using on–line fuzzy control of SMES. *Control Eng. Pract.*, 7(4):531–536.

Sadeghzadeh, S. M., Ehsan, M., Said, N. H., and Feuillet, R. (1998). Improvement of transient stability limit in power system transmission lines using fuzzy control of FACTS devices. *IEEE Trans. Power Syst.*, 13(3):917–922.

Sanathanan, C. (1987). Accurate low order model for hydraulic turbine–penstock. *IEEE Trans. Energy Convers.*, (2):196–200.

Schmuck, C., Woittennek, F., Gensior, A., and Rudolph, J. (2014). Feed–forward control of an HVDC power transmission network. *IEEE Trans. Control Syst. Technol.*, 22(2):597–606.

Sedighizadeh, M., Esmaili, M., and Parvaneh, H. (2018). Coordinated optimization and control of SFCL and SMES for mitigation of SSR using HBB–BC algorithm in a fuzzy framework. *J. Energy Storage*, 18:498–508.

Shah, R., Mithulananthan, N., and Lee, K. (2013). Large–scale PV plant with a robust controller considering power oscillation damping. *IEEE Trans. Energy Convers.*, 28(1):106–116.

Shi, J., Tang, Y., Dai, T., Ren, L., Li, J., and Cheng, S. (2010). Determination of SMES capacity to enhance the dynamic stability of power system. *Physica C*, 470(20):1707–1710. Proceedings of the 22nd International Symposium on Superconductivity (ISS 2009).

Shi, J., Tang, Y., Xia, Y., Ren, L., Li, J., and Jiao, F. (2012). Energy function based SMES controller for transient stability enhancement. *IEEE Trans. Appl. Supercond.*, 22(3):5701304–5701304.

Shintai, T., Miura, Y., and Ise, T. (2014). Oscillation damping of a distributed generator using a virtual synchronous generator. *IEEE Trans Power Del*, 29(2):668–676.

Simani, S., Alvisi, S., and Venturini, M. (2016). Fault tolerant control of a simulated hydroelectric system. *Control Eng. Pract.*, 51:13–25.

SINAC, C. (2017). Mitigación del fenómeno de resonancia subsíncrona en el SEIN. http://www.coes.org.pe/Portal/MarcoNormativo/DecisionesEjecutivasNotasTecnicas. Accessed 2017–06–30.

Song, Z., Tian, Y., Yan, Z., and Chen, Z. (2016). Direct power control for three-phase two–level voltage-source rectifiers based on extended-state observation. *IEEE Trans. Ind. Electron.*, 63(7):4593–4603.

Surinkaew, T. and Ngamroo, I. (2017). Two–level coordinated controllers for robust inter–area oscillation damping considering impact of local latency. *IET Generation, Transmission & Distribution*, 11(18):4520–4530.

Surinkaew, T. and Ngamroo, I. (2018). Adaptive signal selection of wide–area damping controllers under various operating conditions. *IEEE Transactions on Industrial Informatics*, 14(2):639–651.

Surinkaew, T. and Ngamroo, I. (2019). Inter–area oscillation damping control design considering impact of variable latencies. *IEEE Trans. Power Syst.*, 34(1):481–493.

Suul, J., D'Arco, S., and Guidi, G. (2016). Virtual synchronous machine–based control of a single–phase bi–directional battery charger for providing vehicle–to–grid services. *IEEE Trans. Ind. Appl.*, 52(4):3234–3244.

Taguchi, A., Imayoshi, T., Nagafuchi, T., Akine, T., Yamada, N., and Hayashi, H. (2007). A study of SMES control logic for power system stabilization. *IEEE Trans. Appl. Supercond.*, 17(2):2343–2346.

Tamimi, B., Cañizares, C., and Bhattacharya, K. (2013). System stability impact of large–scale and distributed solar photovoltaic generation: The case of ontario, canada. *IEEE Trans Sustain Energy*, 4(3):680–688.

Tan, Y. and Wang, Y. (2004). A robust nonlinear excitation and SMES controller for transient stabilization. *Int. J. Electr. Power Energy Syst.*, 26(5):325–332.

Thirumalaivasan, R., Janaki, M., and Prabhu, N. (2013). Damping of SSR using subsynchronous current suppressor with SSSC. *IEEE Trans. Power Syst.*, 28(1):64–74.

Vahidnia, A., Ledwich, G., and Palmer, E. W. (2016). Transient Stability Improvement Through Wide-Area Controlled SVCs. *IEEE Transactions on Power Systems*, 31(4):3082–3089.

van der Schaft, A. (2017). *L2–gain and passivity techniques in nonlinear control*. Springer International Publishing AG, 3 edition.

Varma, R. K. and Salehi, R. (2017). SSR mitigation with a new control of PV solar farm as STATCOM (PV-STATCOM). *IEEE Trans. Sustainable Enery*, 8(4):1473–1483.

Vidyasagar, M. (2002). *Nonlinear systems analysis*. SIAM.

Wan, Y. and Zhao, J. (2013). h_∞ control of single–machine infinite bus power systems with superconducting magnetic energy storage based on energy–shaping and backstepping. *IET Control Theory Appl.*, 7(5):757–764.

Wang, H. and Du, W. (2016). *Analysis and damping control of power system low–frequency oscillations*. Springer.

Wang, L. and Tseng, H. (1999). Suppression of common–mode torsional oscillations of nonidentical turbine–generators using SMES. In *IEEE Power Engineering Society. 1999 Winter Meeting (Cat. No.99CH36233)*, volume 1, pages 117–122 vol.1.

Wang, M., Zhang, Y., Ji, T., and Wang, X. (2016). Grey prediction control and extension assessment for turbine governing system. *IET Generation, Transmission Distribution*, 10(11):2601–2605.

Wang, S., Lv, D., Li, Z., and Li, H. (2011). A novel rbf–pid control strategy for turbine governing system based on chaotic pso. In *2011 9th World Congress on Intelligent Control and Automation*, pages 130–135.

Wang, Y., Feng, G., Cheng, D., and Liu, Y. (2006). Adaptive l_2 disturbance attenuation control of multi–machine power systems with SMES units. *Automatica*, 42(7):1121 – 1132.

Wu, C. J. and Lee, Y. S. (1993). Application of simultaneous active and reactive power modulation of superconducting magnetic energy storage unit to damp turbine–generator subsynchronous oscillations. *IEEE Trans. Energy Convers.*, 8(1):63–70.

Xu, B., Wang, F., Chen, D., and Zhang, H. (2016a). Hamiltonian modeling of multi–hydro–turbine governing systems with sharing common penstock and dynamic analyses under shock load. *Energy Convers. Manage.*, 108:478–487.

Xu, C. and Qian, D. (2015). Governor design for a hydropower plant with an upstream surge tank by GA-based Fuzzy reduced-order sliding mode. *Energies*, 8(12):13442–13457.

Xu, T., Zhang, L., Zeng, Y., and Qian, J. (2012). Hamiltonian model of hydro turbine with sharing sommon conduit. In *2012 Asia–Pacific Power and Energy Engineering Conference*, pages 1–5.

Xu, Y., Zhou, J., Xue, X., Fu, W., Zhu, W., and Li, C. (2016b). An adaptively fast fuzzy fractional order PID control for pumped storage hydro unit using improved gravitational search algorithm. *Energy Convers. Manage.*, 111:67–78.

Xu, Y., Zhou, J., Zhang, Y., Fu, W., Zheng, Y., and Zhang, X. (2016c). Parameter optimization of robust non–fragile fractional order pid controller for pump turbine governing system. In *2016 Sixth International Conference on Instrumentation Measurement, Computer, Communication and Control (IMCCC)*, pages 15–18.

Yang, B., Jiang, L., Wang, L., Yao, W., and Wu, Q. (2016a). Nonlinear maximum power point tracking control and modal analysis of DFIG based wind turbine. *Int. J. Electr. Power Energy Syst.*, 74:429–436.

Yang, B., Jiang, L., Yao, W., and Wu, Q. (2017a). Perturbation observer based adaptive passive control for damping improvement of multi-terminal voltage source converter-based high voltage direct current systems. *Trans. Inst. Meas. Control*, 39(9):1409–1420.

Yang, B., Jiang, L., Yu, T., Shu, H., Zhang, C.-K., Yao, W., and Wu, Q. (2018a). Passive control design for multi-terminal VSC–HVDC systems via energy shaping. *Int. J. Electr. Power Energy Syst.*, 98:496–508.

Yang, B., Sang, Y., Shi, K., Yao, W., Jiang, L., and Yu, T. (2016b). Design and real–time implementation of perturbation observer based sliding-mode control for VSC–HVDC systems. *Control Eng. Pract.*, 56:13–26.

Yang, W., Zhang, A., Li, J., Li, G., Zhang, H., and Wang, J. (2017b). Integral plus resonant sliding mode direct power control for VSC-HVDC systems under unbalanced grid voltage conditions. *Energies*, 10(10):1528.

Yang, Y., Kim, K. A., Blaabjerg, F., and Sangwongwanich, A. (2018b). Advances in grid–connected photovoltaic power conversion systems.

Yuan, X., Chen, Z., Yuan, Y., Huang, Y., Li, X., and Li, W. (2016). Sliding mode controller of hydraulic generator regulating system based on the input/output feedback linearization method. *Mathematics and Computers in Simulation*, 119:18–34.

Zakeri, B. and Syri, S. (2015). Electrical energy storage systems: A comparative life cycle cost analysis. *Renew. Sustain. Energy Rev.*, 42:569–596.

Zargari, A., Hooshmand, R., and Ataei, M. (2012). A new control system design for a small hydro–power plant based on particle swarm optimization–fuzzy sliding mode controller with kalman estimator. *Trans. Inst. Meas. Control*, 34(4):388–400.

Zeng, Y., Zhang, L., Guo, Y., Qian, J., and Zhang, C. (2014). The generalized hamiltonian model for the shafting transient analysis of the hydro turbine generating sets. *Nonlinear Dyn.*, 76(4):1921–1933.

Zeng, Y., Zhang, L., Xu, T., and Dong, H. (2010). Improvement rotor angle oscillation of hydro turbine generating sets based on hamiltonian damping injecting method. In *Power and Energy Engineering Conference (APPEEC), 2010*, pages 1–5.

Zeni, L., Eriksson, R., Goumalatsos, S., Altin, M., Sørensen, P., Hansen, A., Kjær, P., and Hesselbæk, B. (2016). Power oscillation damping from vsc–hvdc connected offshore wind power plants. *IEEE Transactions on Power Delivery*, 31(2):829–838.

Zhang, G., Cheng, Y., Lu, N., and Guo, Q. (2016a). Research of Hydro–turbine Governor Supplementary Control Strategy for Islanding AC Grid at Sending Terminal of HVDC System. *IEEE Trans. Energy Convers.*, 31(4):1229–1238.

Zhang, H., Chen, D., Guo, P., Luo, X., and George, A. (2018a). A novel surface–cluster approach towards transient modeling of hydro-turbine governing systems in the start–up process. *Energy Convers. Manage.*, 165:861–868.

Zhang, H., Chen, D., Wu, C., and Wang, X. (2018b). Dynamics analysis of the fast–slow hydro–turbine governing system with different time–scale coupling. *Commun Nonlinear Sci Numer Simu*, 54:136–147.

Zhang, H., Chen, D., Wu, C., Wang, X., Lee, J., and Jung, K. (2017). Dynamic modeling and dynamical analysis of pump–turbines in s–shaped regions during runaway operation. *Energ Conver. Manag.*, 138:375–382.

Zhang, H., Chen, D., Xu, B., Patelli, E., and Tolo, S. (2018c). Dynamic analysis of a pumped–storage hydropower plant with random power load. *Mechanical Systems and Signal Processing*, 100:524–533.

Zhang, L., Harnefors, L., and Nee, H.-P. (2011). Interconnection of two very weak AC systems by VSC–HVDC links using power-synchronization control. *IEEE Trans Power Syst*, 26(1):344–355.

Zhang, R., Chen, D., and Ma, X. (2015). Nonlinear predictive control of a hydropower system model. *Entropy*, 17(9):6129–6149.

Zhang, W., Remon, D., and Rodriguez, P. (2016b). Frequency support characteristics of grid–interactive power converters based on the synchronous power controller. *IET Renewable Power Gener.*, 11(4):470–479.

Zheng, H., Jiang, D., Xu, F., and Yiqiao, L. (2015). Optimum configuration for AC/DC converters of DC distribution network. *Int. Trans. Electr. Energy Syst.*, 25(10):2058–2070.

Zhou, J., Zhang, Y., Zheng, Y., and Xu, Y. (2018). Synergetic governing controller design for the hydraulic turbine governing system with complex conduit system. *J. Frankl. Inst.*, 355(10):4131–4146.

Zhu, J., Zhang, H., Yuan, W., Zhang, M., and Lai, X. (2013). Design and cost estimation of superconducting magnetic energy storage (SMES) systems for power grids. In *2013 IEEE Power & Energy Society General Meeting*, pages 1–5. IEEE.

Zhu, W., Spee, R., Mohler, R., Alexander, G., Mittelstadt, W., and Maratukulam, D. (1995). An EMTP study of SSR mitigation using the thyristor controlled series capacitor. *IEEE Trans. Power Del.*, 10(3):1479–1485.

Zhu, W., Zheng, Y., Dai, J., and Zhou, J. (2017). Design of integrated synergetic controller for the excitation and governing system of hydraulic generator unit. *Eng. Appl. Artif. Intell.*, 58:79–87.

Zobaa, A., editor (2013). *Energy Storage–Technologies and Applications*. Rijeka:InTech.

Zonetti, D. (2016). *Energy–based modelling and control of electric power systems with guaranteed stability properties*. PhD thesis, Université Paris-Saclay.

Zonetti, D., Ortega, R., and Benchaib, A. (2015). Modeling and control of HVDC transmission systems from theory to practice and back. *Control Eng. Pract.*, 45:133–146.

Zou, J., Pipattanasomporn, M., Rahman, S., and Lai, X. (2016). A frequency regulation framework for hydro plants to mitigate wind penetration challenges. *IEEE Trans. Sustain. Energy*, 7(4):1583–1591.

Appendix A

Small Hydro–Power Plant

This Appendix shows a passivity-based control for a small hydro–power plant which consists of a permanent magnet synchronous generator connected to a three-phase grid through a back–to–back converter. The proposed controller is tested and compared with a conventional PI controller in a 13.2 kV distribution feeder. Simulation results demonstrate the advantages of the proposed methodology.

In this appendix is analyzed a controller for a small hydro–power (SHP) plant separately from the rest of the dissertation since its contribution in the operation of a power system is not significant. Since the SHP plants are of small capacity and they are designed to operate in distribution feeder or microgrids.

It is important to mention that the mathematical model for SHP plants is different that the model for HTGS plants since this does not have a synchronous machine but also a permanent magnet synchronous generator (PMSG), which is not connected directly to distribution system. The SHP plant iss connected to the grid through a *back–to–back* converter.

A.1 Small Hydro–Power Plant Model

The SHP plant considered in this dissertation consists of a hydro–turbine, a governor, a penstock, and a PMSG. The PMSG is connected to the grid through a *back–to–back* converter. The main function of the system of governor is to control the water flow of the hydraulic turbine and thus, control its speed or power output. Typically governor is modeled like a PID controller, which has been widely used (Chen et al., 2014; Ling and Tao, 2006b) to regulate rotor speed. The aim of this appendix is to model the governor of the SHP like a passivity-based controller. The hydraulic turbine model of the SHP is similar to the HTGS model described in section 3.1 with difference that is not considered the surge tank. Since pressure waves are small in the SHP, therefore, it is not to protect pipes and turbines from this phenomenon function that makes the surge tank. The

dynamic model of a hydraulic turbine is:

$$\begin{aligned} T_{W1}\dot{q}_1 &= 1 - h - k_{f1}q_1^2, \\ T_y\dot{y}_g &= u_y - y_g. \end{aligned} \tag{A.1}$$

This variables already defined in section 3.1.

A.1.1 Permanent Magnet Synchronous Generator

Fig. A.1 illustrates a PMSG integrated to the power grid with a back–to–back converter (Baroudi et al., 2007). The electrical and mechanical equations that describe the behavior of the dynamics in values per–unit of a PMSG are given by

$$\begin{aligned} L_g\dot{i}_{dg} &= -R_g i_{dg} + L_g\omega_m i_{qg} - v_d, \\ L_g\dot{i}_{qg} &= -R_g i_{qg} - L_g\omega_m i_{dg} + \psi\omega_{e_g} - v_q, \\ M\dot{\omega}_m &= T_m - T_e, \end{aligned} \tag{A.2}$$

with

$$M = \frac{2H_g}{\omega_o},$$

where v_{dq} and i_{dq_g} are the voltages and currents of PMSG in dq reference frame, respectively. R_g and L_g are the stator winding's resistance and inductance, respectively. ω_m is the rotor speed ($\omega_m = \omega_{e_g}$ in per–unit). ψ denotes permanent magnetic flux produced by the rotor magnets, which is constant and depends on the material used for its construction. H_g is hydro-turbine inertia time constant and ω_o is the generator based angular speed; T_m and T_e are the mechanical and electrical torque. Mechanical torque T_m was defined in (3.4) as

$$\tau_m = \frac{A_t q_1^2\,(q_1 - q_{nl})}{y_g^2\omega},$$

and the electrical torque is given by

$$T_e = \psi i_q.$$

Typically a back–to–back configuration with voltage source converters is employed to integrate a PMSG to the ac grid because this requires a full rated converter (Baroudi et al., 2007). Therefore, the output voltages of a PMSG can define as function of the modulation indexes of the converter as follows:

$$v_{dq} = m_{dq_g} v_{dc}$$

where $m_{dq_g} \in [-1, 1]$ represents the modulation index and subscript g refers to the VSC_g; v_{dc} is the voltage in the dc–link.

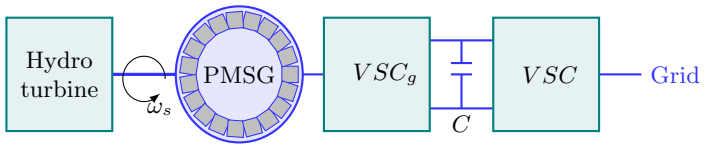

Figure A.1: A PMSG integrated to back–to–back converter

The configuration used presents the PMSG connected directly to a VSC, due to this, the PMSG output voltages are represented as modulation indexes by the voltage in the dc–link (for more details, see (Giraldo and Garces, 2014)).

The dynamic modeling of second VSC in the dq reference frame is given by

$$\begin{aligned} L\dot{i}_d &= -Ri_d - L\omega_e i_q + v_{dc}m_{d2} - e_d, \\ L\dot{i}_q &= -Ri_q + L\omega_e i_d + v_{dc}m_{q2} - e_q, \\ C\dot{v}_{dc} &= i_s - i_d m_d - i_q m_q, \end{aligned} \tag{A.3}$$

where i_{dq} is current that flow through of the transformer and, L and R are their inductance and resistance parameters, respectively. e_{dq} the ac voltage of the main grid; C is the dc–link capacitor of the VSC and its voltage is v_{dc} and i_s is the current delivered by the PMSG. ω_e is the grid angular electrical frequency, which is gotten employing a classical phase–locked loop (PLL) (Golestan et al., 2017). $m_{dq} \in [-1, 1]$ represents the modulation index of a VSC connected to ac grid.

A.2 Controller Design for the SHP Plant

The controller design for the SHP plant is done separately. The control design for hydro–turbine and PMSG (see (A.1) and (A.2)) are based on IDA–PBC described in section 2.5.1 since this system is affine; While the control design for the VSC (see (A.3)) is based on PI–PBC shown in section 2.5.2 since this system is non–affine.

A.3 Controller Design for the Hydro–Turbine and PMSG

The aims of control are to regulate turbine/rotor speed and the electrical power delivered by PMSG and its d–axis current. The control design is based on the IDA–PBC presented in Section 2.5.1. To apply this method, it is necessary to choose the desired total stored $H(\tilde{x}_{sh})_d$, the desired interconnection matrix J_{sh}, and the desired damping matrix R_{sh}. We choose $H(\tilde{x}_{sh})_d$ as the quadratic function:

$$H(\tilde{x}_{sh})_d = \frac{1}{2}(x_{sh} - x^*_{sh})^T \mathcal{P}_{sh}(x_{sh} - x^*_{sh}),$$

where $x_{sh} = \text{col}(x_1, ..., x_5) = \text{col}(q_1, y_g, i_{dg}, i_{qg}, \omega_m)$ and $\mathcal{P}_{sh} = \text{diag}(T_{W1}, T_{yi}, L_g, L_g, M)$.

Now, we fix the desired matrices R_{sh} and J_{dsh} as having a relation between the control aims and control variables, as follows:

$$R_{sh} = \text{diag}(r_{sh1}, ..., r_{sh5}),$$
$$J_{sh} = \begin{bmatrix} 0 & 0 & 0 & 0 & 0 \\ 0 & 0 & 0 & 0 & 0 \\ 0 & 0 & 0 & L_g x_5 & 0 \\ 0 & 0 & -L_g x_5 & 0 & -f \\ 0 & 0 & 0 & f & 0 \end{bmatrix}.$$

The control laws are found by applying (2.11), as follows

$$\begin{aligned} u_y &= x_{2^*} - r_{sh2}(x_2 - x_2^*), \\ m_{dg} &= -\frac{r_{sh3}(x_3 - x_3^*) + R_g x_3^* - L_g x_5 x_4^*}{v_{dc}}, \\ m_{qg} &= -\frac{r_{sh4}(x_4 - x_4^*) + R_g x_4^* + L_g x_5 x_3^* - \psi x_5^*}{v_{dc}}. \end{aligned} \tag{A.4}$$

Now, it is necessary to define the reference values. Typically, the control variables for the PMSG are rotor speed and d–axis current. x_5^* allows controlling the rotor speed, i.e., $x_5^* = \omega_m^{nom}$ and to guarantee the maximum torque $x_3^* = 0$. To control the electrical power delivered by PMSG, we use the following expression

$$x_2^* = \frac{A_t (x_1^*)^2 (x_1^* - q_{nl})}{P_m^*},$$

with,

$$P_m^* = P_e^* + |i_{dq}|^2 R_g,$$

where P_e^* is the reference electrical power.

To apply the control laws of (A.4), it is necessary to compute the non–controlled variables that can be found by defining the left annihilator of g_i as

$$g_i^{\perp} = \begin{bmatrix} 1 & 0 & 0 & 0 & 0 \\ 0 & 0 & 0 & 1 & 0 \end{bmatrix}^T,$$

and using (2.10), the non–controlled variables are:

$$\begin{aligned} x_4^* &= \frac{T_m + r_{sh5}(x_5 - x_5^*)}{\psi}, \\ x_1^* &= \frac{r_{sh1} x_1 - 1}{r_{sh1} - x_1 \left(k_{f1} + \dfrac{1}{x_2^2} \right)}. \end{aligned}$$

A.4 Controller Design for the VSC

The control aims for the VSC are to deliver all electrical power generated by the PMSG and regulate the dc–link voltage to guarantee its operating adequate. Applying (2.19) the passive outputs of the VSC are

$$\tilde{y} = \begin{bmatrix} x_8 x_6^* - x_6 x_8^* \\ x_8 x_7^* - x_7 x_8^* \end{bmatrix},$$

where $x_6 = i_d$, $x_7 = i_q$, and $x_8 = v_{dc}$.

Defining x_8 and x_7 as the control variables for the VSC. x_8^* is selected to control dc–link voltage on the capacitor C, i.e., $x_8^* = V_{dc}^{nom}$. In case of x_7^* permits to control the reactive power delivered (or absorbed) by VSC to the ac grid, which is calculated as

$$x_8^* = \frac{e_q P_e^* - e_q Q^*}{e_d^2 + e_q^2},$$

where Q^* is the reference reactive power and P_e^* is the active power delivered by PMSG.

The controller design is fulfilled when x_6^* is determined, which is computed similarly as shown in section , as follows

$$x_6^* = i_s - Kp_{sh}(x_8^* - x_8) - Ki_{sh}\int (x_8^* - x_8)dt.$$

A.5 Test system, Simulation Scenarios and Results for the SHP Plant

Fig. A.2 depicts the test system employed to assess the proposed controller. The test system was conducted in Matlab/Simulink SimPowerSystems. This test system is a modification of proposed in (Giraldo and Garces, 2014), which has a 13.2 kV distribution feeder with a 2–MW SHP and four loads. Parameters of the system and SHP have listed in in Appendix B Table B.13.

We proposed two simulation scenarios in order to investigate the effectiveness of the proposed control of the SHP, simulations were implemented using MATLAB/Simulink. For validation, the proposed controller is compared with a conventional PI controller. It is important to mention that when we refer to the PI controller for the SHP, it is divided as follows, the governor system is controlled with the PID controller and PMSG and VSC are controlled with PI controllers.

Scenario 1: Active and reactive power control. It presents the ability of the PBC to control the active and reactive output power of the SHP on the point of common coupling (PCC). Simulations illustrated in Fig. A.3 show the active power delivered by the hydro–power plant on dc–link and the rotor speed deviation.

Note in Fig. A.3(a) that response of both controllers present the intrinsic non–minimum phase characteristic of hydro–power plant. However, the PBC has a better response than PI controller with an average error about 5 %, while PI controller present an average error about 8.4 %. Rotor

speed regulation the proposed controller continues presenting a better than PI controller since this keeps an error about $1 \cdot 10^{-4}$ (see Fig. A.3(b)).

Fig. A.4 shows the active and reactive power deliver on PCC by the SHP and dc-link voltage. Comparing Fig. A.4(a) with Fig. A.3(a) observe that the active power behavior is maintained

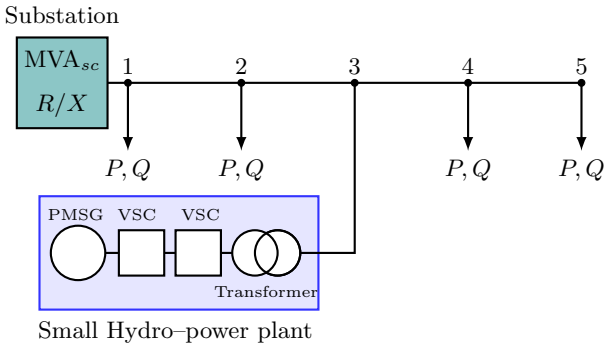

Figure A.2: Simulated primary feeder with a small Hydro–power plant.

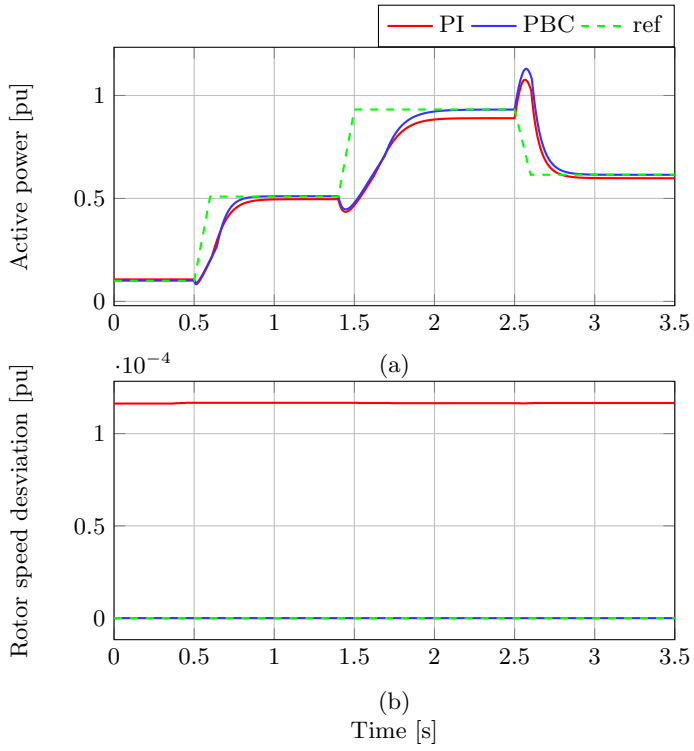

Figure A.3: Dynamic response of PMSG for Scenario 1: (a) Active power generated by PMSG on dc–link and (b) rotor speed deviation.

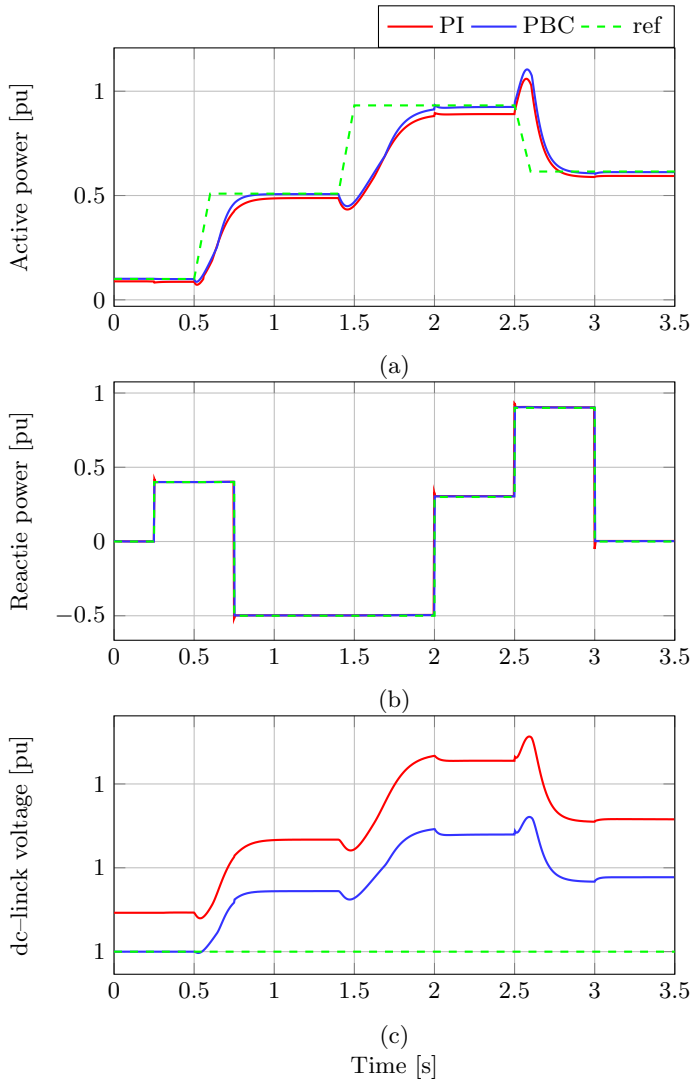

Figure A.4: Dynamic response of the SHP on PCC for Scenario 1: (a) Active power delivered, (b) Reactive power generated, and (c) voltage on capacitor.

where the PBC presents an average error about 6.4 %, while PI controller has an average error about 9.2 %.

Observe in Fig. A.4(b) that both controllers follow the desired reference. However, the proposed controller shows a better dynamical response than the PI controller with a standard deviation of 0.6 %, while the PI controller has a standard deviation of 0.9 %. For the voltage regulation, both controllers present behavior similar.

Scenario 2: Transient behavior. This scenario analyzes the transient behavior of the SHP. We

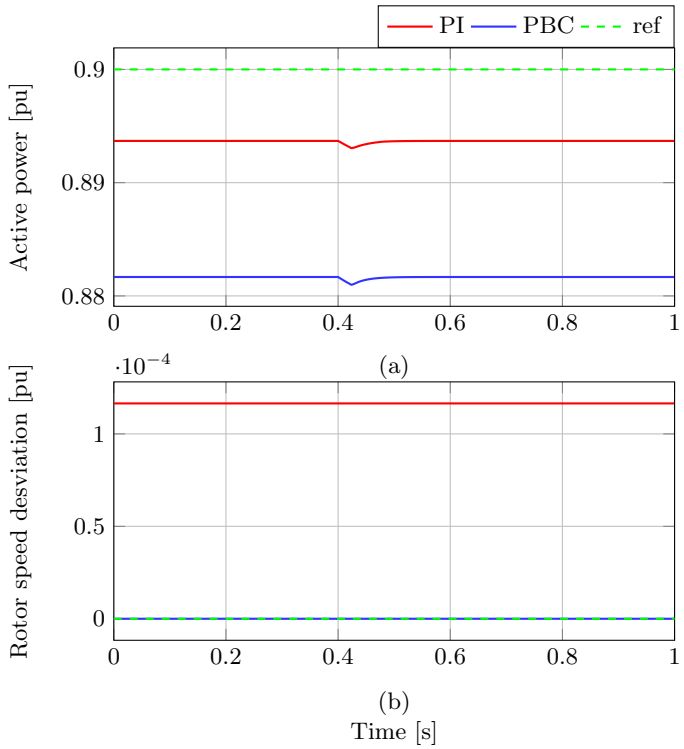

Figure A.5: Dynamic response of PMSG for Scenario 2: (a) Active power generated by PMSG on dc–link and (b) rotor speed deviation.

assumed that the active power generates by the SHP is maintained constant at 0.9 pu. A three–phase short–circuit to ground at Node–3 is considered in $t = 0.4$ s. Results are presented in Figs. A.5 and A.6. The active power generates for both controllers on the dc-link voltage decrease due to the drop in the grid voltage at Node–3. However, both controllers returner initial values (see Fig. A.5(a)). The rotor speed keeps its speed during the fault (see Fig. A.5(b)).

The active power delivered on PCC decreases to almost zero for both controllers. Next, the fault finishes the active power provided by the PBC has a higher peak than the PI controller; But, the proposed controller stabilizes the system in less time compared with the PI controller (see Fig. A.6(a)). Note in Fig. A.6(b) and A.6(c) that both controllers show the same dynamic response for the reactive power and dc-link voltage, respectively.

To quantify the performance of the proposed controller ITAE index is used. The settling time for the active power delivered by PMSG t_p is also considered. The ITAE index are computed for the rotor speed deviation, the dc-link voltage, active power delivered by PMSG, and reactive power,

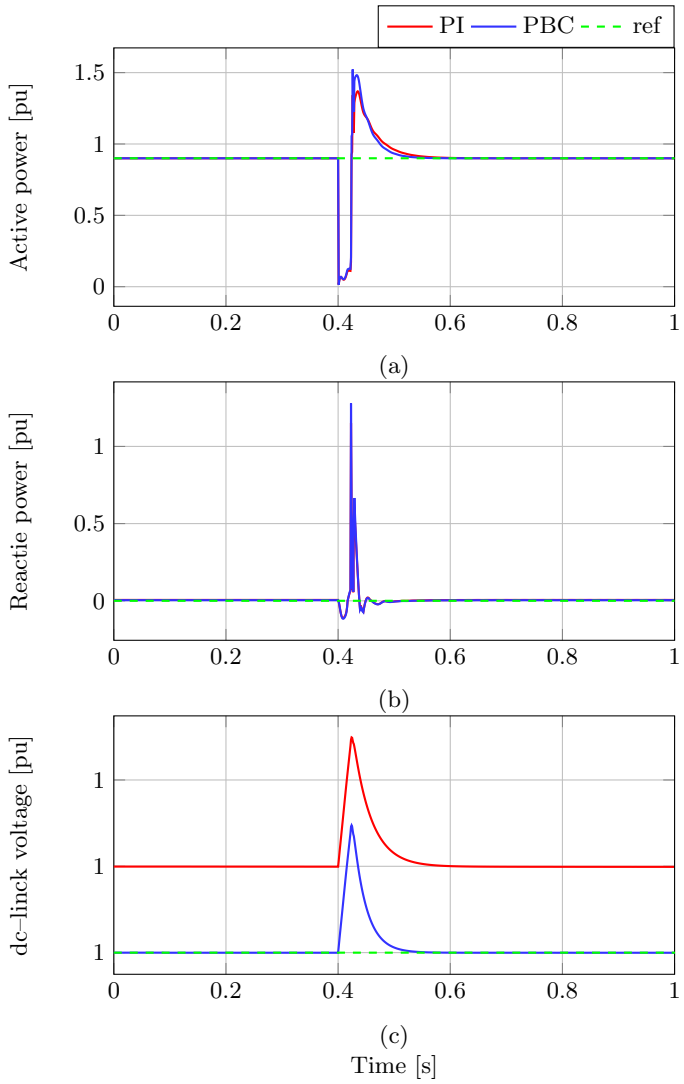

Figure A.6: Dynamic response of the SHP on PCC for Scenario 2: (a) Active power delivered, (b) Reactive power generated, and (c) voltage on capacitor.

as follows

$$ITAEW = \int_0^{t_{sim}} t' \left|\omega - 1\right| dt',$$

$$ITAE_{v_{dc}} = \int_0^{t_{sim}} t' \left|v_{dc} - v_{dc}^*\right| dt',$$

$$ITAE_P = \int_0^{t_{sim}} t' \left|P_e - P_e^*\right| dt',$$

$$ITAE_Q = \int_0^{t_{sim}} t' \left|Q - Q^*\right| dt'$$

Table A.1: Performance Indexes

	Controller	$ITAEW$	$ITAE_{v_{dc}}$	$ITAE_P$	$ITAE_Q$	t_p [s]
Scenario 1	PI	0.2038	0.6096	123.76	26.82	1.3
	PBC	5^{-7}	0.3512	105.36	10.14	1.25
Scenario 2	PI	0.0582	0.2644	16.37	4.754	0.14
	PBC	4.5^{-8}	0.0124	13.04	5.44	0.11

where t_{sim} is the simulation time.

Table A.1 shows the performance indices for each case considered. Note that theses indices validate the better performance for the proposed controller from less steady–state error and faster stabilization in each case proposed.

A.6 Summary of the Appendix

A new approach for the control of a small hydro–power plant based on passivity theory was described in this appendix, which consisted of a PMSG connected to a three–phase grid through a *back–to–back* converter. The proposed controller is based on PBC which guarantees asymptotic stability by means of Lyapunov's theory. The controller was assessed and compared with the classical PI controller considering state and transients behaviors in SHP. It was observed that the controllers based on PBC showed better performance in all scenarios considered than PI controllers, which have been confirmed by comparing with the integral of time–weighted absolute error and settling time.

Appendix B

Parameters for Simulation Studies

This Appendix presents the parameters used in the simulations as well as the control parameters

B.1 12–Bus Test System Parameters

Here presents all data for the 12–bus system and its topology as shown in Fig. 5.1. Transmission line lengths and impedances are given in Table B.1. Transformer data is provided in Table B.2. Generator data is shown in Table B.3. In Figs. B.1 and B.2 IEEE–ST1A excitation systems and IEEE–PSS1A schemes are illustrated, respectively. The parameters of them are given in Tables B.4 and B.5, respectively. Table B.6 describes the base case for the demand load of the test system. Voltage and power bases are 230 kV and 100 MW, respectively.

The control design parameters for the PID governing system and their limits are shown in Table B.7. Here, the parameters were computed as recommended by (IEEE working group report, 1992), while static and transient droop were implemented as recommended by (Machowski et al., 2008). Table B.8 presents the IDA–PBC parameters for HTGS.

Tables B.9 and B.10 show the parameter for the PV plant and the SMES system, respectively. Table B.11 shows the PI–PBC parameters for the PV plant and the SMES system. Additionally,

Table B.1: Transmission Line Data for 12–Bus System.

Line	Length [km]	R [pu]	L [pu]	B [pu]
1–2	100	0.01131	0.08998	0.18377
1–6	300	0.03394	0.26995	0.55130
2–5	400	0.0453	0.3599	0.7351
3–4	100	0.0057	0.0450	0.3675
4–5	150	0.0170	0.1350	0.2757
4–6	300	0.03394	0.26995	0.55130
7–8	600	0.0159	0.1721	3.2853

Table B.2: Transformer Data for 12–Bus System.

From–tp Bus	Type	MVA Capacity	Impedance [%]	Vector Group
1–7	Autotransformer	500	5	$Y_N y_N$
1–9	Step–up	800	4	$Y_N d_{11}$
2–10	Step–up	700	4	$Y_N d_{11}$
3–8	Autotransformer	500	5	$Y_N y_N$
3–11	Step–up	400	5	$Y_N d_{11}$
6–12	Step–up	500	5	$Y_N d_{11}$

Table B.3: Generator Data for 12–Bus System.

Description	Parameter	G # 1	G # 2	G # 3	G # 4
Power nominal	S_{nom} (MVA)	750	640	384	474
Type operation	–	Slack	PV	PV	PV
Voltage nominal	V_t (kV)	15.5	15	18	13.8
Base angular frequency (r/s)	ω_B	$2\pi 60$	$2\pi 60$	$2\pi 60$	$2\pi 60$
Inertia constant (s)	M	4.768	2.932	4.3368	3.1772
d–axis synchronous reactance	x_d	1.220	1.537	1.651	0.920
d–axis transient reactance	x'_d	0.174	0.299	0.232	0.300
d–axis subtransient reactance	x''_d	0.134	0.216	0.171	0.220
q–axis synchronous reactance	x_q	1.160	1.520	1.590	0.510
q–axis transient reactance	x'_q	0.250	0.976	0.380	0.510
q–axis subtransient reactance	x''_q	0.134	0.216	0.171	0.290
Leakage reactance	x_l	0.078	0.133	0.101	0.130
d–axis open–circuit time constant (s)	T'_{do}	8.970	4.300	5.900	5.200
d–axis open–circuit subtransient time constant (s)	T''_{do}	0.033	0.048	0.033	0.029
q–axis open–circuit time constant (s)	T'_{qo}	0.500	1.500	0.535	0.034
q–axis open–circuit subtransient time constant (s)	T''_{qo}	0.070	0.218	0.078	0.034
Synchronous resistance	r_s	0.004	0.003	0.003	0.002
Generator terminal voltage	v_t*	1.0	1.01	1.01	1.01

All parameters are in per unit, except the indicated within parentheses.

Table B.12 shows the values parameters of proposed POD methodology. Here, T_r and T_W have the same values for POD, P–POD and Q–POD, which are 0.016 and 30, respectively. These parameters are selected to produce a band–filter with a cut-on frequency of 0.00534 Hz and a cut-off frequency of 9.895 Hz. These limits cover the bandwidth for the typical power system oscillation modes (Machowski et al., 2008). The cut–off and cut–on frequency are defined when the frequency of a signal is greater than -3 dB (Liu et al., 2015). In Fig. B.3 is illustrated the bode diagram of the low- and washout filters.

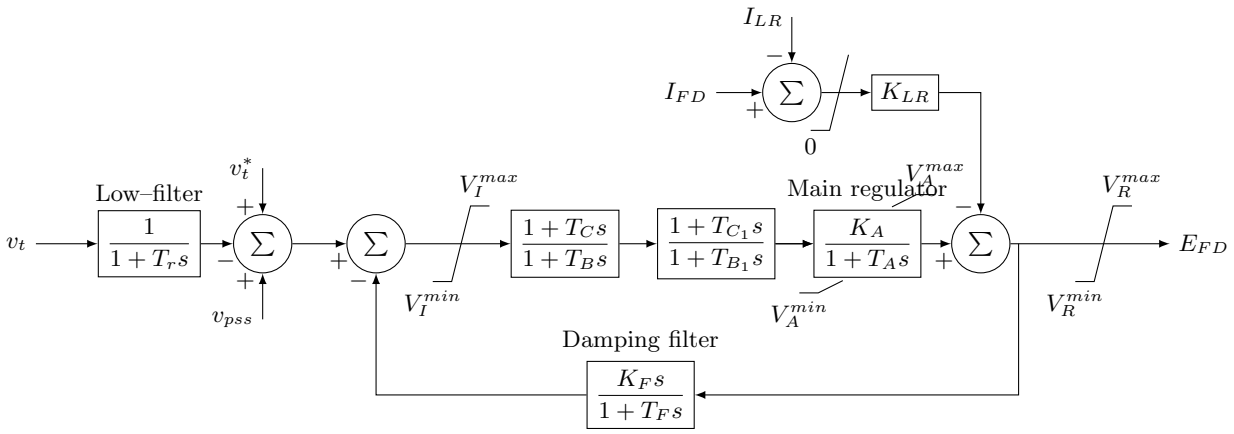

Figure B.1: IEEE–ST1A excitation system

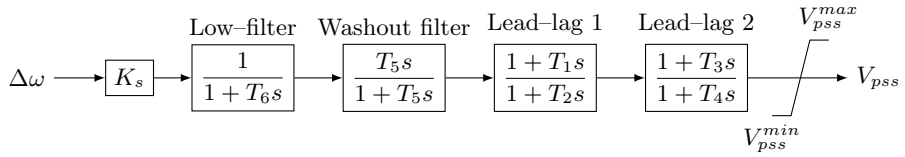

Figure B.2: IEEE–PSS1A single–input power system stabilizer

Table B.4: IEEE–ST1A Excitation System Data.

Description	Parameter	Value
Low–filter time constant (s)	T_r	0.02
Regulator denominator (lag) time constant (s)	T_B	1
Regulator numerator (lead) time constant (s)	T_C	1
Regulator denominator (lag) time constant (s)	T_{B_1}	0
Regulator numerator (lead) time constant (s)	T_{C_1}	0
Maximum exciter output	V_R^{max}	6.43
Minimum exciter output	V_R^{min}	-6
Maximum regulator output	V_A^{max}	6.43
Minimum regulator output	V_A^{min}	-6
Maximum voltage error (regulator input)	V_I^{max}	99
Minimum voltage error (regulator input)	V_I^{min}	-99
Rate feedback gain	K_F	0
Rate feedback time constant (s)	T_F	1
Exciter output current limiter gain	K_{LR}	4.54

All parameters are in per unit, except the indicated within parentheses.

Table B.5: IEEE–PSS1A Power System Stabilizer Data.

Description	Parameter	Value
PSS gain	K_s	16.7
PSS Regulator numerator (lead) time constant (s)	T_1	0.15
PSS Regulator denominator (lag) time constant (s)	T_2	0.03
PSS Regulator numerator (lead) time constant (s)	T_3	0.15
PSS Regulator denominator (lag) time constant (s)	T_4	0.03
PSS washout time constant (s)	T_6	1.65
PSS transducer time constant (s)	T_6	0.015
Minimum PSS output	V_{pss}^{min}	-0.2
Maximum PSS output	V_{pss}^{max}	0.2

All parameters are in per unit, except the indicated within parentheses.

Table B.6: Bus Data for 12–Bus System Base Case Scenario.

Bus	Voltage [kV]	Bus Type	P_{load} [pu]	Q_{load} [pu]	Q_{shunt} [pu]
1	230	PQ	3.00	1.86	–
2	230	PQ	2.50	1.21	–
3	230	PQ	3.00	1.15	–
4	230	PQ	1.00	1.86	2.00
5	230	PQ	1.50	0.48	0.04
6	230	PQ	–	0.49	–
7	345	PQ	–	–	-1.0
8	345	PQ	–	–	–

B.2 13.2 kV Distribution Feeder Parameters

The parameters of 13.2 kV distribution feeder are shown in Table B.13.

B.3 Two–Terminal VSC–HVDC System Parameters

The parameters of the two–terminal VSC–HVDC system have listed in Table B.14, which are presented in (Yang et al., 2018a). We considered that the ac networks are strong; therefore, their inductive effects are ignored, i.e., $x_{ij} = 0 \; \forall \; ij$ (Yang et al., 2018a). Tables B.15 and B.16 show the PI–PBC and PI parameters, respectively.

Table B.7: Governing System Data.

Description	Parameter	Value
Proportional gain	K_p	1.1072
Integral gain	K_i	0.0831
Derivative gain	K_d	2.2144
Permanent Droop	ρ	0.005
Temporary Droop	σ	0.45
Power–Speed	R_s	0.005
Maximum Gate Limit	–	1
Minimum Gate Limit	–	0
Maximum Gate Opening Rate (pu/s)	–	0.1
Minimum Gate Opening Rate (pu/s)	–	–0.1

All parameters are in per unit, except the indicated within parentheses.

Table B.8: The IDA–PBC parameters.

Parameter	r_1	r_2	r_3	r_4	r_5	r_6	r_7	r_8	r_9	r_{10}	k_1
Value	10	5	5	15	80	100	4	4	1	1	40

Table B.9: PV plant Data.

Description	Parameter	Value
Nominal power	S_{nom}	1
Capacitance of dc–link voltage	C	0.1
Transformer inductance	L_t	0.15
Transformer resistance	r_t	0.015
Power Limits	S_{pv}^{max}	1.1

$S_{base} = 50\ MVA$ and $V_{base} = 230\ kV$

Table B.10: SMES system Data.

Description	Parameter	Value
Nominal power	S_{nom}	100 MW
Capacitance of dc–link voltage	C	10 mF
Transformer inductance	L_t	770.31 mH
Transformer resistance	r_t	1.452 mΩ
Coil inductance	L_{sc}	10.8 H
Initial current of superconducting coil	i_s	3800 A
Maximum current of superconducting coil	i_s	4400 A

Table B.11: PI–PBC Gains.

Description	Parameter	Value
PV plant		
Proportional gain for $y_{1_{pv}}$	$K_{P1_{pv}}$	5.0
Proportional gain for $y_{2_{pv}}$	$K_{P2_{pv}}$	5.0
Proportional gain for P^*_{pv}	$K_{I_{P*}}$	2.0
Integral gain for $y_{1_{pv}}$	$K_{I1_{pv}}$	50
Integral gain for $y_{2_{pv}}$	$K_{I2_{pv}}$	50
Integral gain for P^*_{pv}	$K_{I_{P*}}$	20
SMES system		
Proportional gain for $y_{1_{sc}}$	$K_{P1_{sc}}$	10.0
Proportional gain for $y_{2_{sc}}$	$K_{P2_{sc}}$	10.0
Proportional gain for $y_{3_{sc}}$	$K_{P3_{sc}}$	5.0
Proportional gain for i^*_{sc}	$K_{i^*_{sc}}$	2.0
Integral gain for $y_{1_{sc}}$	$K_{I1_{sc}}$	30
Integral gain for $y_{2_{sc}}$	$K_{I2_{sc}}$	30
Integral gain for $y_{3_{sc}}$	$K_{I3_{sc}}$	50
Integral gain for i^*_{sc}	$K_{i^*_{sc}}$	20

$S_{base} = 50\ MVA$ and $V_{base} = 230\ kV$

Table B.12: POD parameters.

Description	Parameter	Value
POD gain	K_f	20
P–POD gain	K_P	100
Q–POD gain	K_Q	20
Transformer resistance	r_t	0.015
Low-filter time constant (s)	T_r	0.016
Washout filter time constant (s)	T_W	30

$S_{base} = 50\ MVA$ and $V_{base} = 230\ kV$

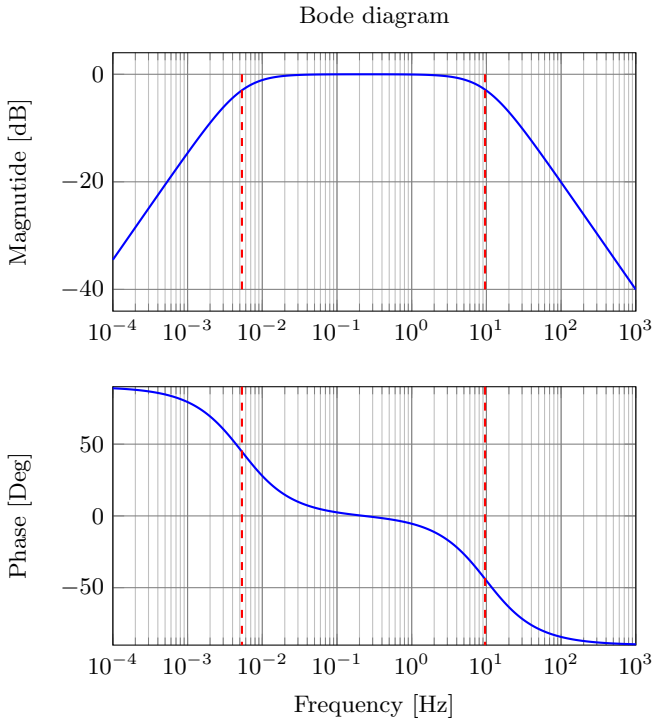

Figure B.3: Bode diagram of POD methodology.

Table B.13: Parameters of the 13.2 kV Distribution Feeder.

Parameter	Value	Unit	Component
Nominal power	2	MVA	PMSG
Nominal voltage	690	V	
Nominal rotational speed	$2\pi 34$	rad/s	
Stator phase resistance	0.05	pu	
Armature impedance	0.80	pu	
Flux	1.50	pu	
Starting time of water in tunnel	4	s	SHP
Factor of constant proportionality	1.65		
Servomotor main time constant	0.3	s	
Friction losses on penstock	$1.7 \cdot 10^{-4}$	pu	
Nominal voltage	13.2	kV	Grid
Three–phase short circuit power	100	MW	
X/R ratio	7		
Frequency	60	Hz	

Table B.14: The VSC–HVDC System Data.

Description	Parameter	Value
Power–base	S_{base}	100 MVA
AC base voltage	V_{base}	100 kV
DC base voltage	v_{dc}	200 kV
AC system inductance (25 km)	L	2.6 $\frac{mH}{km}$
AC system inductance (25 km)	L	2.6 $\frac{mH}{km}$
AC system resistance (25 km)	R	0.022 $\frac{\Omega}{km}$
DC cable inductance (50 km)	L_{dc}	2.2 $\frac{mH}{km}$
DC cable resistance (50 km)	R_{dc}	0.016 $\frac{\Omega}{km}$

Table B.15: Passivity–based PI gains.

$K_p = \text{diag}(4.915, 4.328, 4.253, 2.495) \cdot 10^{-12}$	
$K_i = \text{diag}(6.196, 1.705, 1.780, 6.750) \cdot 10^{-12}$	
$Kp_p = 1.162 \cdot 10^3$	$Ki_p = 1.3458 \cdot 10^4$
$Kp_v = 895.44$	$Ki_v = 1.9645 \cdot 10^4$

Table B.16: PI controller gains.

	ΔP_1	ΔQ_1	Δv_{dc2}	ΔP_2	ΔQ_2
K_p	29887.3	2990.59	1664.52	569.235	11491.08
K_i	158.26	636.04	24.7	1277.21	1595.35